Universidade de Brasília
Instituto de Geociências
Programa de Pós-Graduação em Geociências Aplicadas e Geodinâmica

Tese de Doutorado Nº 71

DESLOCAMENTO VERTICAL CAUSADO PELA INFLUÊNCIA HIDROLÓGICA NA BACIA AMAZÔNICA

LAVOISIANE FERREIRA

BRASÍLIA-DF

2022

Universidade de Brasília
Instituto de Geociências
Programa de Pós-Graduação em Geociências Aplicadas e Geodinâmica

LAVOISIANE FERREIRA

DESLOCAMENTO VERTICAL CAUSADO PELA
INFLUÊNCIA HIDROLÓGICA NA BACIA AMAZÔNICA

Tese de Doutorado submetida ao Programa de Pós-Graduação em Geociências Aplicadas e Geodinâmica, como parte dos requisitos necessários à obtenção do grau de Doutor em Geociências Aplicadas e Geodinâmica.

Orientador: Prof. Dr. Giuliano Sant'Anna Marotta

BRASÍLIA-DF

2022

Ficha catalográfica elaborada automaticamente,
com os dados fornecidos pelo(a) autor(a)

Universidade de Brasília
Instituto de Geociências
Programa de Pós-Graduação em Geociências Aplicadas e Geodinâmica

LAVOISIANE FERREIRA

DESLOCAMENTO VERTICAL CAUSADO PELA INFLUÊNCIA HIDROLÓGICA NA BACIA AMAZÔNICA

BANCA EXAMINADORA

_____

Prof. Dr. Giuliano Sant'Anna Marotta
Universidade de Brasília

_____

Profa. Drª. Roberta Mary Vidotti
Universidade de Brasília

_____

Prof. Dr. Francisco Hilario Bezerra
Universidade Federal do Rio Grande do Norte

_____

Prof. Dr. Carlos Alberto Moreno Chaves
Universidade de São Paulo

BRASÍLIA-DF

2022

"Eis o meu segredo. É muito simples: só se vê bem com o coração.

O essencial é invisível para os olhos."

Antoine de Saint-Exupéry

Dedicatória

À minha mãe, Maria F. de A. e ao meu irmão, Lavousier Ferreira D. de S., por sempre estar ao meu lado, me apoiar em minhas escolhas e me darem força para acreditar que desafios podem ser superados e que não devo temê-los.

Agradecimentos

Agradeço, primeiramente, à minha mãe, Maria Ferreira, e ao meu irmão, Lavousier Ferreira, por me apoiar e me motivar a buscar o meu desenvolvimento com muita dedicação e esforço.

Agradeço ao orientador, Prof. Dr. Giuliano Sant'Anna Marotta, por ter acreditado em mim, me motivando a realizar esta pesquisa e por todo apoio.

Agradeço à Prof. Drª. Elizabeth Madden por todos os ensinamentos e sugestões que me ajudaram e me motivaram a melhorar os resultados alcançados neste projeto.

Agradeço a todos os coautores dos artigos, Prof. Dr. Giuliano Sant'Anna Marotta, Prof. Drª. Elizabeth Hale Madden, Prof. Drª. Adriana Maria Coimbra Horbe, Prof. Dr. Roberto Ventura Santos e Prof. Dr. José Maria Nogueira da Costa, por toda paciência e sugestões que me ajudaram a evoluir. Serei eternamente grata pela contribuição e por terem aceitado fazer parte desta pesquisa.

Agradeço ao Prof. Dr. Denizar Blitzkow por disponibilizar o dado gravimétrico terrestre.

Agradeço ao Prof. Dr. Giuliano Sant'Anna Marotta, Profa. Drª. Roberta Mary Vidotti, Prof. Dr. Francisco Hilario Bezerra e Prof. Dr. Carlos Alberto Moreno por terem aceitado fazer parte da comissão examinadora.

Agradeço ao Observatório Sismológico pela infraestrutura necessária para a realização deste trabalho e a toda equipe técnica, professores e amigos que me acompanharam nessa jornada. Agradeço ao Observatório Sismológico, por meio do contrato com FURNAS, o pagamento do artigo aberto ao público, ajudando na disseminação do conhecimento científico.

Agradeço ao Observatório Nacional (ON) pela bolsa de pesquisa que me proporcionou a oportunidade de conhecer e começar este projeto, tendo sido extremamente importante para me motivar a continuá-lo.

Abstract

Hydrological loading effects are caused, mainly, by water mass movement between continents and oceans, seasonally modifying the positioning of GNSS stations and the gravity field. Therefore, several studies have sought to establish the relationship between gravimetric and positioning signals for the study of hydrological loading at different scales (global, regional, and local). In this work, a study was carried out at the regional level, in the Amazon Basin, and at the local level, in Manaus. Studies of these deformations aim, mainly, to analyze and model the relationship between the variables that influence the hydrological loading (soil moisture, surface water, groundwater) and the signal of vertical movement measured on the earth's surface, over time.

In the Amazon River Basin region, this study was carried out with the aforementioned variables and also with others, such as topography, soil type, and geology, which can influence both the distribution and the mass movement resulting from the hydrological cycle and which, in turn, reflect on the displacement/deformation variations attributed to the action of loading effects. In addition, observations of displacement at GNSS stations are compared to: a) hydrologic deformation model based on the TWS from GRACE data; and b) high-resolution hydrologic deformation model based on Land Surface Discharge Model (LSDM) water mass simulations.

Results of the hydrologic deformation model based on LSDM show how the GNSS stations can be influenced mainly by local water variations with a high magnitude, such as rivers, which, it was not possible to observe in the hydrological deformation model based on the TWS due to the limitation in the resolution data. I show that amplitude variation of vertical displacement depends on the region's geological nature, i.e., whether it is dominated by sedimentary or igneous/metamorphic rocks. It influences the vertical displacement associated with the hydrologic loading, because porous and permeable thick sedimentary rocks accumulate large volumes of water, leading to extensive seasonal hydrologic loading and, consequently, play a significant role in vertical crustal displacement.

In the center of Amazon Basin, I am using microgravimetry, being the first time applied in Manaus, to obtain more information about the local hydrological cycle, in the rainy (December-May) and dry (June-November) seasons, during drought (2016), and flood (2017) years. Gravity changes measured by high precision gravimeters can be used to monitor changes in water-land distribution in the vicinity of the station. Thus, gravity meters have been widely used for studies of hydrological effects on the local scale such as groundwater, soil moisture, rainfall, or snow covering. Studies at the local scale can reveal more about the behavior of the hydrological cycle and provide a better understanding of the connections between different components of the water balance in the Amazon basin.

3D model results of the river's influence on the anomalous gravitational field shows that the Negro river is not influencing the gravity variation measured by the gravimeter, 7 km from the nearest edge of the river. I estimate the groundwater using the gravity data variation and characterized the behavior of the local hydrological cycle, describing the relative contributions of fluvial height, soil moisture, precipitation, evapotranspiration and groundwater and highlighting the connections between these variables. Results show the connection between groundwater variations and surface water, as rivers.

KEYWORDS: Vertical Displacement, Hydrologic Loading, Gravimetry, Groundwater.

Resumo

Os efeitos de carga hidrológica são causados, principalmente, pelo fluxo de massa d'água entre continentes e oceanos, modificando sazonalmente o posicionamento das estações GNSS e o campo gravitacional. Portanto, diversos estudos têm buscado estabelecer a relação entre sinais gravimétricos e de posicionamento para o estudo de carga hidrológica em diferentes escalas (global, regional e local). Neste trabalho, foi realizado um estudo em nível regional, na Bacia Amazônica, e em nível local, em Manaus. Os estudos dessas deformações visam, principalmente, analisar e modelar a relação entre as variáveis que influenciam a carga hidrológica (umidade do solo, águas superficiais, subterrâneas) e o sinal de movimento vertical medido na superfície terrestre, ao longo do tempo.

Na região da Bacia Hidrográfica Amazônica, realizou-se um estudo com a análise das variáveis citadas acima e também com outras, como a topografia, tipo de solo e geologia, as quais podem influenciar tanto na distribuição quanto no movimento de massa decorrente do ciclo hidrológico e que, por sua vez, refletem nas variações de deslocamento/deformação atribuídas à ação dos efeitos de carga. Além disso, as observações de deslocamento em estações GNSS foram comparadas ao modelo de deformação hidrológica baseado: a) no TWS dos dados GRACE; e b) em simulações de alta resolução do Land Surface Discharge Model (LSDM).

Os resultados do modelo de deformação hidrológica baseado no LSDM mostraram como as estações GNSS podem ser influenciadas principalmente por variações locais de grande magnitude, como rios, o que não foi possível observar no modelo de deformação hidrológica baseado no TWS, devido à limitação na resolução dos dados. Além disso, os resultados demonstraram que a variação de amplitude do deslocamento vertical depende da natureza geológica da região, ou seja, se é dominada por rochas sedimentares ou ígneas/metamórficas. Então, há sua influência no resultado de deslocamento vertical associado á carga hidrológica, pois espessas camadas de rochas sedimentares, porosas e permeáveis acumulam grandes volumes de água, levando à relevante carga hidrológica sazonal e, conseqüentemente, desempenham um papel significativo no deslocamento vertical da superfície.

No centro da Bacia Amazônica, foi utilizada a microgravimetria, para obter mais informações sobre o ciclo hidrológico local, nas estações chuvosas (dezembro-maio) e de seca (junho-novembro), durante um ano de seca (2016) e inundação (2017). Mudanças de gravidade medidas por gravímetros de alta precisão podem ser utilizadas para monitorar a variação de água numa região ao redor da estação. Assim, os gravímetros têm sido utilizados para estudos hidrológicos em escala local, para se estudar a variação de água subterrânea, umidade do solo, chuva ou cobertura de neve. Estudos em escala local podem revelar mais sobre o comportamento do ciclo hidrológico e fornecer um melhor entendimento sobre as diferentes fontes dos componentes do balanço hídrico.

Resultados de modelagem 3D da influência gravitacional do rio mostraram que o rio Negro não está influenciando a variação da gravidade medida pelo gravímetro, a 7 km da borda mais próxima do rio. Estimou-se a água subterrânea usando a variação dos dados de gravidade e caracterizou-se o comportamento do ciclo hidrológico local, descrevendo as contribuições relativas á variação fluvial, umidade do solo, precipitação, evapotranspiração e água subterrânea, destacando as conexões entre essas variáveis. Os resultados mostraram a conexão entre as variações das águas subterrâneas e as águas superficiais, como rios.

PALAVRAS CHAVE: Deslocamento Vertical, Carga Hidrológica, Gravimetria, Água Subterrânea.

Lista de Figuras

Sumário

1. Introdução

Ao longo do tempo, efeitos de carga que atuam na litosfera, como maré terrestre (Agnew, 2007), carga oceânica (Van Dam et al., 1994), carga atmosférica (Van Dam et al., 1997) e carga hidrológica (Van Dam et al., 2001; Meurers, 2006; Zou et al., 2015), vêm sendo assunto de grande interesse científico. Dentre as diversas implicações dos efeitos de carga, tem-se a contribuição em processos geodinâmicos. Tal contribuição pode ser caracterizada por deformações e esforços, de origem sazonal, que pode ser modelada a partir de observações geodésicas e geofísicas sobre a litosfera, com base na variação temporal de posição e ou do campo de gravidade, registrados de forma contínua, e caracterizados como um sinal.

Dentre os efeitos de carga, a carga hidrológica possui especial atenção, pois está associada ao ciclo hidrológico e seus processos subjacentes, cujas implicações estão diretamente associadas à condição de manutenção da vida na Terra. Porém, para que seja possível a realização de estudos de natureza hidrológica envolvendo um sinal geodésico/geofísico, torna-se necessário a compreensão do comportamento de cada fenômeno gerador dos efeitos de carga, para que seja possível a identificação e individualização dos mesmos.

Diversos trabalhos têm sido desenvolvidos para entendimento das variações hidrológicas, por meio de observações do campo de gravidade e de posição variáveis no tempo e sua correlação com nível da água, variações de umidade do solo, eventos de precipitação e cobertura de neve. Dentre os trabalhos, pode-se citar Lambert e Beaumont (1977), Bower e Courtier (1998), Van Camp et al. (2006), Kroner et al. (2007) e Kang et al. (2011) que trabalharam com modelos derivados de observações do campo de gravidade. Nestes trabalhos, o campo de gravidade decorrente da carga hidrológica (entendida como um sinal no domínio do tempo), dependendo do período e da escala de estudo, varia de alguns nm/s² a aproximadamente 200 nm/s² (Kang et al., 2011). Para se atingir tal resultado, efeitos derivados ou não de maré, oscilações do núcleo da Terra ou variações co-sísmicas (Imanishi et al., 2004) cuja ordem de grandeza é similar ou mesmo menor que a alcançada pelos trabalhos citados, precisa ser estudada, tratada e retirada do sinal.

Visto que os efeitos de carga contribuem para a variação no campo de gravidade e, consequentemente, na alteração do regime de esforços locais que podem ser observados na estimativa de deformação por métodos geodésicos, diversos estudos também vêm relacionando as deformações (calculadas pela variação temporal na posição de pontos) às

alterações no ciclo hidrológico (Wang, 2000; Van dam et al., 2007; e Wang et al., 2013). Com efeito, os estudos mencionados também estabelecem boa correlação entre os diferentes tipos de observações citados.

Diante do exposto, e considerando a dificuldade na modelagem de fenômenos dependentes de condições climáticas e meteorológicas, no contexto do entendimento do comportamento geodinâmico decorrentes de mudanças no ciclo hidrológico, entende-se que o tema é pendente de compreensão e, por isto, necessita ser estudado. Portanto, esta pesquisa busca contribuir para o entendimento da relação dos esforços e deformações decorrentes de fontes cíclicas, mais especificamente associadas ao efeito de carga hidrológica, como subsídio para melhorar o entendimento sobre mudanças climáticas e sobre fontes causadoras de eventos sísmicos. E para a realização da pesquisa, foi definida a Bacia Amazônica como área de estudos, por apresentar uma das maiores variações de ciclo hidrológico do planeta (Tapley, 2004) e por contribuir de forma significativa no sistema climático global.

1.1   Objetivos

1.1.1   Objetivo Geral

O objetivo geral desta pesquisa consiste em compreender a relação entre a movimentação de massa, decorrente do ciclo hidrológico, seus efeitos na variação do campo de gravidade e de posição estimados por observações geodésicas/geofísicas.

1.1.2   Objetivos Específicos

Os objetivos específicos consistem em:

- Correlacionar os dados de posição, do campo de gravidade terrestre, dos modelos hidrológicos, de nível fluvial, de variação do freático e das características pedológicas e geológicas da região de estudo, com a finalidade de compreender o comportamento da variação do ciclo hidrológico e de seus efeitos na variação do campo de gravidade e de posição;

- Modelar a variação dos campos de movimentação, deformação e esforço associados à movimentação de massa decorrente do ciclo hidrológico.

1.2   Problema

O principal problema desta pesquisa volta-se à busca do entendimento de: como a variação do ciclo hidrológico afeta seu efeito de carga e altera o regime de esforços locais?

1.3   Hipóteses

As hipóteses afirmativas a serem testadas nesta pesquisa são:

- É possível melhorar o entendimento da relação de causa e efeito, entre variação do ciclo hidrológico e dos campos de gravidade e de posição, considerando modelos hidrológicos, nível fluvial, variação do freático e características pedológicas e geológicas da região de estudo;

1.4   Estrutura da Tese

Esta tese intitulada "Deslocamento vertical causado pela influência hidrológica na Bacia Amazônica" subdivide-se em seis capítulos, sendo eles: introdução; revisão bibliográfica; os dois artigos que buscam atender aos objetivos desta tese; conclusão final; e referências bibliográficas.

No primeiro capítulo foi apresentada uma introdução sobre o tema abordando as justificativas, objetivos, problema e hipóteses. No segundo capítulo foram abordadas as revisões bibliográficas de subtemas das diferentes áreas de conhecimento que integram o tema geral, como: o ciclo hidrológico, na qual é apresentada a base teórica do funcionamento do ciclo hidrológico; os efeitos de carga, englobando principalmente a carga atmosférica, oceânica, maré terrestre e hidrológica; a gravimetria, na qual são apresentados seus conceitos teóricos; e o Sistema de Posicionamento Global (GNSS), na qual estão demonstrados seus conceitos.

No terceiro capítulo encontra-se o artigo no qual foi realizado um estudo regional sobre o deslocamento vertical causado pela influência hidrológica na Bacia Amazônica, intitulado "Deslocamento vertical causado pela influência hidrológica na Bacia Amazônica" (*Vertical displacement caused by hydrological influence in the Amazon Basin*). Neste estudo foi analisada a relação entre as variáveis que influenciam a carga hidrológica (umidade do solo, águas superficiais, subterrâneas) e o sinal de movimento vertical medido na superfície terrestre, ao longo do tempo. Além disso, foram consideradas

também outras variáveis, até então não consideradas, como topografia, tipo de solo e geologia, que podem influenciar tanto na distribuição quanto no movimento de massa decorrente do ciclo hidrológico e que, por sua vez, refletem nas variações de deslocamento/deformação atribuídas à ação dos efeitos de carga. Por fim, as observações de deslocamento em estações GNSS foram comparadas ao: a) modelo de deformação hidrológica baseado no TWS dos dados GRACE; e b) modelo de deformação hidrológica de alta resolução baseado em simulações do *Land Surface Discharge Model* (LSDM).

No quarto capítulo foi realizado um estudo, em nível local, intitulado "Influência hidrológica na variação de gravidade em Manaus, Amazonas, Brasil" (*Hydrological influence on the variation of the terrestrial gravity field in Manaus, Amazonas, Brazil*), na qual foi utilizada a microgravimetria, para obter mais informações sobre o ciclo hidrológico local, nos períodos chuvoso (dezembro-maio) e seco (junho-novembro), durante um ano de seca (2016) e inundação (2017). Mudanças de gravidade medidas por gravímetros de alta precisão podem ser utilizadas para monitorar a variação de água numa região ao redor da estação. Além disso, estudos em escala local podem revelar mais sobre o comportamento do ciclo hidrológico e fornecer um melhor entendimento das fontes entre os diferentes componentes do balanço hídrico na bacia amazônica.

No quinto e sexto capítulos são apresentadas as conclusões finais e referências bibliográficas.

2. Revisão Teórica

2.1 Ciclo Hidrológico

A água ocupa cerca de 71% da superfície terrestre, sendo então considerada o composto mais abundante em sua superfície. Porém, de acordo Shiklomanov (1998), do total de fonte de água do planeta, somente 2,5% é água doce, das quais 68,9% estão nas calotas polares e geleiras, 30,8% em águas subterrâneas, restando apenas 0,3% para lagos, rios, atmosfera, biosfera entre outros.

A água é a única substância que existe naturalmente nos três estados (líquido, sólido e gasoso). O estado líquido tem a maior capacidade de calor específico entre todas as substâncias já conhecidas e, portanto, a transformação de água no estado líquido para o gasoso consome grande quantidade da energia solar total absorvida pela superfície terrestre (Brooks et al., 2013), sendo essencial para o equilíbrio térmico do planeta. Além disso, possui uma importante função biológica na transformação e movimentação de muitos sais minerais e nutrientes em solução de solos e água subterrânea para as plantas, além de, a partir das forças físicas de suas moléculas, ao fluir através da superfície do solo, transportar materiais solúveis e não solúveis para dentro de canais e outros corpos d'água (Brooks et al., 2013).

A circulação de água na Terra, chamada de ciclo hidrológico (Figura 2.1), está associada a diferentes caminhos pelos quais a água evapora da superfície terrestre até a atmosfera e retorna a superfície por precipitação ou condensação (Brutsaert, 2005). Após a precipitação ou condensação, parte da água terá evapotranspiração e temporariamente será perdida da bacia hidrográfica para a atmosfera, mas eventualmente retornará a superfície terrestre como precipitação em outros lugares e assim o ciclo continua.

A evapotranspiração é a soma da interceptação, transpiração e evaporação (Brutsaert, 2005). De acordo Brooks et al. (2013), a interceptação consiste na precipitação que é coletada pelas superfícies de plantas e que evapora de volta, enquanto que a transpiração é definida como a água que é extraída do solo pelas raízes das plantas e que a deixa a partir de evaporação. Também, a evaporação ocorre a partir de corpos de água localizados em uma bacia hidrográfica e da superfície do solo.

A precipitação que não retorna a atmosfera via evapotranspiração pode seguir um fluxo a partir da superfície de solo alcançando os canais e corpos d'agua superficiais ou infiltrar/percolar no solo. A infiltração depende da condição da umidade do solo; da capacidade de controle do solo; e da conexão e tamanho dos poros da matriz do solo (Brooks et al., 2013).

De acordo Manoel Filho (2008), a água infiltrada pode ser dividida em três fluxos: a) fluxo não saturado, o qual permanece na zona não saturada, acima do nível freático, onde os vazios do solo estão parcialmente preenchidos por água e ar; b) interfluxo (escoamento sub-superficial), na qual a água infiltrada pode fluir rapidamente e lateralmente ao alcançar uma camada de solo ou rocha dentro de uma permeabilidade limitada, alcançando depois um canal ou corpo d'agua; e c) através da percolação, que ocorre de forma mais lenta, quando a água infiltrada em excesso, que consegue ultrapassar a capacidade de controle do solo, pode fluir para baixo sob a influência da gravidade até alcançar a água subterrânea (Brooks et al., 2013).
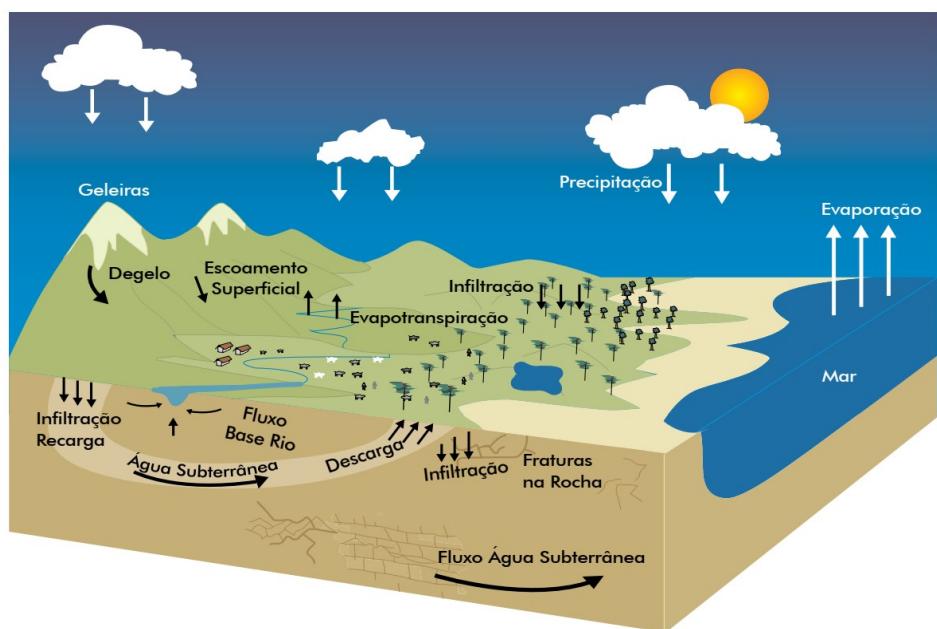
Figura 2.1 – Ciclo Hidrológico (Ministério do Meio Ambiente, 2007).

De acordo Manoel Filho (2008), a distribuição da água no subsolo pode ser dividida em duas zonas horizontais (Figura 2.2), associadas à proporção do espaço poroso preenchido pela água, denominadas zona saturada e não saturada.

Na zona saturada os poros encontram-se completamente preenchidos por água, situando-se abaixo da superfície freática (Freeze e Cherry, 2017), onde se encontra a água subterrânea.

Na zona não saturada, também chamada de zona vadosa ou zona de aeração, os poros estão preenchidos tanto por água quanto por gases (Cleary, 2017; Manoel Filho, 2008). Esta zona, situada entre a superfície do terreno e a superfície freática, pode ser dividida em três camadas, de baixo para cima (Manoel Filho, 2008): a) zona capilar, a qual se estende da superfície freática até o limite de ascenção capilar da água, sendo que próximo à superfície freática os poros encontram-se saturados e nas partes superiores somente os poros menores ficam preenchidos, dando a esta zona um limite superior irregular, chamado de franja capilar, definido como o limite na qual abaixo obtém se um solo praticamente saturado (75%); b) zona intermediária, que se encontra entre o limite de ascenção capilar da água e o limite de alcance das raízes das plantas, na qual sua umidade provém da água capilar isolada não alcançada por raízes e por forças não capilares, como a água pelicular; e c) zona de água no solo (zona de evapotranspiração), que está situada entre o limite radicular e a superfície do terreno, cuja espessura pode ser de centímetros (ausência de cobertura vegetal) a metros (vegetação abundante).
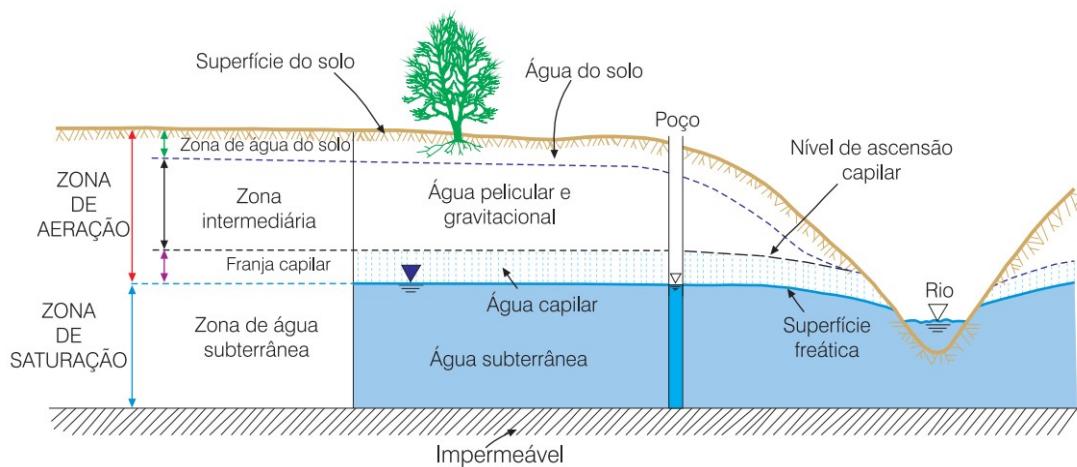
Figura 2.2 – Camadas de distribuição da água no subsolo (Manoel Filho, 2008).

De acordo Brooks et al. (2013), a polaridade da água resulta em suas propriedades de coesão, adesão e capilaridade. De acordo com os mesmos autores, a ligação do hidrogênio ajuda a manter as moléculas de água juntas, por coesão, enquanto a ligação polar a outros materiais (adesão) explica a atração de moléculas de água a partículas de solo e células de plantas.

De uma forma geral, conforme a quantidade de água varia dentro dos poros (Figura 2.3) diferentes forças são atuantes, e além da força gravitacional, o movimento da água também é controlado pelas forças moleculares e tensão superficial.

Quando um solo encontra-se muito seco (Figura 2.3), abaixo do chamado ponto de murcha, significa que a maioria das plantas não pode sobreviver por causa da umidade limitada no solo (Brooks et al., 2013) e porque a força de sucção das raízes das plantas é menor que as forças atuantes sobre essa água (Manoel Filho, 2008). Neste caso, predomina-se a água adsorvida à superfície dos grãos, chamada de água higroscópica, e também, a água que se reúne à superfície dos grãos e à água higroscópica como uma fina camada, denominada de água pelicular (Manoel Filho, 2008).

Conforme a quantidade de umidade aumenta (Figura 2.3), a água passa a ocupar os espaços antes ocupados por gases. Nesta etapa é possível observar a capilaridade, na qual a água pode se movimentar para cima, contra a força gravitacional, a partir de suas propriedades como a coesão entre suas moléculas, que gera uma alta superfície de tensão, juntamamente com a adesão (Brooks et al., 2013). A magnitude da pressão capilar é o quanto um meio poroso parcialmente saturado pode succionar a água repelindo o ar. Então, parte da água infiltrada será retida pelas plantas, a partir da capilaridade (Brooks et al., 2013).

Aumentando mais a umidade no solo (Figura 2.3), chega-se a capacidade de campo, que se refere à quantidade máxima de água que um solo pode reter contra a força gravitacional. Então, uma quantidade de água acima da capacidade de campo pode ser drenada livremente através do solo a menos que essa movimentação seja impedida por alguma camada. Um solo pode ser saturado temporariamente se a taxa de infiltração de chuva ou derretimento de neve dentro do solo exceder a taxa na qual a água se movimenta a partir da percolação.
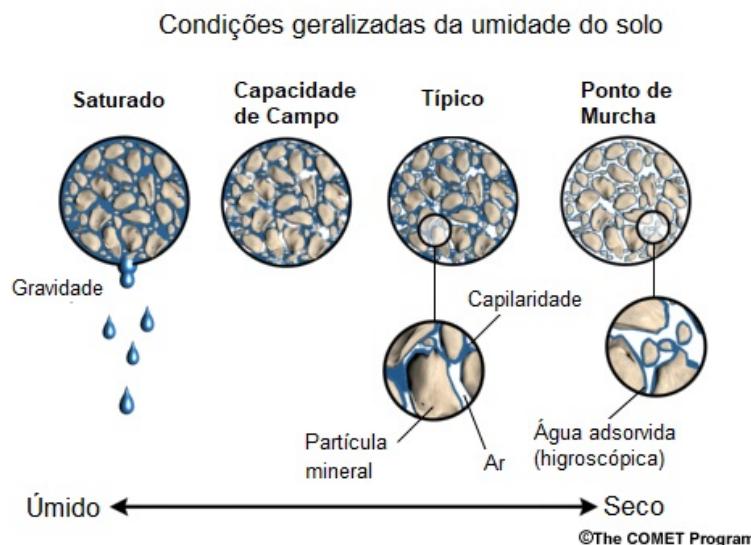
Figura 2.3 – Diferentes condições da umidade do solo (*The COMET Program*, 2019).

De acordo Brooks et al. (2013), a taxa de água que alcança a água subterrânea depende das características subterrâneas dos materias e camadas geológicas que influênciam no caminho preferêncial do fluxo. Algumas águas subterrâneas têm intersecção com canais de rios ou outros corpos de água, retornando a superfície.

2.2 Efeitos de Carga

Efeitos de cargas que atuam na litosfera a partir da atmosfera e, principalmente pela hidrosfera, causam oscilações em sua superfície, de forma sazonal, devido ao fluxo de massa entre continente-oceano (Van Dam et al., 2001; Heki, 2001; Blewitt et al., 2001; Dong et al., 2002; Fritsche et al., 2012). Entre as cargas que devem ser consideradas tem se as decorrentes de mudanças na pressão atmosférica, flutuações dos níveis d'agua dos oceanos, e variações na distribuição de água, neve e gelo.

De acordo Mangiarotti et al. (2001), a redistribuição da massa de ar e água afeta o sistema da Terra de diversas formas como: a) mudança temporal no campo de gravidade; e b) mudança de posição ao centro de massa da Terra no sistema de referência, causando uma variação na rotação da Terra. Ainda de acordo com esses autores, em curto espaço de tempo a resposta elástica da crosta causa a deformação elástica na Terra, principalmente em sua direção radial, sendo possível detectar estes efeitos em escalas desde 1 a 10 anos.

Farrell (1972) menciona que a análise de deformação da Terra a partir de sua superfície e o estudo das forças atuantes e seus efeitos no sistema de massa é um clássico

problema do interesse de geodesistas, nos quais os primeiros cálculos de deformação de maré na Terra foram realizados por Stoneley (1926) e Takeuchi (1950) e os modelos simples de carga de superfície desenvolvidos por Slichter e Caputo (1960) e Caputo (1961, 1962).

Mangiarotti et al. (2001) apontam que a modelagem de deformações elásticas da Terra a partir da superfície de carga é definida a partir da abordagem clássica de Farrell (1972), que calculou a deformação resultante pela carga de massa na superfície a partir de modelos da Terra esférica, baseando-se em estudos da época, como os de Longman (1962, 1963) e Alterman et al. (1959). Nessa abordagem é necessário compreender o comportamento dos diferentes tipos de carga para que se possa separar a contribuição da carga hidrológica.

Existem diferentes causas de variações sazonais de posicionamento e gravidade, definidas de acordo Dong et al. (2002) como:

a) Derivada da teoria gravitacional e da força centrífuga de rotação da Terra, a partir dos efeitos de maré com a contribuição principalmente do Sol e da Lua, que está relacionada ao deslocamento devido a: movimentação polar sazonal, variação do tempo universal corrigido para a movimentação polar (UT1) e deslocamentos de carga devido a marés terrestres, marés oceânicas, marés atmosféricas e maré polar;

b) Derivada de teorias hidrodinâmicas e termais, que tem as cargas derivadas da: pressão atmosférica, flutuações da superfície do mar não relacionadas à maré e carga hidrológica; e

c) Derivada de erros, que são responsáveis por gerar uma aparente variação sazonal, como os erros dos modelos orbitais dos satélites, dos modelos atmosféricos, dos modelos de distribuição de vapor d'agua, da variação dos modelos de centro de fase e multicaminhamento.

2.2.1 Carga Atmosférica

Darwin (1882) demonstrou que a variação de peso gerado pela atmosfera devido à variação de pressão resulta na chamada carga atmosférica. Mangiarotti et al. (2001) cita que, na década de 80, muitos estudos investigaram os efeitos de carga atmosférica na deformação crustal da Terra e na mudança da gravidade local (Stolz e Larden, 1979; Spratt, 1982; Van Dam e Wahr, 1987). Esses estudos resultaram numa carga modelada

com maior acurácia (Velicogna et al., 2001; Van Dam e Wahr, 1987; Van Dam et al., 1994). Além disso, tinham como objetivo compreender o comportamento dos oceanos na resposta barométrica inversa (BI) (Van Dam et al., 1994).

Os oceanos respondem aos efeitos de carga atmosférica como um barômetro invertido, ou seja, cada milibar de pressão que aumenta a superfície oceânica compensa pela depressão de 1 cm, causando um equilíbrio entre a combinação de massa de ar e água total (Van Dam et al., 1994; Wunsch e Stammer, 1997). Nas regiões costeiras ainda existe a contribuição barométrica inversa dos oceanos, considerando que altas e baixas pressões são correlacionadas sobre centenas de quilômetros, mas a 1000 km de distância dos oceanos as estações não são sensíveis a essa contribuição.

Estudos de deslocamento na superfície terrestre devido a mudanças na carga atmosférica concluíram que essa carga pode resultar em perturbações na gravidade de 3 a 6 μGal , sendo maior em altas latitudes onde a variação de pressão é maior (Van dam et al., 1994; Fritsche et al., 2012). O pico de deslocamento radial na superfície da Terra, definida a partir de análises numéricas, é de 10 a 25 mm com associação a um deslocamento horizontal de 1/3 a 1/10 desta magnitude (Van Dam e Wahr, 1987; Rabbel e Schuh, 1986; Van Dam et al., 1994).

2.2.2 Carga Oceânica

Entre as cargas oceânicas tem se a carga de maré e a não derivada da maré.

A carga de maré oceânica está relacionada à variação da coluna d'água dos oceanos devido à força de maré, enquanto que a carga não derivada da maré surge a partir da interação da força de superfície que dirige os ventos, pressão atmosférica, calor, troca de umidade e efeitos hidrodinâmicos (Dong et al., 2002; Van Dam et al., 2007).

A carga oceânica não derivada da maré pode ser causada pela variação da altura do nível do mar e da densidade da coluna d'agua (Dong et al., 2002) e ser responsável por induzir mudanças de pressão no assoalho oceânico, que por sua vez deforma o geoide e as proximidades da crosta, causando uma movimentação de 5 mm pico a pico em regiões próximas a costa, com possíveis deslocamentos verticais acima de 10 mm e deslocamentos horizontais que são em média, 1/3 dos verticais (Van Dam et al., 1997). As deformações associadas à mudança de gravidade são da ordem de 2-3 microgal, porém mudanças de pico a pico de 5 μGal também são preditas (Van Dam et al., 1997).

Modelos de marés oceânicas mostram a variação de altura dos oceanos devido às forças de maré para uma localização e tempo (Urschl, 2005). De acordo Schwiderski (1980), nos últimos três séculos, desde Newton em 1687, muitos cientistas, como Bernoulli, Maclaurin, Euler, Kelvin, Laplace, Darwin e Doodson, tentaram desenvolver modelos de marés globais ou oceânicos por métodos empíricos, teóricos ou hidrodinâmicos. De acordo Thomas et al., (2007), a partir da década de 80, técnicas geodésicas foram capazes de medir deslocamentos na superfície com acurácia de milímetros. De acordo Baker e Bos (2003) os estudos de maré a partir da gravimetria foram os responsáveis pelo melhoramento dos modelos de carga de maré oceânica, os quais antes dependiam de modelos da Terra disponibilizados pela sismologia. Então, estudos de maré a partir da gravimetria foram utilizados para se testar os modelos de carga oceânica (Baker et al., 1996).

A carga de maré oceânica está associada à deformação periódica da crosta (Urschl, 2005), na qual pode resultar num deslocamento de até 10 centímetros na vertical e 3 centímetros na horizontal (Monico, 2008), sendo maior em regiões costeiras. A partir da contribuição de 1 metro de maré a altura do deslocamento devido a carga dentro de um raio de 10 km é de cerca de 1 mm (Penna et al., 2008). No continente é observada a partir da propagação lateral da deformação causada pela carga oceânica, sendo maior nas áreas costeiras que em seu interior (Mangiarotti et al., 2001).

2.2.3 Maré Terrestre

As marés terrestres são perturbações na Terra Sólida causadas pelas influências gravitacionais de corpos celestes e de seus movimentos no espaço (Agnew, 2007), dentre os quais a lua e o Sol são os maiores influenciadores (Dehant et al., 1999). De acordo Wahr (1995) como a força gravitacional exercida pela lua (e sol em menor escala) não é a mesma em todos os pontos da Terra, e por esta força estar associada à variação da distância, entende-se que a aceleração da gravidade também não é a mesma em todos os pontos.

Marés terrestres foram observadas indiretamente há mais de cem anos atrás (Brush, 1996). De acordo Wahr (1995), a deformação causada pelo efeito de maré terrestre é modelada, primeiramente, especificando a aceleração gravitacional luni-solar, variável no tempo e espaço. Para isso, a aceleração é quantificada a partir de um escalar de potencial de maré definido por meio do conhecimento da movimentação orbital da Terra e da lua. E

depois a resposta da Terra precisa ser modelada. Portanto, este é um problema geofísico, no qual, é representado pelos "Números Love".

De acordo Dehant et al. (1999), Love (1926) demonstrou que os efeitos de maré poderiam ser representados por números adimensionais chamados de Números Love, os quais, são calculados para um dado modelo da Terra, e seus parâmetros podem ser utilizados nas funções de Green, tornando o cálculo da resposta de carga reduzida à resolução da integral de convolução (Farrell, 1972).

De acordo Wahr (1995), perturbações no campo potencial gravimétrico são da ordem de 100 µGal ou mais e podem ser determinadas a partir de sensores orbitais. Enquanto que o deslocamento causado na superfície, de algumas dezenas de centímetros em baixas latitudes, pode ser observado a partir de técnicas geodésicas como GPS, VLBI e *Satellite Laser Ranging* (SLR).

De acordo Agnew (2007) com o aumento da precisão das medidas, as correções dos efeitos de maré se tornaram necessários, sendo as marés terrestres relativamente mais fáceis de serem modeladas que as oceânicas, porque a água não é rígida e por causa da geometria do problema.

2.2.4 Carga Hidrológica

O modelo da carga hidrológica ainda não é conhecido em muitas regiões do planeta, mas sua deformação é perceptível nos sinais de posicionamento global e gravimétrico (Van Dam et al., 2001; Blewitt et al., 2001; Wu et al., 2003; Rajner e Liwosz, 2011). Essa carga está relacionada à distribuição de massa d'agua nos continentes, como umidade do solo, água em subsuperfície, neve e gelo (Van Dam et al., 2007). Então, um sinal anual residual de longo comprimento de onda corrigido dos efeitos de carga atmosférica, oceânica e maré deveria representar o efeito de carga hidrológica (Van Dam et al., 2007). Suas deformações são efeitos de larga escala (Blewitt et al., 2001; Rajner e Liwosz, 2011, Davis et al., 2004), regional (Heki, 2001; Rajner e Liwosz, 2017) e local (Wang, 2000; Bevis et al., 2005).

Van Dam et al. (2001) avaliou a relação do deslocamento crustal devido a carga hidrológica numa escala de longos períodos (maior que 100 km) e o sinal de carga encontrado tinha um sinal de variação anual na maior parte das localizações (Figura 2.4) e

nas regiões tropicais, como África e América do Sul, a variação da carga pelo armazenamento de água proporcionou deslocamento de até 30 mm.
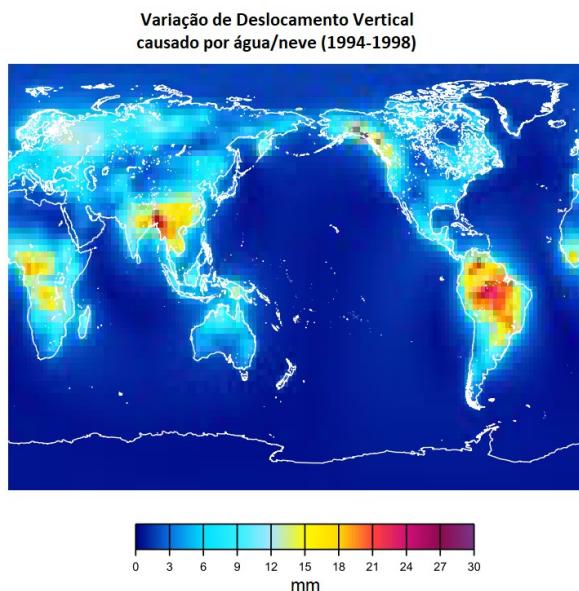
Figura 2.4 – Variação de deslocamento vertical devido à carga hidrológica no período de 1994-1998 (Van Dam et al., 2001).

De acordo Bevis et al. (2005), em Manaus, a variação de deslocamento de um ciclo anual varia de 50 a 75 mm, sendo 2-3 vezes maior que o esperado para esta região, e tem uma correlação inversa com a variação da altura do rio, de 15 metros a 29 metros (Figura 2.5). De acordo com estes autores, a Terra Sólida responde de forma instantânea à variação de carga hidrológica e, portanto, um melhor conhecimento da estrutura elástica crustal, além de trazer informações acerca das relações geodésicas sobre ciclos hidrológicos, traz subsídios para implicação em atividades sísmicas.
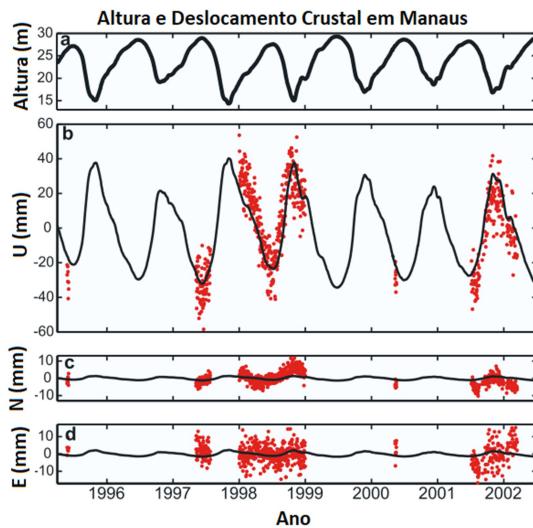
Figura 2.5 – Variação da série de altura do rio em Manaus e modelo de predição do deslocamento (E, N, U) em linha contínua e da estação de GPS MANA, em ponto vermelho (Bevis et al., 2005).

Guimarães et al. (2012) utilizaram séries de estações fluviométricas integrada com dados gravimétricos do *Gravity Recovery and Climate Experiment* (GRACE) e uma estação de posicionamento com o objetivo de analisar o deslocamento crustal na Bacia Amazônica. Obteve um deslocamento vertical do ciclo anual de 80-100 mm com uma alta correlação e uma fase oposta de posicionamento em relação às séries hidrológicas e gravimétricas, mostrando que a crosta responde instantaneamente ao ciclo de carga hidrológica.

Ibanez et al. (2014) utilizaram medidas estruturais de campo nos depósitos sedimentares Miocenos-Holocenos expostos na bacia do Rio Amazonas para investigar o desenvolvimento da Amazônia Central e associaram um pulso extensional com orientação NE-SW à carga hidrológica, que teria induzido uma subsidência flexural, causando esforço extensional na crosta superior.

Miguez-macho e Fan (2012a-b) realizaram a modelagem do comportamento do ciclo hidrológico na Amazônia e associaram a variação da coluna d'agua com a topografia à capacidade de drenagem. Esses autores descreveram essa relação da seguinte forma: a) a coluna de solo com drenagem livre na base pode ser bem descrita para os planaltos (coluna de solo acima da coluna d'agua), na qual resulta num maior controle e alimentação da água subterrânea; b) a água subterrânea é a responsável por acelerar artificialmente a drenagem nas áreas mais baixas, próxima aos vales, a partir do efeito de convergência, na qual o fluxo de água vai das regiões mais altas para as mais baixas; c) a partir da contribuição da água subterrânea que convergiu às planícies e da baixa profundidade da coluna d'agua,

existe um aumento da saturação do solo e redução da capacidade de drenar; e d) a reduzida perda de drenagem nessas planícies durante as estações úmidas levam a um maior armazenamento de água no solo no começo da estação da seca, o que caracteriza sua importância na regulação do ciclo hidrológico.

Pokhrel et al. (2013) descreveram que, na Amazônia, a maior parte da resposta total da água em superfície (*Total Water Surface* - TWS) é devido ao armazenamento em águas subterrâneas (71%), zonas de planícies de inundação (24%) e canais dos rios (5%). Também, em estudo realizado pelos mesmos autores, concluíram que na parte noroeste da região citada, o armazenamento em subsuperfície (zona vadosa e água subterrânea) é saturado e raso durante todo o ano, resultando numa variação do armazenamento de água total (TWS) controlado por planícies de inundação e rios. Por outro lado, a coluna d'agua de armazenamento em subsuperfície é mais profunda na parte sudeste, que possui um solo mais insaturado resultando numa grande capacidade de armazenamento antes de alimentar os canais, sendo o armazenamento de água total (TWS) controlado pela água em subsuperfície.

2.3 Gravimetria

A gravimetria mede a variação do campo de gravidade causada por materiais com diferentes densidades em subsuperfície. Sua base teórica deriva da Lei da Gravitação Universal, descrita por Sir Isaac Newton em *Principia Mathematica* (1687), na qual define que entre duas partículas de massa (m) existe uma força (F) diretamente proporcional ao produto das massas e inversamente proporcional ao quadrado da distância (l).

A expressão vetorial da Lei da Gravitação, a força de atração ($\vec{F}$) entre duas massas m_1 e m_2 separadas pela distância l é dada pela eq. 2.1:

$$\vec{F} = G \ \frac{m_1 m_2}{l^3} \ \bar{l} \tag{2.1}$$

onde, $l = \sqrt{(x - x')^2 + (y - y')^2 + (z - z')^2}$; x, y e z são as coordenadas da partícula atraída e x', y' e z' são as coordenada da partícula atrativa.

Admitindo-se que o corpo de massa m_1 é atrativo e pode ser considerado como composto por volumes elementares dv e o corpo atraído (m_2) é definido como uma massa unitária, a força sobre esses volumes elementares ($\vec{F}_{dv}$) pode ser definida de acordo a eq. 2.2 (Gemael, 1999):

$$\vec{F}_{dv} = -G \iiint_v \frac{\rho}{l^3} \bar{l} \, dv \tag{2.2}$$

Fazendo $dm = \rho \, dv$, sendo ρ a densidade, a decomposição da força segundo o sistema de massa contínua $(\vec{F}_M)$ decomposta nos eixos cartesianos $(x, y$ e $z)$ pode ser escrita pela eq. 2.3 (Gemael, 1999):

$$\vec{F}_x = -G \iiint_M \frac{(x-x')}{l^3} dm; \; \vec{F}_y = -G \iiint_M \frac{(y-y')}{l^3} dm; \; \vec{F}_z = -G \iiint_M \frac{(z-z')}{l^3} dm \tag{2.3}$$

O potencial gravitacional de atração (V), eq. 2.4, formado pela massa $m(x', y', z')$ no ponto $P(x, y, z)$ resulta no potencial $V(P)$ que no caso de distribuição de massa contínua pode ser representado pela eq. 2.5, considerando $dm = \rho \, dv = \rho \, dx' \, dy' \, dz'$ (Guimarães e Blitzkow, 2011):

$$V = \frac{Gm}{l} \tag{2.4}$$

$$V(P) = V(x, y, z) = G \iiint_v \frac{\rho}{l} dv = G \iiint_M \frac{dm}{l} = G \iiint_M \frac{\rho \, dx' \, dy' \, dz'}{l} \tag{2.5}$$

De acordo Gemael (1999), a propriedade fundamental do potencial de atração define que as derivadas do potencial gravitacional segundo os eixos coordenados correspondem às respectivas forças de atração em relação ao mesmo eixo (eq. 2.6):

$$\vec{F}_x = \frac{\partial V}{\partial x} \; ; \; \vec{F}_y = \frac{\partial V}{\partial y} \; ; \; \vec{F}_z = \frac{\partial V}{\partial z} \tag{2.6}$$

O campo potencial gravimétrico é considerado conservativo, ou seja, o trabalho necessário para se mover uma partícula através do campo vetorial $\vec{F}$ independe do caminho na qual percorre (Blakely, 1995). Portanto, a partir dessa propriedade, tem-se que o campo potencial gravimétrico pode ser representado pelo gradiente de uma função escalar V (eq. 2.7).

$$\vec{F} = \nabla V \tag{2.7}$$

O campo potencial de $\vec{F}$ satisfaz as equações de Laplace (eq. 2.8), na qual a soma das derivadas de segunda ordem, membro a membro, significa que o laplaciano do campo potencial gravimétrico não exerce influência fora das massas atrativas (Guimarães e Blitzkow, 2011). .

$$\nabla^2 V = 0 \tag{2.8}$$

Para os pontos interiores ao corpo de massa m, tem-se a equação de Poisson (eq. 2.9; Gemael, 1999):

$$\Delta V = -4\pi G \rho \qquad (2.9)$$

2.3.1 Potencial de Gravidade

A gravidade (eq. 2.10) é resultante da força de atração $\vec{F}$ e da força centrífuga $\vec{C}$:

$$\vec{g} = \vec{F} + \vec{C} \qquad (2.10)$$

A força centrífuga vetorial (eq. 2.11) é dada pela a magnitude da velocidade de rotação da Terra (w) e pelo vetor definido pela separação entre o ponto e o eixo de rotação da Terra ($\vec{d}$):

$$\vec{C} = w^2\vec{d} \qquad (2.11)$$

A força centrífuga $\vec{C}$ resulta do potencial centrífugo (Q), eq. 2.12:

$$Q = \frac{1}{2}w^2d^2 \qquad (2.12)$$

O potencial da gravidade W (eq. 2.13) é dado pela soma do potencial gravitacional com o potencial centrífugo. O gradiente do campo geopotencial resulta na aceleração da gravidade (eq. 2.14), e da equação de Poisson obtém-se a eq. 2.15. Instrumentos geofísicos medem a variação do campo escalar na vertical do campo vetorial de aceleração da gravidade (Blakely, 1995) e seu valor na superfície terrestre é de cerca de 9,8 m/s² (Telford et al., 1990).

$$W = G \iiint_M \frac{dm}{l} + \frac{1}{2} w^2d^2 = G \iiint_M \frac{dm}{l} + \frac{1}{2} w^2 (x^2 + y^2) \qquad (2.13)$$

$$\vec{g} = \nabla W \qquad (2.14)$$

$$\Delta(W) = -4\pi G\rho + 2w^2 \qquad (2.15)$$

2.4 Sistema de Navegação Global por Satélite (GNSS)

O Sistema de Navegação Global por Satélite (GNSS) representa os principais sistemas de satélites utilizados para fins de posicionamento, dos quais atualmente pode-se citar: o Galileo (europeu), GPS (americano), GLONASS (russo) e BeiDou (chinês) (Monico, 2008).

Todos os sistemas de satélites de posicionamento existentes trabalham de forma a emitir dados de navegação e observação. Sendo os dados de navegação responsáveis por possibilitar o cálculo das coordenadas dos satélites em tempo predeterminado, e os dados de observação responsáveis por permitir o cálculo de distâncias entre satélites e receptor.

Uma vez calculadas as coordenadas dos satélites e as distâncias entre satélites e receptor, torna-se possível estimar os valores de coordenadas do ponto onde o receptor se encontra posicionado, pelo processo de trilateração (Figura 2.6). Porém, para que isto seja realizado, torna-se necessário a observação de dados de no mínimo 4 satélites, pois além das coordenadas tridimensionais, a correção do tempo é uma incógnita adicional que também está presente e que precisa ser estimada um sistema de equações lineares. Portanto, todos os sistemas que fazem parte do GNSS desenvolveram suas constelações de satélites de forma a permitir a observação de no mínimo 4 satélites a qualquer tempo e em qualquer lugar da superfície da Terra.
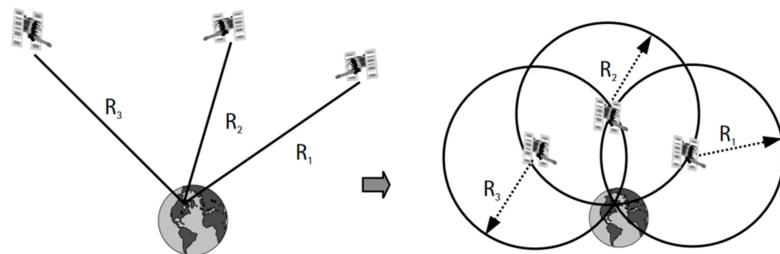
Figura 2.6 – Método de trilateração, na qual requer pelo menos três satélites para se conhecer a localização de um ponto (El-Rabbany, 2002).

Para obtenção de coordenadas precisas, torna-se necessário o conhecimento das fontes de erro associadas aos satélites, à propagação dos sinais, ao receptor e à estação. Estas fontes de erro são apresentadas na Tabela 1, segundo Monico (2008), e tais erros devem ser reduzidos por meio de modelos preestabelecidos e de cuidados no momento do registro dos dados.

Tabela 1 – Fontes e erros envolvidos no GNSS (Monico, 2008)

Fontes	Erros
Satélite	Erro da órbita
	Erro do relógio
	Relatividade
	Atraso entre as duas portadoras no hardware do satélite
	Centro de fase da antena do satélite
	Fase wind-up
Propagação do sinal	Refração troposférica
	Refração ionosférica
	Perdas de ciclos
	Multicaminhamento ou sinais refletidos
	Rotação da Terra
Receptor/Antena	Erro do relógio
	Erro entre os Canais
	Atraso entre as duas portadoras no hardware do receptor
	Centro de fase da antena do receptor
	Fase wind-up
Estação – (alguns erros são, na realidade, efeitos geodinâmicos que devem ser corrigidos.)	Erro nas coordenadas
	Multicaminhamento ou sinais refletidos
	Marés terrestres
	Movimento do pólo
	Carga oceânica
	Pressão da atmosfera

O sistema de posicionamento global (GPS), utilizado neste trabalho, consiste na constelação formada por no mínimo 24 satélites distanciados a aproximadamente 20000 km de altitude distribuídos em 6 planos orbitais (Figura 2.7) quase circulares, o que permite observações simultâneas de pelo menos 4 satélites num mesmo ponto em qualquer parte do dia e local do globo (Beutler et al., 1998). É um sistema de caminho único no qual os satélites emitem ondas de rádio que se propagam pelo espaço até os receptores na superfície terrestre, cujos dados registrados permitem o calculo da distância entre as antenas dos satélites e receptores. Os dados recebidos constam de mensagens de observação, os quais compreendem a sinais e códigos digitais modulados, e mensagens de navegação (El-Rabbany, 2002).
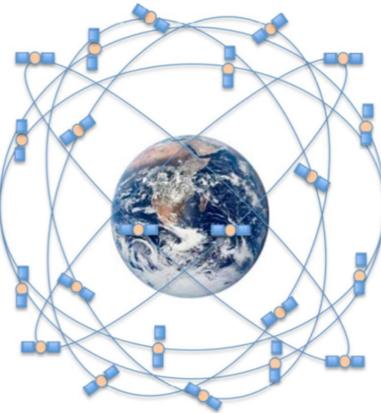
Figura 2.7 – Sistema de posicionamento global (GPS) formada por no mínimo 24 satélites distanciados a aproximadamente 20000 km de altitude distribuídos em 6 planos orbitais quase circulares (*California Institute of Technology*, 2010).

As portadoras de fase dos sinais são centradas em duas frequências de rádio micro-ondas: L1 com 1575,42 Mhz e L2 com 1227,60 Mhz com comprimentos de ondas de 19 cm e 24.4 cm, respectivamente (El-Rabbany, 2002). A distância entre satélite e receptor é feita a partir da soma total entre o número de ciclos inteiro e fracionais multiplicado comprimento de onda da respectiva portadora (El-Rabbany, 2002). Porém o receptor pode definir somente a parte fracional do ciclo de forma mais acurada (2 mm), pois como todos os sinais são iguais, não tem como diferenciar um ciclo de outro para determinar o número de ciclos completos ou ambiguidade (N). Então, estes ciclos desconhecidos são chamados de tendência de ambiguidade ou como ambiguidade inicial do ciclo, que ao serem resolvidas a partir de parâmetros, tornam possível o cálculo acurado de posicionamento (El-Rabbany, 2002).

Dois diferentes códigos são transmitidos por cada satélite: o C/A e o código P. São sequencias geradas a partir de valores binários, conhecidos como *Pseudorandom Noise* (PRN), que não se repetem ate certo intervalo de tempo. O PRN é uma sequência binária que varia de 0 e 1 ou +1 e -1, a qual é gerada por algoritmos ou hardwares chamados *tapped feedback registers* (Langley, 1998). Cada satélite gera códigos únicos para que não haja interferências e também sendo facilmente identificado (Monico, 2008). Então, conhecendo-se o instante de tempo de transmissão do satélite, a partir da comparação entre a sequência do sinal recebido e do sinal replicado, independentemente, pelo receptor GPS é possível a medida do atraso no tempo dos sinais (Langley, 1998).

O código CA é uma sequência de 1023 digitos binários na qual são repetidos a cada milissegundo com um comprimento de cerca de 300 metros (Monico, 2008). O código P

possui cerca de 30 metros, com uma transmissão de frequência f_o de 10,23 Mhz, possui maior precisão pois foi criado para propósitos militares, sendo criptografado (Langley, 1998). O código CA é modulado dentro da L1 utilizado uma técnica chamada quadratura de fase enquanto o código P é transferido na L1 e L2.

Para se calcular corretamente a distância entre os satélites e as antenas receptoras deve-se saber exatamente a localização do satélite. Para isso cada satélite transmite sua própria mensagem com sua informação orbital (efemérides) a serem utilizados no cálculo de posicionamento, deslocamento no tempo do relógio do sistema de tempo do GPS, informações sobre o funcionamento do satélite e sua precisão, além do dado almanaque, que contém informações sobre todos os satélites da constelação, inclusive a descrição das orbitas satelitais com suas localizações (Langley, 1998).

As observáveis de pseudodistância (eq. 2.16) e portadora de fase (eq. 2.17) são definidas como (Langley, 1998):

$$PD = \rho + c\,(dt - dT) + d_{ion} + d_{trop} + e \qquad (2.16)$$

$$\theta = \rho + c\,(dt - dT) + \lambda \cdot N - d_{ion} + d_{trop} + e \qquad (2.17)$$

onde: PD é s observável de pseudodistância; θ é a observável portadora de fase; ρ é a medida geométrica ao satélite; c é a velocidade da luz; dt é a variação de tempo do relógio do satélite no Tempo GPS; dT é a variação de tempo do relógio do receptor no tempo GPS; λ é o comprimento de onda; N é a ambiguidade; d_{ion} é o atraso na ionosfera; d_{trop} é o atraso na troposfera; e representa o multicaminhamento e o ruído no receptor.

3. Deslocamento vertical causado pela influência hidrológica na Bacia Amazônica

Artigo publicado no *Journal of Geophysical Research: Solid Earth*

Lavoisiane Ferreira[1], Giuliano Sant'Anna Marotta[1], Elizabeth Hale Madden[1], Adriana Maria Coimbra Horbe[1], Roberto Ventura Santos[1], José Maria Nogueira da Costa[2]

[1]Instituto de Geociências / Universidade de Brasília

[2]Centro Nacional de Monitoramento e Alertas de Desastres Naturais - CEMADEN

Correspondence to:

L. Ferreira,
lavoisiane@outlook.com

Vertical Displacement Caused by Hydrological Influence in the Amazon Basin

Lavoisiane Ferreira[1] , **Giuliano S. Marotta[1]** , **Elizabeth H. Madden[1]** , **Adriana M. C. Horbe[2]** , **Roberto V. Santos[2]** , **and José M. N. Costa[3]**

[1]Seismological Observatory, Institute of Geosciences, University of Brasília, Brasília, DF, Brazil, [2]Institute of Geosciences, University of Brasília, Brasília, DF, Brazil, [3]National Center for Natural Disaster Monitoring and Alerts – CEMADEN, São José dos Campos, SP, Brazil

Abstract Hydrologic loading studies are related to variables such as soil moisture, precipitation, and groundwater. These parameters are associated with water mass movements, which may affect the positioning of the Global Navigation Satellite System (GNSS) stations and the gravitational field in a seasonal mode. This study addresses the relationship between displacement and deformation variations observed in the Amazon Basin and local geological and climatic features. It also aims to understand mechanisms that may influence the water distribution and mass movement during the hydrological cycle. We have correlated the vertical displacement with soil moisture at different depths in the Amazon Basin. Our approach takes into consideration topography, soil type, water storage, hydrologic deformation model used, sediment thickness, and geology. We show that amplitude variation of soil moisture and water storage parameters depends on the region's geological nature, that is, whether it is dominated by sedimentary or igneous/metamorphic rocks. In areas dominated by sedimentary rocks, soil moisture increases with depth, while in regions dominated by igneous and metamorphic rocks, soil moisture decreases with depth. We conclude that geology and topography influence the vertical displacement associated with the hydrologic loading. We further show an East-West gradient in the Amazon Basin, in which the largest amplitudes of vertical displacement occur in the sedimentary basins to the East. A few stations in the sedimentary basins have less vertical displacement than expected. We argue that these areas may be associated with thinner and more compact sedimentary rock, or even with intrusive igneous rocks.

1. Introduction

Loading effects related to seasonal mass movement between continental and oceanic areas may modify the positioning of the GNSS stations and the gravity field (Blewitt et al., 2001; Dong et al., 2002; Fritsche et al., 2012; Rajner & Liwosz, 2011; Van Dam et al., 2001; Wu et al., 2003). Among the many possible causes of these effects, previous studies have shown the importance of the role of hydrologic loading associated with groundwater variations and the accumulation of snow and ice (Van Dam et al., 2001).

Deformation derived from hydrologic loading can be considered at global (Blewitt et al., 2001; Davis et al., 2004; Van Dam et al., 2001), regional (Heki, 2001; Rajner & Liwosz, 2017), and local scales (Bevis et al., 2005; Wang, 2000). Studies show that deformation depends on variables related to the hydrologic loading (soil moisture, precipitation, groundwater, among others) and the temporal variations of vertical displacement measured at the Earth's surface (Mangiarotti et al., 2001; Wu et al., 2003).

Hydrologic loading is particularly significant in the Amazon Basin due to the considerable seasonal variation of precipitation in the region (Tapley, 2004) and the thicker sedimentary pile that can store large amounts of groundwater. The area is also under the influence of large-scale climate systems, such as the Intertropical Convergence Zone (ITCZ) and South Atlantic Convergence Zone (SACZ), which provoke seasonal and spatial variations in precipitation (Espinoza et al., 2015; Espinoza Villar et al., 2009b; Nesbitt & Anders, 2009; Nobre, 2009; Santos et al., 2015). The Andean orographic barrier associated with the ITCZ movement leads to seasonal variations in precipitation in the north-south and east-west directions (Espinoza Villar et al., 2009a; Santos et al., 2015) and, consequently, to seasonal variations in hydrologic loading.

Several studies have addressed the crustal displacement in the region based mainly on Gravity Recovery and Climate Experiment (GRACE) and Global Navigation Satellite System (GNSS) observations. In general,

these studies consider spatial variations without considering the relationship with geological and climatic features, such as sedimentary distribution and thickness, and the spatial variation in precipitation. In the Amazon Basin, most of the total water storage (TWS) in the Amazon region is in the surface as: groundwater (71%), on floodplains (24%), and in river channels (5%) (Pokhrel et al., 2013). For instance, Van Dam et al. (2001) identify a loading signal with a minimum-maximum amplitude of 500–1,000 mm of water storage in the tropical regions of Africa and South America that results in up to 30 mm of crustal displacement. Davis et al. (2004) suggest a vertical deformation of 13 mm in the region of the Amazon River. Guimarães et al. (2012), when using time series of hydrological stations at specific sites in the Amazon Basin, obtain a vertical displacement over the annual cycle of 80–100 mm and an opposite phase correlation between the data of the GNSS positioning stations, the hydrological stations, and the GRACE data. Almeida et al. (2012), based on the comparison of GRACE data and local measurements of a river flow, study the water mass distribution of the Amazon Basin and comment that the correlation could be related to the geology of the region, as it is higher in the Solimões-Amazonas and Piedmont Andean areas and lower in the Guiana and Guaporé shield areas. Costa et al. (2012) use GRACE observations to study the hydrologic loading in the Amazon region and obtain the highest values of 5–7 cm of vertical displacement per year in sedimentary and flooded areas of the region. In addition, Ibanez et al. (2014) recognize a flexural subsidence with NE-SW orientation in the upper crust associated with the hydrologic loading in Central Amazonia.

In this paper, we study relations between the displacement and deformation variations observed in the Amazon Basin with regional geological, soil, relief, and climatic features. We further detail the mechanism that may influence the distribution and mass movement based on temporal data generated from GNSS stations in the region. We compare the GNSS data with parameters of the physical environment (e.g., sediment thickness, soil moisture, TWS), aiming to establish relationships between the displacement/deformation variations and the hydrologic loading system. We also present a hydrologic deformation model based on the TWS from GRACE data and a high-resolution hydrologic deformation model based on Land Surface Discharge Model (LSDM) water mass simulations. Available geological data indicate that hydrologic loading in the sedimentary basin may explain the elastic response. Porous and permeable thick sedimentary rocks may accumulate large volumes of water, leading to extensive seasonal hydrologic loading and, consequently, a significant role in vertical crustal displacement.

2. Study Area

The Amazon Basin (Figure 1) occupies an area of 6,110,000 km^2 between the Andes and the Equatorial Atlantic. It extends through Brazil (63%), Peru (17%), Bolivia (11%), Colombia (5,8%), Ecuador (2,2%), Venezuela (0,7%), and Guyana (0,2%) (ANA, 2017).

According to Fisch et al. (1998), the determining factors for the Amazonian climate are the availability of solar energy, through the energy balance, and the meteorological interactions resulting from the precipitation regime and the cloudiness. The mean air temperature varies between 24° and 26° according to the Climatological Norms of 1961–1990 (INMET, 1992). In the southern part of the basin, the rainy season extends from November to March and the dry season from May to September (Nobre et al., 2009). In the northern part, however, the rainy season extends from May to October and the dry season from December to February (Nobre et al., 2009). In the northwest portion of the basin's wetter region, there is an increase in precipitation (March to May) associated with the rise of water vapor convergence; this decreases in the southeast direction (Espinoza et al., 2009a).

The Amazon sedimentary basin is located in the northern part of the South American Plate. The Andes and the Brazilian Shield limit the western and southern parts of the basin, respectively, while the Equatorial Atlantic margin and the Guiana Shield limit its eastern and northern regions, respectively (Almeida, 1978). The basin has two main axes along which various subbasins occur (Figure 1; Caputo, 2014; Milani & Thomaz Filho, 2000). The N-S subbasins border the Andes and include the Beni, Madre de Dios, Ucayali, Huallaga, Santiago, and Putumayo Orient Maranon subbasins. The E-W basins include the Acre, Solimões, and Amazonas subbasins, which are separated from each other by tectonic structures called arches (e.g., Iquitos, Purus, Monte Alegre, Gurupá). For instance, the Iquitos Arch separates the Acre basin (area 40,000 km^2, depth 6,000 m (Caputo, 2014)) and the Solimões basin. The Solimões basin has thick sills
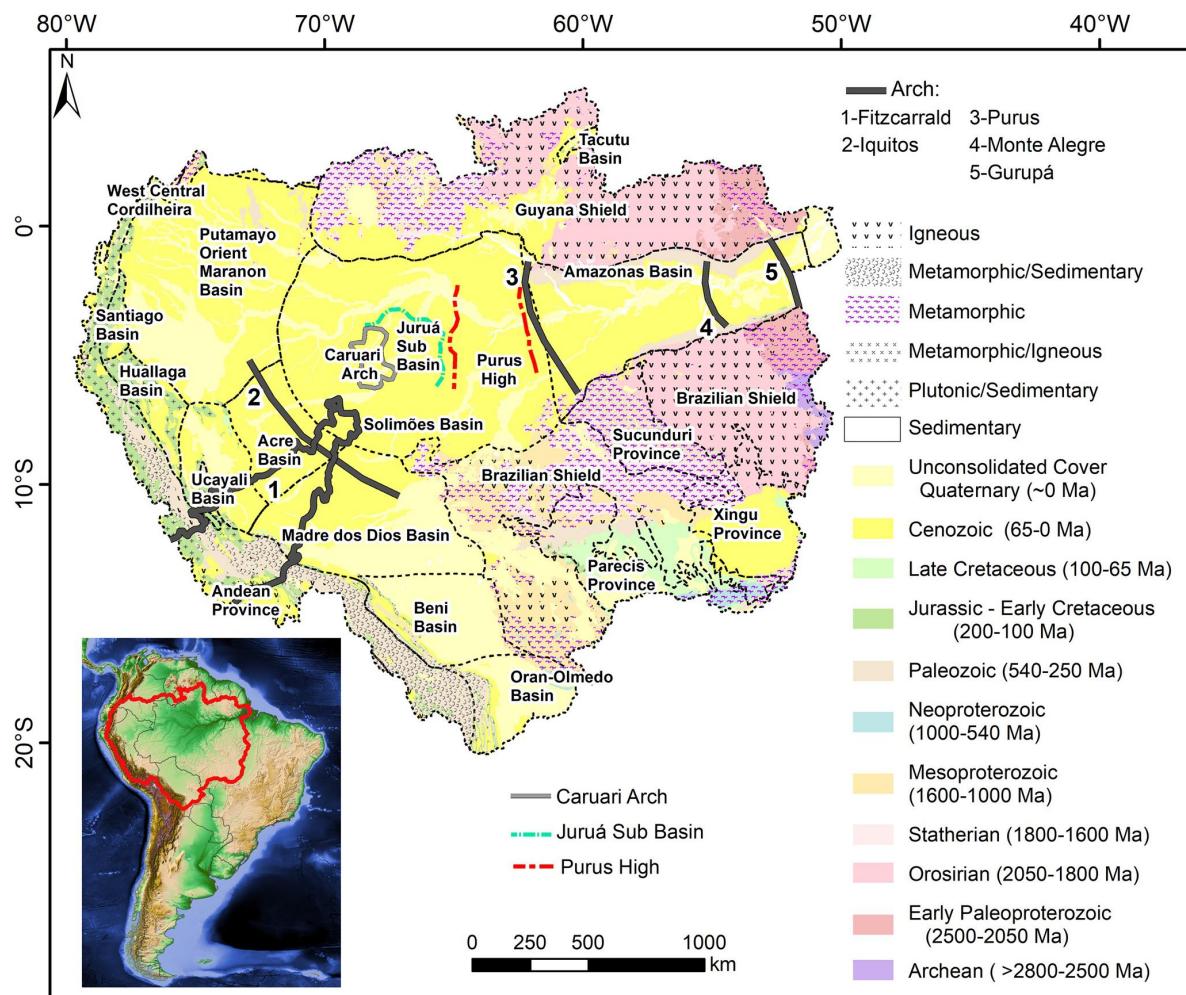
Figure 1. Geology of the Amazon Basin (modified from Schobbenhaus & Bellizia, 2001), tectonic provinces (Schenk et al., 1999), Purus High limits (Munis, 2009) and Fitzcarrald, Iquitos, Purus, Monte Alegre, and Gurupá Arches.

of diabase in the Juruá area that overloads and may cause isostatic depression in the upper crust (Caputo & Soares, 2016). The intrusions may also have led to the formation of the Carauarí Arch to the west (Caputo & Soares, 2016). These arches formed two subbasins in the Pennsylvanian (Milani & Thomaz Filho, 2000): Jandiatuba to the west with up to 3,500 m of sediments, and Juruá to the east with up to 3,800 m of sediments (ANA, 2015).

The Purus Arch limits the Solimões and Amazonas basins (Figure 1). This arch is the result of the pressure that reversed the Cachimbo Graben (Mesoproterozoic) (Caputo & Soares, 2016). In the Carboniferous, sediments covered both sides of Purus Arch, when both the Solimões and Amazonas basins received the same kind of sediments (Caputo & Silva, 1991). The Amazonas Basin covers an area of 500,000 km^2 in which the maximum sedimentary thickness reaches 5,000 m (Milani & Thomaz Filho, 2000). Dikes and thick sills intrude the sedimentary rocks on the eastern side of the basin (ANA, 2015). The Gurupá Arch limits its western border, which is the east side of the Marajó rift. This last subbasin extends for 53,000 km^2 and has maximum sedimentary thickness above 16,000 m (Zalán & Matsuda, 2007). Available studies indicate that this basin is an aulacogen (aborted rift) covered by a sag-type basin (Zalán & Matsuda, 2007).
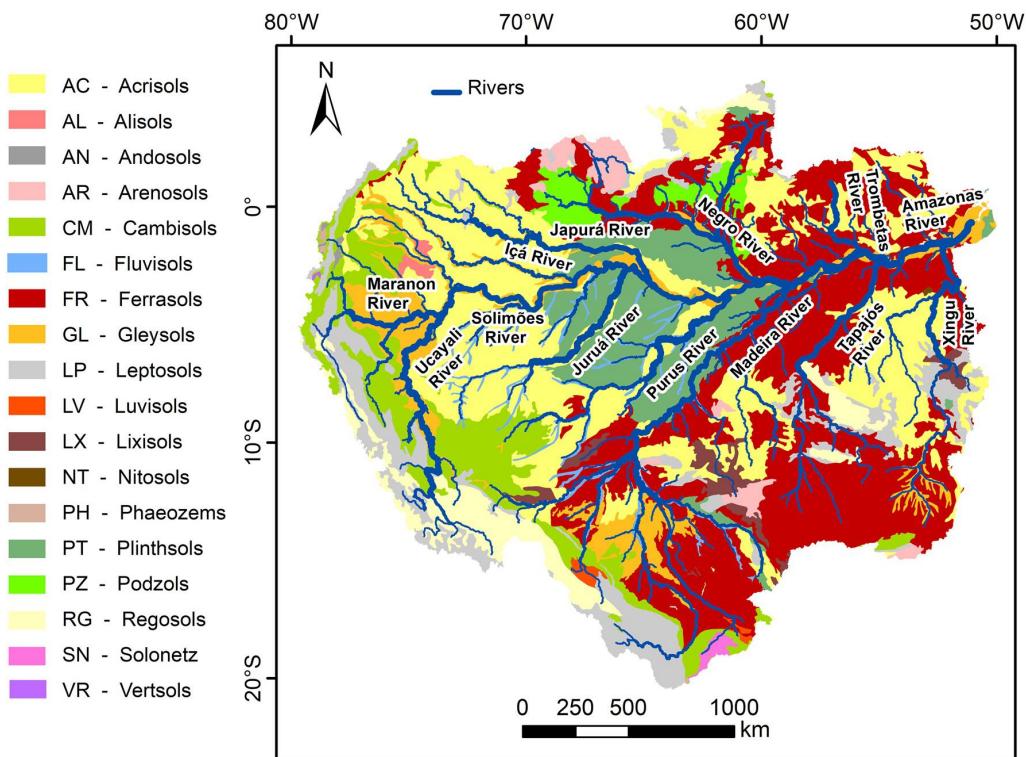
Figure 2. Soil map of the study area provided by the International Soil Reference and Information Centre (ISRIC) and distribution of the rivers provided by Geonetwork/FAO.

The basins of Solimões, Amazonas and Marajó have as substrate pre-Cambrian rocks represented by the Amazonian Craton (Almeida, 1978), subdivided into the Guyana Shield to the north and the Brazilian Shield to the south.

Figure 2 shows a soil map of the region. In the study area, acrisols, ferrasols, plinthosols, podzols, gleysols, cambisols, leptosols, and regosols predominate. The gleysols occur near to the drainage areas, while cambisols and acrisols are more frequent in the Solimões Basin. In the Amazonas Basin, there are acrisols, plinthosols, and ferrasols. In the Andean region, where igneous and metamorphic rocks prevail, the most common soils are leptosols and regosols.

The Amazon River and its tributaries constitute the largest source of fresh water on land (Tourain et al., 2018). The river basin releases approximately 209,000 $m^3 s^{-1}$ (20% of the global discharge) of fresh water to the ocean (Marengo, 2005; Molinier et al., 1997). Figure 2 shows the main tributaries rivers provided by Geonetwork/Food and Agriculture Organization (FAO). The major tributaries have their sources in the Andes (Solimões, Içá, Japura, and Madeira rivers), in the subAndean trough (Juruá and Purus rivers), in the Guyana Shield (Negro and Trombetas rivers) or drain the Brazilian Shield (Tapajós and Xingú) (Seyler & Boaventura, 2003). According to Latrubesse et al. (2005, 2017), 20 of the 34 largest tropical rivers are Amazonian tributaries and four of the 10 largest rives in the world are in the Amazon Basin (the Amazonas, Negro, Madeira, and Japurá rivers).

3. Methodology

To study the relationships between displacement and deformation variations and effects related to the hydrologic loading system between 2015 and 2018, we use several data types. We use daily positioning data from 35 GNSS stations (Figure 3), processed, and made available by the Nevada Geodetic Laboratory (NGL)
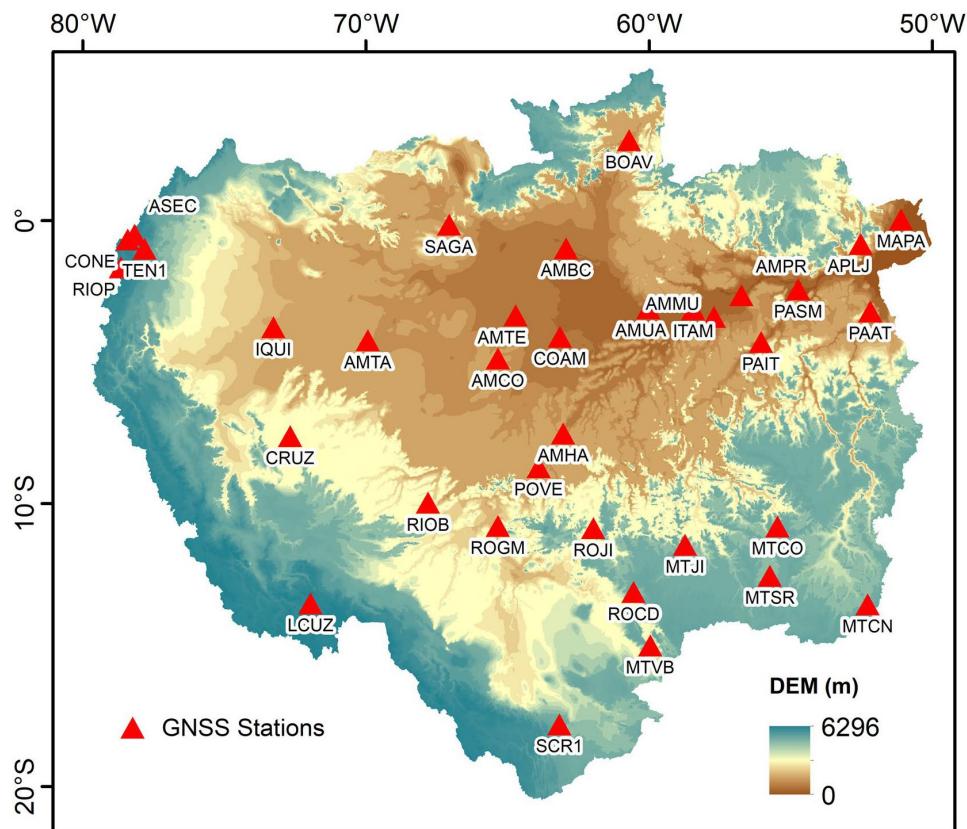
Figure 3. Distribution of GNSS stations and relief variation from DEM/GTOPO30.

and Blewitt et al. (2018). The geology (Munis, 2009; Schenk et al., 1999; Schobbenhaus & Bellizia, 2001) is shown in Figure 1. Soil type provided by ISRIC (Batjes, 2005; Dijkshoorn et al., 2005) is shown in Figure 2. Soil moisture data, with 3 h sampling rate and 0.25° spatial resolution, is from the Global Land Data Assimilation System (GLDAS) NOAH and made available by National Aeronautics and Space Administration (NASA)/Goddard Space Flight Center (GSFC). We also use a Digital Elevation Model (DEM) from the Global 30-Arc-Second Elevation (GTOPO30) data set (Smith & Sandwell, 1997) and take sediment thickness at 1° spatial resolution from the Global Crustal Model—CRUST1.0 (Laske et al., 2013), provided by the Institute of Geophysics and Planetary Physics (IGPP). Alter do Chão Aquifer limit provided by ANA (2016). Total Water Storage (TWS) is estimated using daily GRACE solutions data (Kvas et al., 2019; Mayer-Gürr et al., 2018) up to degree and order 40, provided by the Institute of Geodesy at Graz University of Technology (ITSG). The hydrologic deformation model based on TWS data is computed using the routine by Chanard et al. (2014). The hydrologic deformation model based on the Land Surface Discharge Model (LSDM) (Dill & Dobslaw, 2013) is available from the German Research Centre for Geosciences (GFZ).

We present a high-resolution hydrologic loading model based on LSDM because GRACE, due to its limited spatial resolution, can only sense a long-wavelength average of the load in narrow structures with high loads, like at the main rivers in the Amazon Basin (Fu et al., 2013). The high-resolution model provides more realistic results at stations near large rivers (Dill et al., 2018). Moreira et al. (2016) used this model in the 18 stations in Amazon Basin and find that the hydrologic loading can affect the vertical displacement at up to 10 cm in the center of Amazon Basin.

The time interval (2015–2018) used in this research considers the activity of a large number of GNSS stations in the region, as well as the availability of data from the GRACE mission.

28

3.1. GNSS Positioning Data

The daily positioning data from 35 GNSS stations (Figure 3) were computed according to Blewitt et al. (2018), using the Precise Point Positioning (PPP) technique and the GIPSY/OASIS-II software, version 6.1.1, developed by Jet Propulsion Laboratory (JPL). For a final solution, the coordinates were associated with the IGS08 reference frame. The following parameters were applied to the data processing: orbits, clocks and phase centers of the antennas made available by JPL, mapping function of the troposphere based on the Global Mapping Function (GMF), model of correction of the first-order effect of the ionosphere from the combinations of LC and PC, and correction of the impact of the Solid Earth tide, pole, and ocean tide loading according to International Earth Rotation and Reference Systems Service (IERS) 2010 Convention. Also, the surface displacement was computed in relation to the center of mass, and no corrections were applied to atmospheric pressure and hydrologic loading.

This research uses only the daily vertical positioning (displacement) data (U_{GNSS}).

3.2. GLDAS Data

The GLDAS hydrologic model integrates satellite and surface data using land surface assimilation and modeling techniques. Based on the model, we obtain the flows and states acting on the terrestrial surface (Rodell et al., 2004). The GLDAS data have a spatial resolution of 0.25°, a 3-h sampling rate, and are composed of 36 parameters. We use soil moisture from 0 to 10 cm (SM1), from 10 to 40 cm (SM2), from 40 to 100 cm (SM3), and from 100 to 200 cm (SM4). The soil moisture from 0 to 200 cm (SM) was calculated as the sum of SM1 to SM4.

According to the Land Data Assimilation System (LDAS, 2018), the data has the following information. The soil distribution is taken from the global database of Reynolds et al. (2000), which includes fractions of sand, silt, clay, porosity, among others, as well as from a global database with more than 1,300 soil samples added to the global FAO Soil Map, of the United Nations Educational, Scientific and Cultural Organization (UNESCO). Database information of vegetation cover, developed using sensor data Moderate Resolution Imaging Spectroradiometer (MODIS), with 30 arc-second of spatial resolution, is classified according to International Geosphere-Biosphere Programme (IGBP). Elevation information is extracted from GTOPO30. Weather information (temperature, pressure, humidity, and long-term radiation) are adjusted for the different elevations of the model and additional information is obtained from products derived from various orbital sensors.

In order to analyze the relationship between different types of data in this research, soil moisture data are resampled daily. This process was performed using least squares adjustment with a weighted moving window.

3.3. Total Water Storage (TWS)

To compute TWS, we use the daily gravity field variation of GRACE data calculated by the difference between the coefficients of spherical harmonics (Equation 1). Also, we used a Gaussian filter with a radius of 300 km (Wahr et al., 1998), aiming to obtain the hydrologic response related to the maximum resolution of GRACE:

$$\text{TWS}(\theta,\lambda) = \frac{\rho_e R_e}{3} \sum_{n=0}^{\infty} \frac{(2n+1)}{1+k'_n} \sum_{m=0}^{n} P_{n,m}(cos\theta)\left(\Delta\overline{C}_{nm}\sin m\lambda + \Delta\overline{S}_{nm}\cos m\lambda\right) \tag{1}$$

ρ_e represents the mean density of the Earth (5,540 kg/m³); R_e is the radius of Earth; k'_n is the load love numbers; $P_{n,m}$ is computed by Legendre Functions; $\Delta\overline{C}_{nm}$ and $\Delta\overline{S}_{nm}$ are the spherical harmonics coefficients; θ and λ are latitude and longitude; n and m are degree and order, respectively.

3.4. Hydrologic Deformation Model Based on TWS ($U_{\text{Model}}^{\text{TWS}}$)

After computing TWS, the hydrologic deformation modeling is performed according to the routine provided by Chanard et al. (2014), aiming to calculate the elastic deformation of the Earth by the sur-

face load (Equation 2). These authors use the formalism of classical approach (Farrell, 1972) and the numerical method of Guo et al. (2004). They use Green's Functions computed for a spherical perfectly elastic Earth model based on load Love numbers calculated for Preliminary Reference Earth Model (PREM) (Dziewonski & Anderson, 1981). First, they consider a time-varying, distributed surface load expressed in terms of seasonal equivalent water $h_s(l,t)$ with density (ρ), where t refers to time and l to the site located at the surface. The vertical displacement $U_{\text{Model}(i)}^{\text{TWS}}(L,t)$ at a point L is obtained by convolving the load distribution over a surface S with the Green's functions $G_i(L)$ (Chanard et al., 2014; Farrell, 1972):

$$U_{\text{Model}(i)}^{\text{TWS}}(L,t) = \rho \int_s h_s(l,t) G_i(L-l) dl \qquad (2)$$

Here, G_i refers to the *ith* component of vertical displacement at point L and at the surface point load, a Dirac function, at the origin.

The surface Green's function (Equation 2) (Chanard et al., 2014; Farrell, 1972; Kusche & Schrama, 2005) for vertical displacement induced by a unit mass point is given by:

$$u_\phi = \frac{R_e}{M_e} \sum_{n=0}^{n\infty} h_n' P_n(\cos\phi) \qquad (3)$$

R_e and M_e are the radius and the mass of Earth, respectively; h_n' is the harmonic coefficient for vertical displacement; $P_n(\cos\phi)$ are the Legendre polynomials of nth degree; and ϕ is the angular distance between force application point and observation point (Chanard et al., 2014).

3.5. Hydrologic Deformation Model Based on LSDM Water Mass Simulations ($U_{\text{Model}}^{\text{LSDM}}$)

In general, to calculate a hydrologic deformation model, a large area around every station has to be taken into account, since mass variation induces deformation fields of principally global extent (Dill & Dobslaw, 2013). However, loading extremes along river channels are not resolvable by GRACE due their small-scale variability (Dill et al., 2018; Dill & Dobslaw, 2013; Fu et al., 2013; Karegar et al., 2018).

Dill and Dobslaw (2013) provide the hydrologic loading due the terrestrial water storage given by hydrologic model LSDM (Dill, 2008) on a 0.5° global regular grid with daily temporal resolution. Because locally strong signals with exceptionally high amplitudes occur along the major river channels, they consider that only high-resolution loading calculations of mass water anomalies stored along river can improve the modeled amplitudes in the surrounding area (up to 100 km distance). In order to reconcile the river mass with its location, they first model the river in the high-resolution 0.125° GIS-based river network and then they add this model to the global grid of 0.5° (Dill et al., 2018).

According to Dill and Dobslaw (2013), the loading deformations are numerically integrated in the spatial domain based on Green's function (Farrell, 1972; Kusche & Schrama, 2005). Thus, they generate globally gridded deformations suitable for extracting deformation time series at arbitrary locations by interpolation in space. They attempt to separate the calculation of the globally gridded deformation field into contributions from a 2.0° × 2.0° low-resolution far-field grid and a 0.125° × 0.125° high-resolution near-field grid, thereby exploiting the very smooth behavior of the Green's Function weights for large spherical distances. They map the low-resolution far-field effect to a higher resolution and substitute the high-resolution near-field effect only for a limited distance of up to few degrees.

The LSDM (Dill, 2008) is based on the Hydrological Discharge Model and the Simplified Land Surface Scheme (Hagemann & Dümenil, 1998). The LSDM includes the water in soil moisture, snow, ice, and beyond as runoff and drainage; these are considered in the model river network as overland flow, base flow, and river flow (Dill & Dobslaw, 2013). Thus, the model enables interaction between land surface and river routing in both directions. Deep groundwater variations are not included in the LSDM (Dill & Dobslaw, 2013).

3.6. Vertical Displacement Variations due to the Seasonal Effect in the Amazon Basin

We analyze variations in vertical displacement, U_{GNSS}, in time and space. The temporal analysis includes detection of the delay time (Δt) using cross-correlation between the U_{GNSS} time-series and the parameters SM, TWS, U_{Model}^{TWS} and U_{Model}^{LSDM}. Estimation of the correlation coefficients (R values) between U_{GNSS} and these same parameters is performed after the Δt correction.

The spatial analysis includes comparison between the R values and the maximum amplitudes of SM and TWS (ΔSM and ΔTWS) for each station, aiming to highlight the characteristics of the hydrological cycle associated with the hydrologic loading. We also compare the maximum amplitudes of U_{GNSS}, TWS, U_{Model}^{TWS} and U_{Model}^{LSDM} (ΔU_{GNSS}, ΔTWS, ΔU_{Model}^{TWS} and ΔU_{Model}^{LSDM}), to soil type, sediment thickness and geology, aiming to improve understanding of how U_{GNSS} is associated with the storage and/or transportation of water mass in the study area.

4. Results

Figure 4 shows the cross-correlation between the U_{GNSS} time-series and the parameters SM, TWS, U_{Model}^{TWS} and U_{Model}^{LSDM}. Table 1 shows the estimated R values for each station and reveals that there are significant differences in Δt and R for each station. We identify stations with better R values as those with $R < -0.6$ for SM, TWS and $R > 0.6$ for U_{Model}^{TWS} and U_{Model}^{LSDM} and with worse R values as those with $R > -0.6$ for SM, TWS and $R < 0.6$ for U_{Model}^{TWS} and U_{Model}^{LSDM} in Table 1.

Among the 35 stations studied, 25 (71%) have R values between U_{GNSS} and SM lower than -0.6. Three others showed a positive correlation (LCUZ, TEN1, and RIOP). In terms of the relationship between U_{GNSS} and TWS, 30 (86%) have R values below -0.6 (Table 1). These same stations, have R values for the correlation between U_{GNSS} and U_{Model}^{TWS} above 0.6. 28 stations (80%) have R values for the correlation between U_{GNSS} and U_{Model}^{LSDM} of 0.6 or above.

Figure 5 exhibits the time-series data of the stations with the best R values. A good correlation between U_{GNSS} and the parameters SM and TWS indicates a response of vertical displacement to mass changes related to seasonal water storage. It is possible to observe distinct behavior at those stations with better correlations. There is a Δt between different parameters at the same station and at different stations for the same parameter. This shows that the correlation between these variables at each station is not homogeneous and, therefore, is dependent on the location.

The strong correlation between U_{GNSS} and parameters related to seasonal water storage indicate that the hydrological cycle has a vital role in the fluctuation of the vertical displacement. As shown in Figures 4 and 5, Δt varies with the hydrological cycle, suggesting that appropriate geological conditions to store water in sediments are also essential to explain the fluctuations.

Figure 6 shows the results of the spatial analysis. R values between U_{GNSS} and SM (from 0 to 200 cm) and TWS are shown, as are geological features and relief.

As shown in Figure 6, ΔSM in the shallow parts of the soil displays narrower ranges, since these areas are more controlled by heat effects and exchange of water with the atmosphere. In contrast, in the deeper soil, there is larger contrast among the sites. Sedimentary areas display higher ΔSM values, while crystalline terrains display much lower values. Furthermore, SM increases with depth in regions with sedimentary rocks, but decreases with depth in areas with igneous and metamorphic rocks (e.g., Andes region, Guyana Shield, Brazilian Shield, north and south of the Solimões Basin).

ΔTWS in the Amazon Basin has a strong E-W gradient. It ranges from 118 mm on the western side of the basin to 1,291 mm in the central-eastern side. The higher values (1,291 mm) occur in the Amazonas Basin, and the eastern portion of the Solimões Basin, near to Alter do Chão aquifer. Figure 6 and Table 1 show that the R values of TWS are consistently higher than that of SM, indicating its stronger correlation with U_{GNSS}.

31
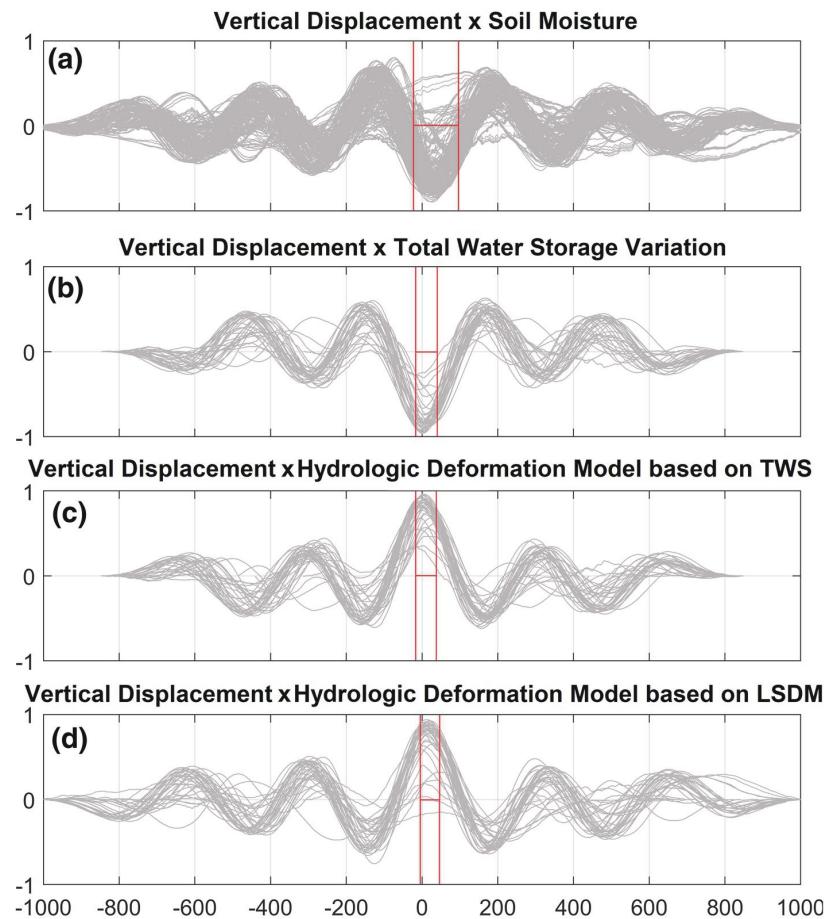
Figure 4. Cross-correlation between the time series of vertical displacement, U_{GNSS}, and SM (a) (soil moisture from: 0 to 10 cm, 10 to 40 cm, 40 to 100 cm, 100 to 200 cm and 0 to 200 cm), TWS (b), U_{Model}^{TWS} (c), and U_{Model}^{LSDM} (d). The red lines show the range of Δt (maximum and minimum values) across all 35 stations.

To evaluate the relationship between U_{GNSS} and storage and/or transportation of water mass, we compare the maximum amplitude values of $U_{GNSS} \left(\Delta U_{GNSS} \right)$ for each station with soil data (Figure 7), geology, maximum amplitude values of U_{Model}^{TWS} and U_{Model}^{LSDM} (ΔU_{Model}^{TWS} and ΔU_{Model}^{LSDM}), sediment thickness, and ΔTWS (Figure 8).

Figure 7 shows spatial relationships between ΔU_{GNSS} and soil characteristics: clay content (Figure 7a), bulk density (Figure 7b), soil class (Figure 7c) and drainage capacity (Figure 7d). There is no spatial correspondence between this different soils information and ΔU_{GNSS}.

Figure 8a shows a stronger relationship between ΔU_{GNSS} and the geology of the station site. ΔU_{Model}^{TWS} (Figure 8b and 8c) is the vertical displacement resulting from the hydrologic deformation model based on TWS calculated using GRACE data. This shows the influence of water at the surface and soil moisture at different depths, down to the deepest aquifers (Dill et al., 2018). The highest values of ΔU_{Model}^{TWS} coincide to the area of the extensive floodplains, and geologically, to the depocenter of the Solimões/Amazonas subbasins. On the other hand, vertical displacement from the high-resolution LSDM model (ΔU_{Model}^{LSDM}; Figure 8d and 8e), shows the influence of soil moisture, shallow groundwater and surface water (rivers, lakes, wetlands; Zhang et al., 2017). This shows the important local contribution of the main river channels, due to their high magnitudes of hydrologic loading.

Table 1

Correlation Coefficients, R, Between Time Series of U_{GNSS} and SM, TWS, U_{Model}^{TWS} and U_{Model}^{LSDM}

Station	SM1	SM2	SM3	SM4	SMT	TWS	U_{Model}^{TWS}	U_{Model}^{LSDM}
AMCO	-0,71	-0,72	-0,74	-0,74	-0,76	-0,89	0,89	0,82
AMHA	-0,84	-0,86	-0,87	-0,84	-0,86	-0,93	0,92	0,88
AMPR	-0,79	-0,80	-0,80	-0,70	-0,77	-0,96	0,96	0,94
AMTA	-0,70	-0,74	-0,77	-0,78	-0,78	-0,82	0,81	0,87
AMTE	-0,75	-0,78	-0,81	-0,82	-0,83	-0,95	0,94	0,90
AMUA	-0,83	-0,87	-0,89	-0,90	-0,91	-0,95	0,95	0,95
APLJ	-0,69	-0,72	-0,70	-0,63	-0,68	-0,85	0,84	0,79
BOAV	-0,70	-0,74	-0,76	-0,73	-0,76	-0,82	0,82	0,82
COAM	-0,69	-0,72	-0,73	-0,75	-0,75	-0,96	0,96	0,91
IQUI	-0,57	-0,59	-0,61	-0,61	-0,62	-0,85	0,83	0,80
ITAM	-0,77	-0,78	-0,81	-0,76	-0,79	-0,97	0,96	0,91
MAPA	-0,66	-0,65	-0,65	-0,57	-0,62	-0,68	0,70	0,68
MTCO	-0,80	-0,82	-0,83	-0,79	-0,83	-0,88	0,89	0,88
MTJI	-0,80	-0,81	-0,82	-0,74	-0,82	-0,88	0,88	0,87
MTSR	-0,80	-0,82	-0,83	-0,73	-0,82	-0,85	0,86	0,79
MTVB	-0,69	-0,71	-0,68	-0,72	-0,69	-0,75	0,76	0,73
PAAT	-0,76	-0,80	-0,84	-0,77	-0,82	-0,87	0,86	0,80
PAIT	-0,67	-0,68	-0,61	-0,43	-0,54	-0,92	0,92	0,88
PASM	-0,59	-0,60	-0,60	-0,64	-0,63	-0,91	0,90	0,86
POVE	-0,79	-0,81	-0,82	-0,81	-0,82	-0,91	0,91	0,88
RIOB	-0,73	-0,76	-0,76	-0,72	-0,74	-0,79	0,82	0,76
ROCD	-0,75	-0,78	-0,78	-0,75	-0,79	-0,85	0,86	0,82
ROGM	-0,73	-0,76	-0,81	-0,78	-0,79	-0,84	0,83	0,80
ROJI	-0,79	-0,81	-0,79	-0,65	-0,79	-0,86	0,87	0,84
AMBC	-0,49	-0,50	-0,49	-0,47	-0,48	-0,84	0,82	0,84
AMMU	-0,49	-0,55	-0,63	-0,47	-0,57	-0,95	0,96	0,92
ASEC	-0,37	-0,39	-0,41	-0,44	-0,43	-0,61	0,65	0,38
CONE	-0,28	-0,30	-0,32	-0,33	-0,33	-0,46	0,55	0,01
CRUZ	-0,29	-0,29	-0,25	-0,10	-0,17	-0,67	0,68	0,58
MTCN	-0,57	-0,52	-0,43	-0,31	-0,43	-0,74	0,77	0,64
SAGA	-0,40	-0,44	-0,51	-0,53	-0,53	-0,75	0,73	0,68
SCR1	-0,36	-0,40	-0,40	-0,29	-0,35	-0,54	0,58	0,39
LCUZ	-0,08	-0,05	0,00	0,17	0,05	-0,30	0,37	0,19
RIOP	0,63	0,67	0,74	0,73	0,73	-0,31	0,35	-0,12
TEN1	0,45	0,49	0,51	0,50	0,50	-0,43	0,47	0,24

Note: *SM*1 represents soil moisture from 0 to 10 cm, *SM*2 soil moisture from 10 to 40 cm, *SM*3 soil moisture from 40 to 100 cm, *SM*4 soil moisture from 100 to 200 cm, and *SMT* soil moisture from 0 to 200 cm. Dark grey shading shows better correlations with R < —0.6 for *SM*, *TWS* and R > 0.6 for U_{Model}^{TWS} and U_{Model}^{LSDM}. Light grey shading shows worse correlations with R > —0.6 for *SM*, *TWS* and R < 0.6 for U_{Model}^{TWS} and U_{Model}^{LSDM}. White shading shows positive correlations for SM, which are not expected.

The ΔU_{Model}^{TWS} varies from 0.009 m to 0.047 m (Figure 8b; Table 2). Figure 8b shows that the highest ΔU_{Model}^{TWS} values are located in the Solimões/Amazonas subbasin, where the thickest sediments in Eastern Amazon occur. The following stations have the highest values: AMUA (0.047 m), COAM (0.046 m), and ITAM

33
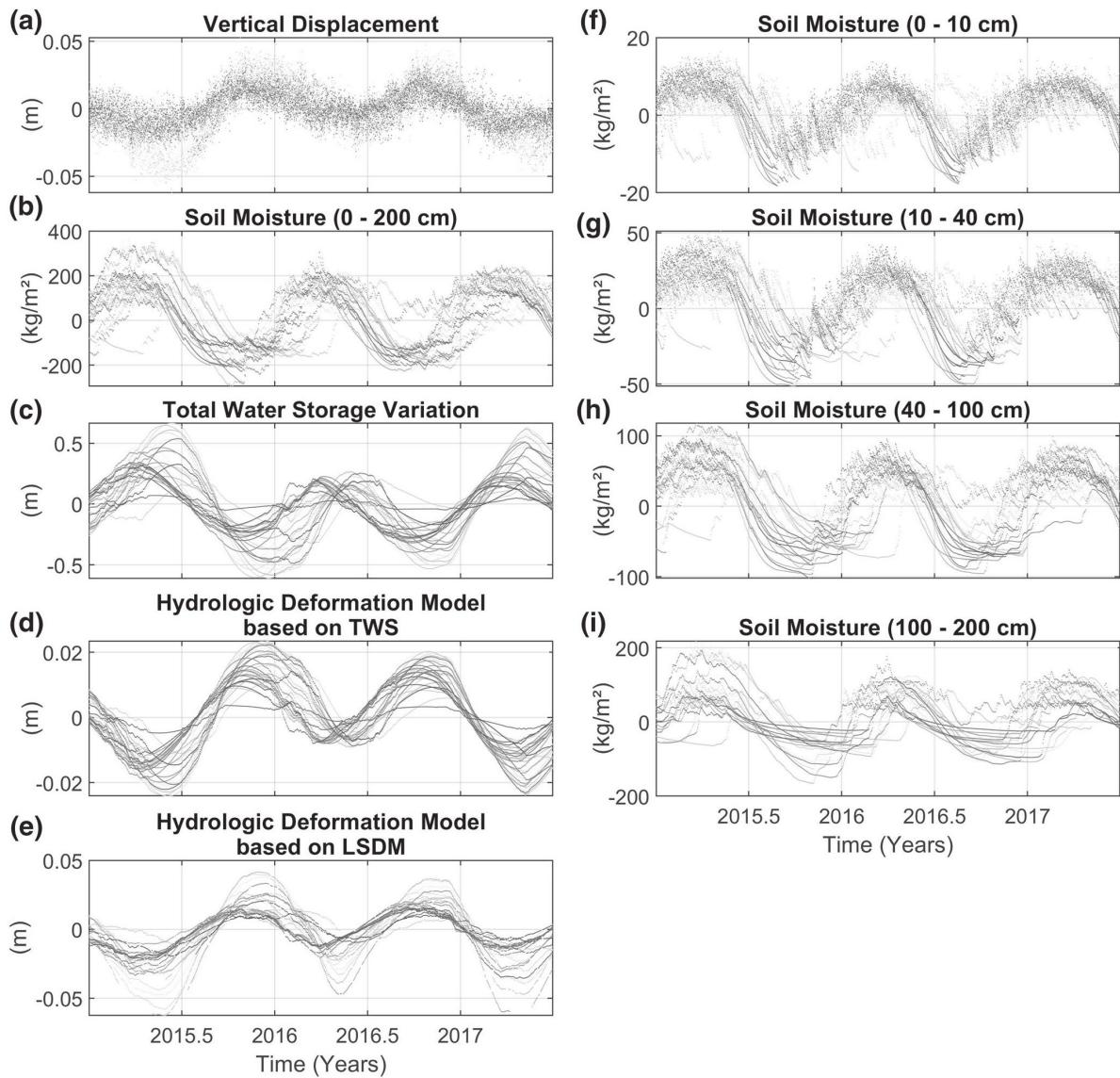
Figure 5. Time series of data from the stations with better R values, lower than -0.6 for SM (b, f, g, h, i) and TWS (c), and higher than 0.6 for U_{Model}^{TWS} (d) and U_{Model}^{LSDM} (e), using U_{GNSS} (a) as reference.

(0.046 m). Here, the Içá and Alter do Chão aquifers have larger seasonal amplitudes of groundwater storage (>450 mm) (Frappart et al., 2019). On the other hand, in the Andes mountainous regions (Figures 3 and 8b), the smallest values of ΔU_{Model}^{TWS} occur.

Considering the ratio between ΔU_{Model}^{TWS} and ΔU_{GNSS}, we observe that the results of ΔU_{Model}^{TWS} account for 18%–66 % of the vertical displacement given by ΔU_{GNSS} (Figure 8c; Table 2). In these results, eight stations (22%) have a contribution between 66% and 51%, 20 stations (57%) have a contribution between 50% and 36%, seven stations (20%) have a contribution between 35% and 18%. In the sedimentary basin, which has higher ΔTWS values (Figure 8c), ΔU_{Model}^{TWS} may account for only 18%–32% of the ΔU_{GNSS}. We analyze this further in the Discussion. The following stations have the highest values: AMCO (66%), AMBC (60%), and ROJI (59%).
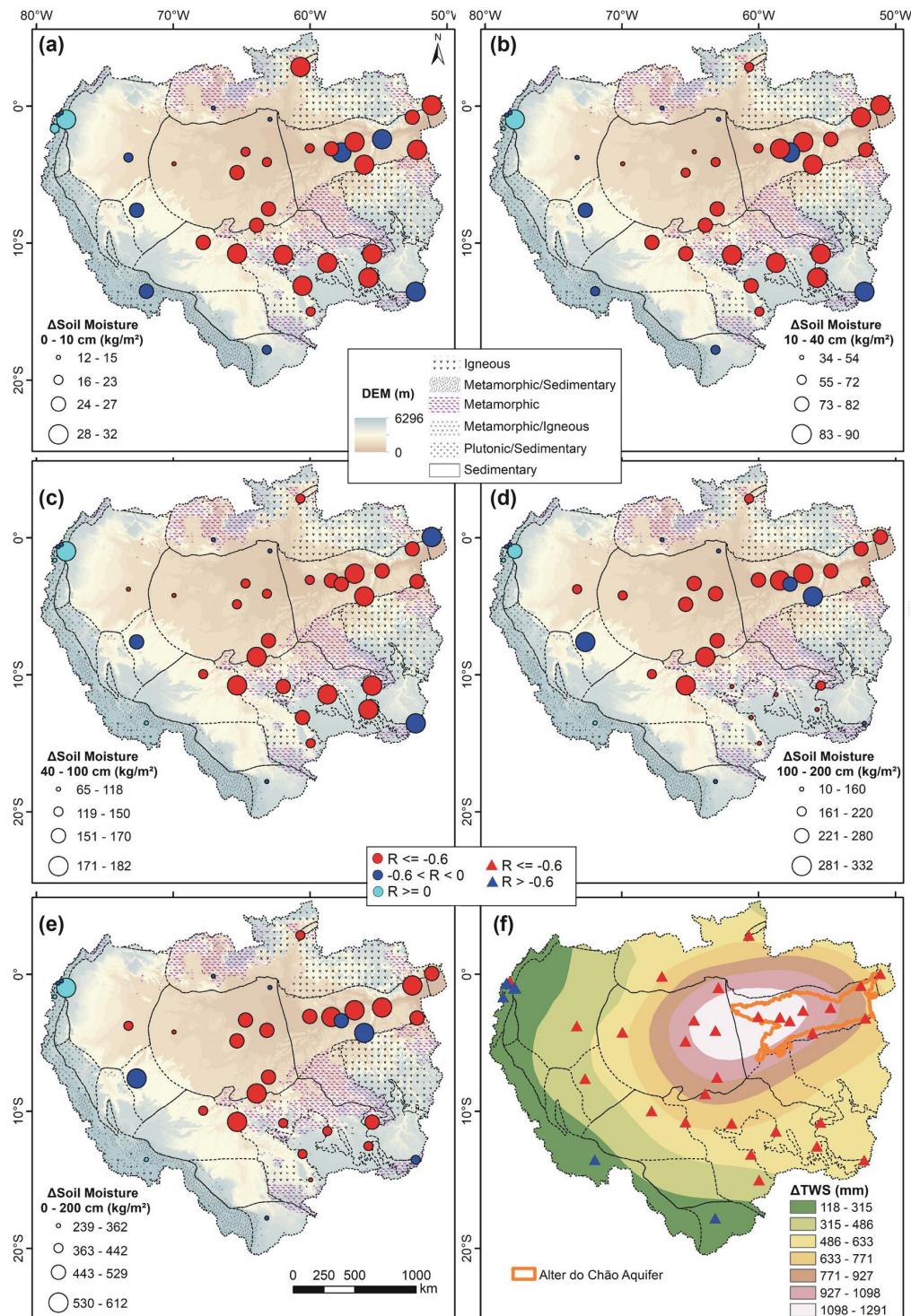
Figure 6. Maximum amplitude variation (Δ) for SM (a, b, c, d, e) and TWS (f). The ranges of *R* values between U_{GNSS} and SM (circles) and TWS (triangles) are marked in different colors.

35
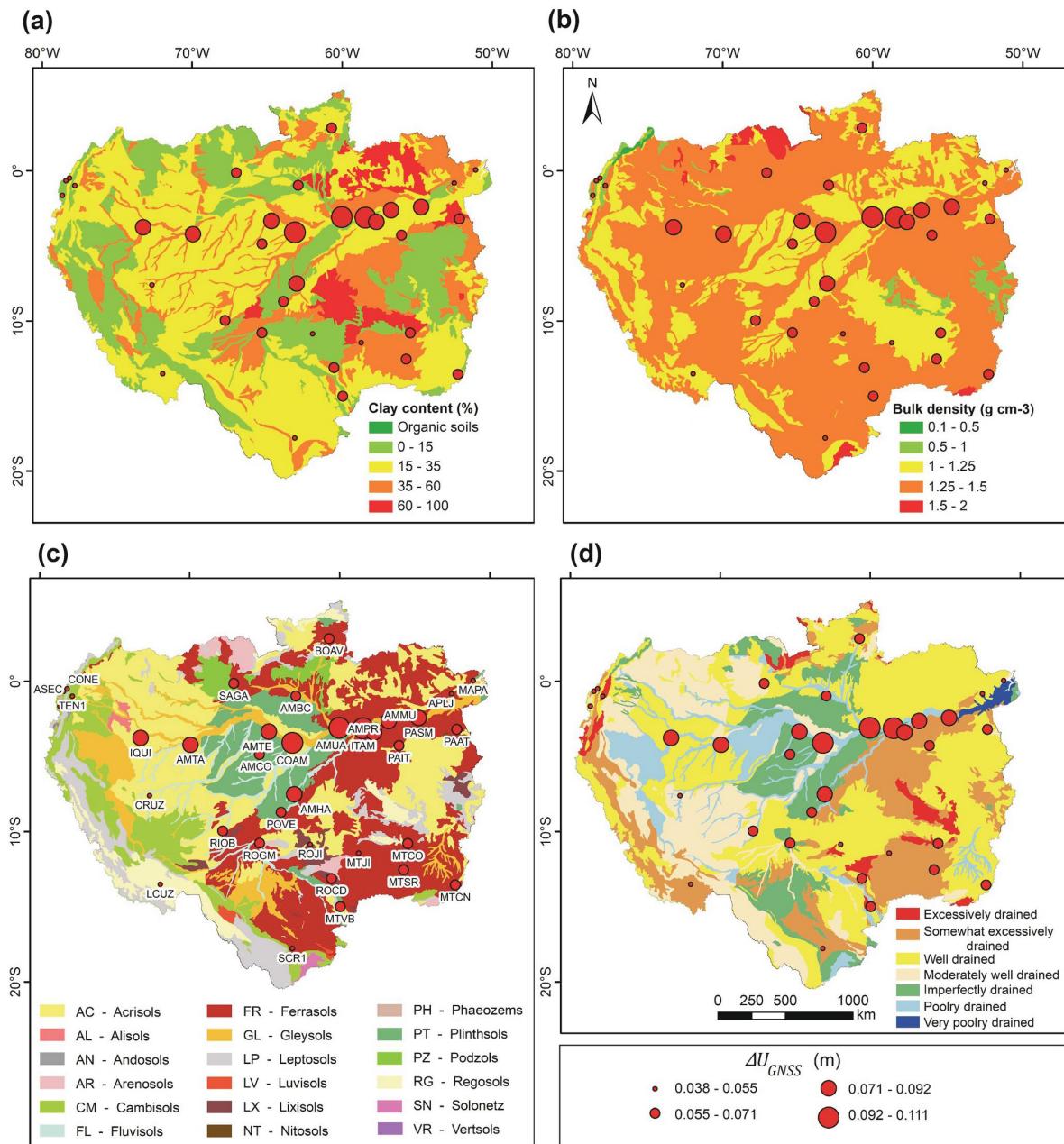
Figure 7. ΔU_{GNSS} and soil information: clay content (a); bulk density (b); types of soils (c); drainage capacity (d).

ΔU_{Model}^{LSDM} varies from 0.01 m to 0.104 m (Figure 8d; Table 2). Figure 8c shows that the highest ΔU_{Model}^{LSDM} values are located in stations near to the main river channel, which receives the water of the rivers of the entire basin by tributary channels. This can be explained by a water flux in basins from upstream to downstream, as water flows from the hills, into the headwater, to the valleys, into the floodplains, until finally reaching the ocean. The following stations, listed in downstream direction, are near encounters between the main tributaries of the Amazonas River and see the highest values: AMTE in Tefé, near of the encounter of the

36
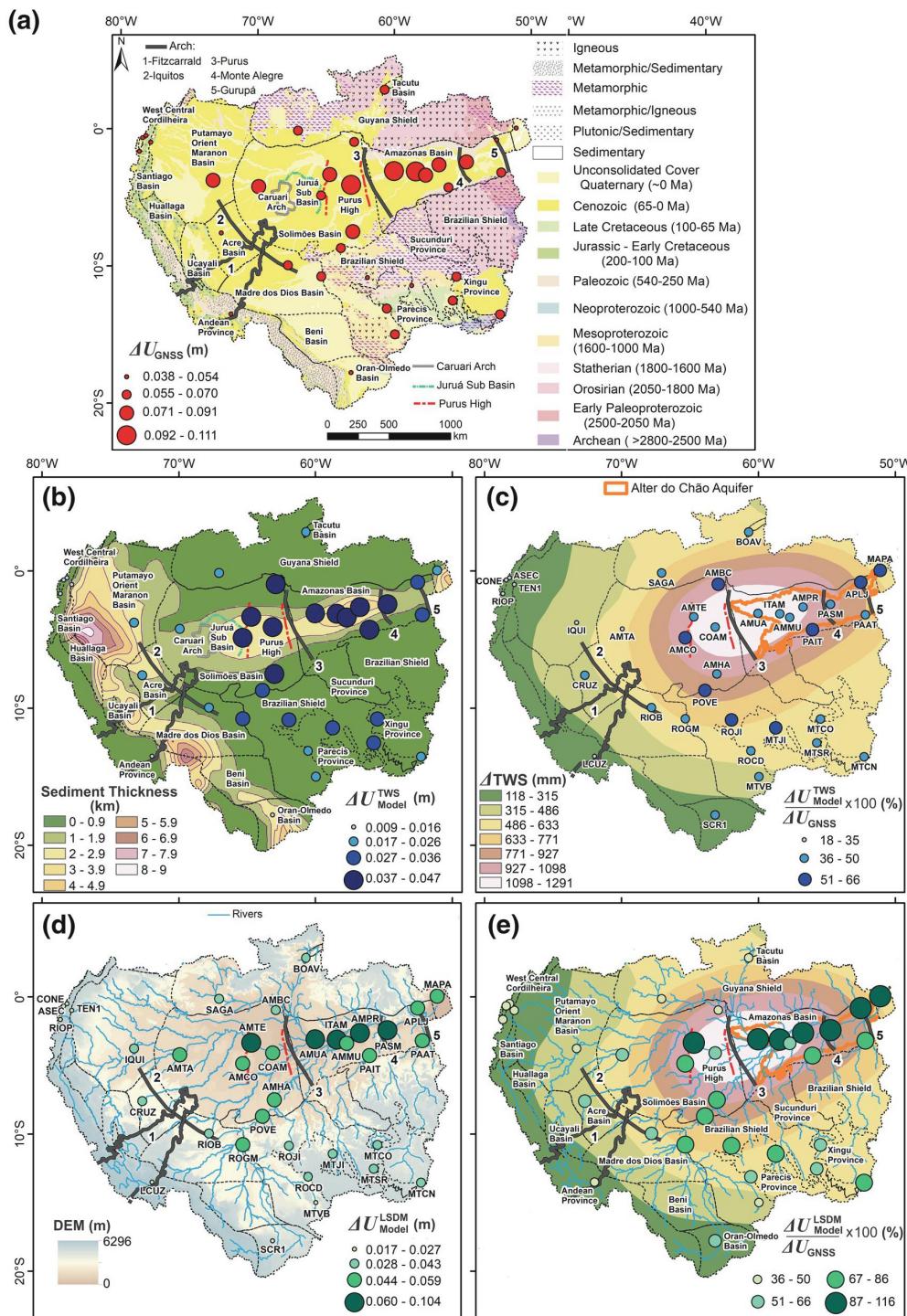
Figure 8. (a) Geology of the Amazon Basin (modified of Schobbenhaus & Bellizia, 2001), tectonic provinces (Schenk et al., 1999), and ΔU_{GNSS}. (b) Sediment thickness (Laske et al., 2013) and ΔU_{Model}^{TWS}. (c) the ratio between ΔU_{Model}^{TWS} and ΔU_{GNSS}. (d) Digital elevation model (DEM/GTOPO30), localization of stations, distribution of the rivers (Geonetwork/FAO) and ΔU_{Model}^{LSDM}. (e) the ratio between ΔU_{Model}^{LSDM} and ΔU_{GNSS}.

37

Table 2

The Maximum Amplitudes of U_{GNSS}, U_{Model}^{TWS} and U_{Model}^{LSDM} (ΔU_{GNSS}, ΔU_{Model}^{TWS} and ΔU_{Model}^{LSDM}) and the ratios of ΔU_{Model}^{TWS} to ΔU_{GNSS} and of ΔU_{Model}^{LSDM} to ΔU_{GNSS}.

Station	ΔU_{GNSS} (m)	ΔU_{Model}^{TWS} (m)	ΔU_{Model}^{LSDM} (m)	ΔU_{Model}^{TWS} (%$_{\Delta U}$)	ΔU_{Model}^{LSDM} (%$_{\Delta U}$)
AMUA	0,112	0,048	0,099	42,67	88,80
COAM	0,105	0,047	0,060	44,73	57,34
ITAM	0,103	0,047	0,104	45,33	101,28
AMPR	0,093	0,044	0,086	47,66	92,80
AMMU	0,090	0,046	0,056	50,64	62,47
AMTE	0,087	0,043	0,078	48,73	88,94
IQUI	0,084	0,020	0,042	23,43	49,54
AMTA	0,084	0,027	0,052	32,54	62,23
AMHA	0,080	0,041	0,054	50,79	67,39
PASM	0,080	0,040	0,093	50,22	116,98
POVE	0,071	0,037	0,052	51,98	72,81
PAIT	0,071	0,042	0,059	58,71	83,67
PAAT	0,071	0,034	0,056	47,68	79,55
SAGA	0,068	0,029	0,033	42,23	48,30
MTCO	0,067	0,031	0,040	46,05	60,17
RIOB	0,066	0,028	0,037	43,13	56,00
AMBC	0,065	0,039	0,030	60,54	46,45
ROCD	0,065	0,028	0,034	43,62	52,94
ROGM	0,064	0,031	0,045	47,75	69,82
BOAV	0,063	0,027	0,030	42,07	47,72
AMCO	0,063	0,042	0,046	66,05	73,78
MTSR	0,062	0,029	0,039	47,19	62,33
MTCN	0,059	0,026	0,040	45,12	68,90
MTVB	0,058	0,024	0,026	41,60	45,02
APLJ	0,056	0,033	0,059	58,98	106,16
ROJI	0,055	0,033	0,038	59,80	69,36
MTJI	0,054	0,031	0,038	57,24	70,37
RIOP	0,051	0,009	0,018	18,72	36,28
MAPA	0,048	0,027	0,055	56,60	115,92
LCUZ	0,047	0,015	0,021	32,06	43,69
TEN1	0,046	0,011	0,019	22,71	40,56
CONE	0,046	0,009	0,017	20,48	37,29
ASEC	0,045	0,010	0,017	21,58	37,88
CRUZ	0,045	0,021	0,028	47,77	63,56
SCR1	0,038	0,016	0,022	41,75	57,17

Note: Stations are in order from the highest to lowest value of ΔU_{GNSS}. Shading from dark to light blue is according to the following ratios: above 87%; 86% to 67%, 66% to 51%, 50% to 36% and 35% to 18%.

Tefé and Solimões rivers; AMUA in Manaus, about 4 km from the Negro River and 14 km from the encounter of the Solimões and Negro rivers (note: after this encounter, it is called the Amazonas River); ITAM in Itacoatiara, about 40 km from the encounter of the Madeira and Amazonas rivers; and PASM in Santarém, about 3 km from the encounter of the Tapajós and Amazonas rivers. The highest values of $\Delta U_{\text{Model}}^{\text{LSDM}}$ are at the following stations: ITAM (0.104 m), AMUA (0.099 m), PASM (0.093 m), AMPR (0.086 m), and AMTE (0.077 m).

In general, the vertical displacement increases from the Andes to the sedimentary Amazonas Basin. Stations at the eastern border of the Amazonas Basin (APLJ and MAPA) have lower values of $\Delta U_{\text{Model}}^{\text{LSDM}}$ compared to stations near river encounters in the sedimentary Amazonas Basin. These stations are in the Marajó rift (limited by the Gurupá Arch) and their lower values may be related to the distribution of the water in estuary and delta channels before it flows to the ocean.

Considering the ratio between $\Delta U_{\text{Model}}^{\text{LSDM}}$ and ΔU_{GNSS} (Figure 8e; Table 2), we observe that the results of $\Delta U_{\text{Model}}^{\text{LSDM}}$ account for 36%–116% of ΔU_{GNSS}. $\Delta U_{\text{Model}}^{\text{LSDM}}$ captures above 87% of ΔU_{GNSS} at seven stations (20%). Nine stations (25%) contribute 67%–86%, and another nine stations (25%) have a contribution 51%–66%, and 10 stations (28%) contribute 36%–50%. Three stations exceed ΔU_{GNSS} and produce rations over 100%: PASM (116%), MAPA (115%), APLJ (106%), and ITAM (101%). According to Dill and Dobslaw (2013), overestimates in the water storage variations in the LSDM may be related to the large precipitation rates in the ECMWF forcing data.

The ratio between $\Delta U_{\text{Model}}^{\text{LSDM}}$ and ΔU_{GNSS} show the highest contribution is at the AMTE station, at the western border of the Purus Arch, and after the Purus Arch, at stations between the main rivers encounter in the sedimentary Amazonas basin and estuary-delta channels before the water discharges into the ocean. The following stations have the highest values: PASM (116%), MAPA (115%), APLJ (106%), ITAM (101%), AMPR (92%), AMTE (88%), and AMUA (88%).

Considering the results of Figure 8 and Table 2, it is possible to observe that ΔU_{GNSS} increases from the cratonic area toward the sedimentary basins (Figure 8a). Moreover, in the sedimentary basin, ΔU_{GNSS} increases from regions with thinner to thicker sedimentary pile (Figure 8a and 8b). Figures 3 and 8a also indicate that ΔU_{GNSS} increases from the Andes to the Amazon lowland areas. Within the lowland areas, ΔU_{GNSS} increases from regions with thin or no sedimentary cover to regions with a thick accumulation of sediments.

A few stations in sedimentary rocks (e.g., CRUZ and AMCO) display very low ΔU_{GNSS} (Figures 3 and 8a). We argue that these areas have rocks with low porosity and permeability below the groundwater flow region. Therefore, these rocks' physical properties affect the state of the stress by increasing resistance to deformation and displacement caused by the hydrologic loading.

The presence of crystalline rocks may explain the smaller ΔU_{GNSS} values observed at some of the stations. For instance, the CRUZ station (Figures 3, 8a, 8b, and 8d), placed in the north of the Acre Basin and near the Fitzcarrald Arch, shows less displacement than expected, when $\Delta U_{\text{Model}}^{\text{TWS}}$, $\Delta U_{\text{Model}}^{\text{LSDM}}$, and ΔU_{GNSS} there are compared to other stations in the same region. Compared to other sites of the Amazon Basin, this area has a thinner layer of young sedimentary rocks because of the proximity of the Fitzcarrald Arch, which represents a topographic high related to the subduction of the Nazca ridge (Espurt et al., 2010).

The AMCO station, near the Tefé River and Purus High western border (Figures 3, 8a, 8b, and 8d), also has a low displacement amplitude. Here, the low amplitude may also be related to the presence of deep intrusive igneous rocks, identified in the region by Munis (2009). Nearby stations with similar values of $\Delta U_{\text{Model}}^{\text{TWS}}$ and $\Delta U_{\text{Model}}^{\text{LSDM}}$ display higher amplitudes of ΔU_{GNSS}, since they are not in the presence of these intrusive rocks. The AMTE station, near to AMCO station, lies in the Purus High western border, above these intrusive igneous rocks, and near to the Tefé River (Figures 3, 8a, 8b, and 8d). This station has 0.087 m of ΔU_{GNSS}, 0.043 m of $\Delta U_{\text{Model}}^{\text{TWS}}$ and 0.078 m of $\Delta U_{\text{Model}}^{\text{LSDM}}$. On other hand, COAM, near to the AMTE station, displays a higher value of ΔU_{GNSS} (0.105, 0.018 m higher than AMTE), even though it has a similar value of $\Delta U_{\text{Model}}^{\text{TWS}}$ (0.047 m, only 0.004 m higher than AMTE) and a lower value of $\Delta U_{\text{Model}}^{\text{LSDM}}$ (0.060, 0.018 m lower than AMTE). While the AMTE station is affected by the presence of igneous rock, resulting in low values of ΔU_{GNSS}, COAM does not have these features and exhibits higher ΔU_{GNSS}, even though it has a lower value of $\Delta U_{\text{Model}}^{\text{LSDM}}$. We analyze this further in the Discussion.

The same behavior can be observed in the stations on the Brazilian Shield, ROJI and MTJI, which achieve, respectively, 0.055 and 0.054 m of ΔU_{GNSS}, 0.033 and 0.031 m of $\Delta U_{\text{Model}}^{\text{TWS}}$, and 0.038 and 0.38 m of $\Delta U_{\text{Model}}^{\text{LSDM}}$. Comparing both stations with ROCD, which lies on a different type of rock, we find similar values of $\Delta U_{\text{Model}}^{\text{TWS}}$ (0.028 m) and $\Delta U_{\text{Model}}^{\text{LSDM}}$ (0.034 m), but a higher value of ΔU_{GNSS} (0.065 m).

5. Discussion

A previous study by Argus et al. (2017) defined two different response with vertical displacement associated to change in hydrologic loading. They find an ascent in the vertical displacement is caused by the porous response, when water fills the pores between the silt, sand and gravel, and rises to the surface. This porous response is the opposite of an elastic response to hydrologic loading. An elastic response is the decrease in vertical displacement due to an increase in water mass. While the GPS sites reach their maximum height at the end of summer due to the elastic response, the maximum height of GPS at aquifers sites is at the end of fall due to the porous response. Argus et al. (2017) postulate that at the top of aquifers there is an elastic response, but it is, in most places, 10 to 100 times smaller than the porous response. Argus et al. (2017) find that 10% of the stations display a porous response.

One of the biggest Brazilian aquifers in the Amazon Basin is called Alter do Chão. The Alter do Chão aquifer lies in the Amazon Sedimentary Basin in north-central Pará and eastern Amazonas states, occupying 312.574 km^2 (ANA, 2005). However, we observe only inverse correlations (negative R values) between vertical displacement and TWS in this analysis, suggesting that all stations have an elastic response. That is, lower values of vertical displacement are associated with higher values of TWS.

The strong correlation between U_{GNSS} and parameters related to seasonal water storage (Table 1) indicate that the hydrological cycle has a vital role in the fluctuation of the vertical displacement. Moreover, the analyzed data for each station is not homogeneous and, therefore, is dependent on the location (Figure 5). This suggests that it is associated with the behavior of the Amazonian hydrological cycle. In addition, as shown in Figures 4 and 5, Δt varies with the hydrological cycle, suggesting that appropriate geological conditions to store water in sediments are also essential to explain the fluctuations. In this regard, we argue that U_{GNSS} is strongly related to geology, and particularly to the thickness of sediments in the Amazon Basin. According to Miguez-Macho and Fan (2012a, 2012b), Δt may be associated with the water column variation cycle, which is responsible for feeding the drought period and maintaining the temperature balance.

Figure 6 shows that ΔSM increases with depth in regions with sedimentary rocks, but decreases with depth in areas with igneous and metamorphic rocks (e.g., Andes region, Guyana Shield, Brazilian Shield, north and south of the Solimões Basin). Furthermore, ΔTWS in the Amazon Basin has a strong E-W gradient. The higher values (1,291 mm) occur in the Amazonas Basin and the eastern portion of the Solimões Basin, near the Alter do Chão aquifer.

The variations in SM and TWS data in the Amazon region (Figure 6) resemble groundwater behavior described by Miguez-Macho and Fan (2012a, 2012b). These authors suggest that groundwater is controlled by topography and depth of the water column. According to them, in elevated regions, the water column is deeper and probably associated with higher drainage capacity. In the transition areas between valley and plateau, the water column is shallower and more accessible to plant roots, minimizing drainage capacity. In the extensive floodplains and in river valleys, which occupy a large part of the Amazon region (20%–40%), water column is even shallower, and drainage capacity is even lower (Miguez-Macho & Fan, 2012a, 2012b). In these areas, SM and evapotranspiration are higher.

The lowest values (18%–32%) of the ratio between $\Delta U_{\text{Model}}^{\text{TWS}}$ and ΔU_{GNSS} are observed in the area with the highest ΔTWS values. Since the main rivers of Amazon Basin in this area lie, the contribution from $\Delta U_{\text{Model}}^{\text{TWS}}$ is underestimated, in accordance of studies of Fu et al. (2013) and Dill and Dobslaw (2013). In narrow structures with highest load, GRACE can only sense a long-wavelength average of the load (Dill & Dobslaw, 2013; Fu et al., 2013). This effect produces a broader but lower amplitude vertical deformation field (Fu et al., 2013), and, in some cases, leads to only a third of deformation amplitude (Dill & Dobslaw, 2013). Thus, since ΔU_{GNSS} is sensitive to short-wavelength loading changes from local effects (Dill et al., 2018)

and $\Delta U_{\mathrm{Model}}^{\mathrm{TWS}}$ underestimates local features because of the limited spatial resolution from GRACE, the ratio between $\Delta U_{\mathrm{Model}}^{\mathrm{TWS}}$ and ΔU_{GNSS} is lower than is realistic.

According to Dill et al. (2018), it is very difficult to separate the water store in the rivers from the total GRACE observations, which include water at the surface and soil moisture to different depths, down to the deepest aquifers. Thus, the hybrid method taking model hydrographs, TWS and a high-resolution river map into account together might to improve correlation between observed and modeled hydrology-induced crustal displacements (Dill et al., 2018). Karegar et al. (2018) invoke a hybrid method, using GRACE data with a limited resolution for the far-field and a hydrologic model with more detailed spatial resolution for the near-field. They find that this hybrid approach improves fits to GPS measured vertical displacement by 25% and 35% on average, relative to Grace-only or high-resolution only hydrologic model. These results show the importance of using a hybrid method.

Considering a uniaxial state of vertical stress in the earth, the relationship between stress, strain and displacement depends on the modulus of elasticity E (Young's modulus) (Fitts, 2015). The lower E values of sedimentary rocks (between 0.1 and 0.6×10^{11} Pa) implies that crystalline terrains (E values between 0.6 and 1.1×10^{11} Pa) or regions with a thinner layer of sedimentary rocks would have a smaller displacement compared to areas with thick sedimentary rock layers. Also, igneous or metamorphic rocks, either underneath or intruded into sedimentary rocks, would resist to deformation and vertical displacement induced by hydrologic loading.

The influence of E can be observed in Figures 8a, 8b, and 8d in which ΔU_{GNSS} increases from the cratonic area toward the sedimentary basin. Moreover, in the sedimentary basin, ΔU_{GNSS} increases from regions with thinner to thicker sedimentary pile (Figures 8a and 8b). We argue that the high porosity of these sedimentary rocks allows a large seasonal variation of groundwater storage and, consequently, of ΔU_{GNSS}. Beyond that, the smaller values of E for terrigenous sedimentary rocks control their lower resistance to deformation. Moreover, at some of the stations inside sedimentary basins, smaller ΔU_{GNSS} values are observed. However, we find that these stations lie near crystalline rocks, which are underneath or intruded into sedimentary rocks, or in places with a thinner sedimentary column. We argue that these areas have rocks with low porosity and permeability below the groundwater flow region. Therefore, these rocks' physical properties affect the state of the stress by increasing resistance to deformation and displacement induced by the hydrologic loading.

6. Conclusions

In this research, the vertical displacement time series generated from 35 GNSS stations distributed throughout the Amazon Basin are compared with regional geological, soil, relief and parameters of the physical environment (sediment thickness, soil moisture, total water storage (TWS), and hydrologic deformation models based on TWS and LSDM). We focus on the temporal and spatial relationships between displacement and deformation variations and the effects related to the hydrologic loading system.

Analyzing the time series in vertical displacement and soil moisture from 0 m to 2 m in depth at all 35 stations, we find that soil moisture and the hydrological cycle vary spatially and have time delays (phase differences) in relation to vertical displacement. Therefore, we suggest that the delay time is associated with water column variation controlled by the Amazonian hydrological cycle. Thus, appropriate geological conditions to store water in sediments are essential to explain the fluctuations. We argue that the vertical displacement caused by hydrologic loading is strongly related to geology and, particularly, to the thickness of sediments in the Amazon Basin.

After correcting for time delays between vertical displacement and soil moisture, TWS and the hydrologic deformation models based on TWS and based on LSDM, the correlation coefficients are estimated for all 35 stations. Twenty five stations (71%) show a correlation between vertical displacement and soil moisture variables below -0.6, and several stations (LCUZ, TEN1, and RIOP) show a positive correlation. On the other hand, 30 stations (86%) showed a correlation between vertical displacement and total water storage below -0.6, and none of the stations show a positive correlation. Since only inverse correlations are found,

41

including in the aquifer regions, such as the large Alter do Chão aquifer, we conclude that all stations show an elastic response caused by hydrologic loading. These same stations, which have a good correlation between U_{GNSS} and TWS, have the correlation R values between U_{GNSS} and $U_{\text{Model}}^{\text{TWS}}$ above 0.6 (86%). The correlation between U_{GNSS} and $U_{\text{Model}}^{\text{LSDM}}$ resulted in 28 stations (80%) with R values above 0.6.

In the spatial analysis of soil moisture at different levels, we observe that the shallower layers of soil represent maximum variations of amplitude that are more homogeneous, probably because the shallower layers are more affected by the exchange of heat and matter with the atmosphere. On the other hand, in deeper soil, there is a larger contrast between sites. Sedimentary areas display higher ΔSM values, while crystalline terrains display much lower values. Furthermore, SM increases with depth in regions with sedimentary rocks, but decreases with depth in areas with igneous and metamorphic rocks (e.g., Andes region, Guyana Shield, Brazilian Shield, north and south of the Solimões Basin).

Analyzing the vertical displacement with the information of soil, geology and topography, we find that the vertical displacement associated with the hydrologic loading is influenced by the geology and topography, since there is a gradient from west to east, in which the largest amplitude of vertical displacement occurs toward the sedimentary basins and the plains. In the sedimentary basins, there are stations where the vertical displacement is smaller than expected, and this may be associated with the thinning and/or compaction of the sedimentary rock layer and/or the presence of intrusive igneous or metamorphic rocks.

We observe that the regional results from the hydrologic deformation model based on TWS represent 18%–66% of the amplitude of vertical displacement variation, ΔU_{GNSS}. In the region of the maximum amplitude variation of TWS $\left(\Delta\text{TWS}\right)$, the sedimentary basin of the eastern Alter do Chão aquifer, the difference between the results from the hydrologic deformation model and the local vertical displacement is more evident. Here, the results from the hydrologic deformation model represent just 18%–32% of the amplitude, because the main rivers of Amazon Basin lie in this region. As a result, the contribution of $\Delta U_{\text{Model}}^{\text{TWS}}$ to the ΔU_{GNSS} is underestimated. This is due the limited spatial resolution from GRACE, which is not sensitive to short-wavelength loading caused by the narrow structures with high loads. Thus, it creates a long-wavelength average of the load, which produces a broader but lower amplitude vertical deformation field, and, in some cases, leading to deformation amplitudes much lower than observed.

We find that the results from a high resolution hydrologic deformation model based on LSDM account for 36%–116% of the amplitude of vertical displacement variation in the GNSS station. Maximum amplitude variations lie in the stations near to the Amazon River and near the encounter between the main tributaries, reinforcing the important contribution of the hydrologic loading from rivers. We further observe that the amplitude of vertical displacement variation increases from the Andes to the sedimentary Amazonas Basin. Stations a t the eastern border of Amazon Basin, limited by Gurupá Arch, have lower values in the maximum amplitude variation than do stations at river encounters in the sedimentary Amazonas Basin. This can be due the distribution of the water in estuary and delta channels before it flows to the ocean.

Finally, we find that, in addition to the contribution of the surface water and groundwater to the vertical displacement, the geology contributes to the amplitude variation of the displacements observed in the GNSS stations.

Data Availability Statement

42

References

Almeida, F. F. M. (1978). A evolução dos crátons Amazônico e do São Francisco comparada com seus homólogos do hemisfério norte. *Anais do 30º Congresso Brasileiro de Geologia, Sociedade Brasileira de Geologia*, 6, 2393–2407.

Almeida, F. G. V., Calmant, S., Seyler, F., Ramillien, G., Blitzkow, D., Matos, A. C. C., & Silva, J. S. (2012). Time-variations of equivalent water heights from Grace Mission and in-situ river stages in the Amazon basin. *Acta Amazonica*, 42, 125–134.

ANA, Agência Nacional das Águas, & J. L. G. Zoby. (2005). *Panorama da qualidade das águas subterrâneas no Brasil*. (p. 80). Brasília: Agência Nacional das Águas.

ANA, & Agência Nacional das Águas. (2015). Avaliação dos Aquíferos das Bacias Sedimentares da Província Hidrogeológica Amazonas no Brasil (escala 1:1.000.000) e Cidades Pilotos (escala 1:50.000), *Geologia da Província Hidrogeológica Amazonas* (Vol II, p. 126). SIP: Brasília, Agência Nacional de Águas (ANA).

ANA, & Agência Nacional das Águas. (2016). http://www.metadados.inde.gov.br/geonetwork/srv/br/metadata.show.embedded?uuid=3ec60e4f-85ea-4ba7-a90c-734b57594f90

ANA, & Agência Nacional das Águas. (2017). www2.ana.gov.br/Paginas/portais/bacias/amazonica.aspx

Argus, D. F., Landerer, F. W., Wiese, D. N., Martens, H. R., Fu, Y., Famiglietti, J. S., & Watkins, M. M. (2017). Sustained water loss in California's mountain ranges during severe drought from 2012 to 2015 inferred from GPS. *Journal of Geophysical Research: Solid Earth*, 122, 10559–10585. https://doi.org/10.1002/2017JB014424

Batjes, N. H. (2005). SOTER-based soil parameter estimates for Latin America and the Caribbean (ver. 1.0). Report 2005/02 ISRIC-World Soil Information, Wageningen. http://data.isric.org/geonetwork/srv/eng/catalog.search#/metadata/3a9ed87d-affc-4f72-aa6e-72db4fefec40

Bevis, M., Alsdorf, D., Kendrick, E., Fortes, L. P., Forsberg, B., Smalley, R., & Becker, J. (2005). Seasonal fluctuations in the mass of the Amazon River system and Earth's elastic response. *Geophysical Research Letters*, 32, 1–4. https://doi.org/10.1029/2005GL023491

Blewitt, G., Hammond, W., & Kreemer, C. (2018). Harnessing the GPS Data Explosion for Interdisciplinary Science. *Eos*, 99, https://doi.org/10.1029/2018eo104623

Blewitt, G., Lavallée, D., Clarke, P., & Nurutdinov, K. (2001). A new global mode of Earth deformation: Seasonal cycle detected. *Science*, 294(5550), 2342–2345. https://doi.org/10.1126/science.1065330

Caputo, M. V. (2014). Juruá orogeny: Brazil and Andean countries. *Brazilian Journal of Geology*, 44, 181–190. https://doi.org/10.5327/Z2317-4889201400020001

Caputo, M. V., & Silva, O. B. (1991). *Origem e evolução de bacias sedimentares* (p. 415). Rio de Janeiro: Petrobrás.

Caputo, M. V., & Soares, E. A. A. (2016). Eustatic and tectonic change effects in the reversion of the transcontinental Amazon River drainage system. *Brazilian Journal of Geology*, 46, 301–328.

Chanard, K., Avouac, J. P., Ramillien, G., & Genrich, J. (2014). Modeling deformation induced by seasonal variations of continental water in the Himalaya region: Sensitivity to Earth elastic structure. *Journal of Geophysical Research: Solid Earth*, 119, 5097–5113. https://doi.org/10.1002/2013JB010451

Cordani, U. G., Ramos, V. A., Fraga, L. M., Cegarra, M., Delgado, I., Souza, K. G., et al. (2016). *Tectonic Map of South America, Comission of the Geologic Map of the World - Scale 1:5,000,000* (2nd ed.). Paris: CGMW-CPRM-SEGEMAR.

Costa, S. M. A., Matos, A. C. O. C., & Blitzkow, D. (2012). Validation of the land water storage from Gravity Recovery and Climate Experiment (GRACE) with gauge data in the Amazon Basin. *Boletim Ciências Geodésicas, Curitiba*, 18, 262–281. https://doi.org/10.1590/S1982-21702012000200006

Davis, J. L., Elósegui, P., Mitrovica, J. X., & Tamisiea, M. E. (2004). Climate-driven deformation of the solid Earth from GRACE and GPS. *Geophysical Research Letters*, 31, 1–4. https://doi.org/10.1029/2004GL021435

Dijkshoorn, J. A., Huting, J. R. M., & Tempel, P. (2005). Update of the 1:5 million soil and terrain database for Latin America and the Caribbean (SOTERLAC, ver. 2.0). Report 2005/01, ISRIC - World Soil Information, Wageningen. http://data.isric.org/geonetwork/srv/eng/catalog.search#/metadata/436bd4b0-7ffc-4272-be57-686b7d7eea7d

Dill, R. (2008). *Hydrological model LSDM for operational Earth rotation and gravity field variations*. In: Scientific Technical Report STR (Vol. 08/09, p. 35). Germany: GFZ Potsdam. https://doi.org/10.2312/GFZ.b103-08095

Dill, R., & Dobslaw, H. (2013). Numerical simulations of global-scale high-resolution hydrological crustal deformations. *Journal of Geophysical Research: Solid Earth*, 118, 5008–5017. https://doi.org/10.1002/jgrb.50353

Dill, R., Klemann, V., & Dobslaw, H. (2018). Relocation of river storage from global hydrological models to georeferenced river channels for improved load-induced surface displacements. *Journal of Geophysical Research: Solid Earth*, 123, 7151–7164. https://doi.org/10.1029/2018JB016141

Dong, D., Fang, P., Bock, Y., Cheng, M. K., & Miyazaki, S. (2002). Anatomy of apparent seasonal variations from GPS-derived site position time series. *Journal of Geophysical Research*, 107(B4), 1–16. https://doi.org/10.1029/2001JB000573

Dziewonski, A., & Anderson, D. (1981). Preliminary reference Earth model. *Physics of the Earth and Planetary Interiors*, 25, 297–356. https://doi.org/10.1016/0031-9201(81)90046-7

Espinoza Villar, J. C., Guyot, J. L., Ronchail, J., Cochonneau, G., Filizola, N., Fraizy, P., et al. (2009a). Contrasting regional discharge evolutions in the Amazon basin (1974–2004). *Journal of Hydrology*, 375, 297–311. https://doi.org/10.1016/j.jhydrol.2009.03.004

Espinoza Villar, J. C., Ronchail, J., Guyot, J.-L., Cochonneau, G. G., Naziano, F., Lavado, W., et al. (2009b). Spatio-temporal rainfall variability in the Amazon basin countries (Brazil, Peru, Bolivia, Colombia, and Ecuador). *International Journal of Climatology*, 29, 1574–1594. https://doi.org/10.1002/joc.1791

Espinoza, J. C., Chavez, S., Ronchail, J., Junquas, C., Takahashi, K., & Lavado, W. (2015). Rainfall hotspots over the southern tropical Andes: Spatial distribution, rainfall intensity, and relations with large-scale atmospheric circulation. *Water Resources Research*, 51, 3459–3475. https://doi.org/10.1002/2014WR016273

Espurt, N., Baby, P., Brusset, S., Roddaz, M., Hermoza, W., & Barbarand, J. (2010). The Nazca Ridge and Uplift of the Fitzcarrald Arch: Implications for Regional Geology in Northern South America. In C. Hoorn & F. P. Wesselingh (Eds.), *Amazonia: Landscape and Species Evolution*, (pp. 89–100). Blackwell. https://doi.org/10.1002/9781444306408.ch6

Farrell, W. E. (1972). Deformation of the Earth's surface loads. *Reviews of Geophysics*, 10, 761–767. https://doi.org/10.1029/RG010i003p00761

Fisch, G., Marengo, J. A., & Nobre, C. A. (1998). Uma revisão geral sobre o clima da Amazônia. *Acta Amazonica*, 28(2), 101–126. https://doi.org/10.1590/1809-43921998282126

Fitts, C. R. (2015). Águas Subterrânea (Groundwater Science). *Translated by Daniel Vieira* (2 ed., p. 692). Rio de Janeiro: Elsevier. ISBN 978-85-352-7744-9.

Frappart, F., Papa, F., Güntner, A., Tomasella, J., Pfeffer, J., Ramillien, G., et al. (2019). The spatio-temporal variability of groundwater storage in the Amazon River Basin. *Advances in Water Resources*, 124, 41–52. https://doi.org/10.1016/j.advwatres.2018.12.005

43

Fritsche, M., Döll, P., & Dietrich, R. (2012). Global-scale validation of model-based load deformation of the Earth's crust from continental watermass and atmospheric pressure variations using GPS. *Journal of Geodynamics*, *59–60*, 133–142. https://doi.org/10.1016/j.jog.2011.04.001

Fu, Y., Argus, D. F., Freymueller, J. T., & Heflin, M. B. (2013). Horizontal motion in elastic response to seasonal loading of rain water in the Amazon Basin and monsoon water in Southeast Asia observed by GPS and inferred from GRACE. *Geophysical Research Letters*, *40*, 6048–6053. https://doi.org/10.1002/2013GL058093

Guimarães, G. N., Blitzkow, D., de Matos, A. C. O. C., Almeida, F. G. V., & Barbosa, A. C. B. (2012). *Analysis of the crust displacement in Amazon Basin*. In S. Kenyon, M. Pacino, & U. Marti (Eds.), Geodesy for planet Earth, international association of geodesy symposia (Vol. 136, pp. 885–891). Berlin: Springer.

Guo, J., Li, Y., Huang, Y., Deng, H., Xu, S., & Ning, J. (2004). Green's function of the deformation of the Earth as a result of atmospheric loading. *Geophysical Journal International*, *159*, 53–68. https://doi.org/10.1111/j.1365-246X.2004.02410.x

Hagemann, S., & Dümenil, L. (1998). Documentation for the hydrological discharge model. In: Technical Report No. 17. Hamburg, Germany: Max Planck Institute for Meteorology.

Heki, K. (2001). Seasonal modulation of interseismic strain buildup in northeastern Japan driven by snow loads. *Science*, *293*, 89–92. https://doi.org/10.1126/science.1061056

Ibanez, D. M., Riccomini, C., & Miranda, F. P. (2014). Is the current stress state in the Central Amazonia caused by surface water loading?. *Journal of South American Earth Sciences*, *55*, 19–28. https://doi.org/10.1016/j.jsames.2014.07.002

INMET, & Instituto Nacional de Meteorologia. (1992). *Normais climatológicas (1961-1990)*. Brasília, Brasil: Departamento Nacional de Meteorologia.

Karegar, M. A., Dixon, T. H., Kusche, J., & Chambers, D. P. (2018). A new hybrid method for estimating hydrologically induced vertical deformation from GRACE and a hydrological model: An example from Central North America. *Journal of Advances in Modeling Earth Systems*, *10*, 1196–1217. https://doi.org/10.1029/2017MS001181

Kusche, J., & Schrama, E. J. O. (2005). Surface mass redistribution inversion from global GPS deformation and Gravity Recovery and Climate Experiment (GRACE) gravity data. *Journal of Geophysical Research*, *110*, B09409. https://doi.org/10.1029/2004JB003556

Kvas, A., Behzadpour, S., Ellmer, M., Klinger, B., Strasser, S., Zehentner, N., & Mayer-Gürr, T. (2019). ITSG-Grace2018: Overview and evaluation of a new GRACE-only gravity field time series. *Journal of Geophysical Research: Solid Earth*, *124*, 9332–9344. https://doi.org/10.1029/2019JB017415

Laske, G., Masters, G., Ma, Z., & Pasyanos, M. (2013). Update on CRUST1.0—A 1-degree Global Model of Earth's Crust. *Geophysical Research Abstracts*, *15*, EGU2013-2658.

Latrubesse, E. M., Arima, E. Y., Dunne, T., Park, E., Baker, V. R., d'Horta, F. M., et al. (2017). Damming the rivers of the Amazon basin. *Nature*, *546*, 363–369. https://doi.org/10.1038/nature22333

Latrubesse, E. M., Stevaux, J. C., & Sinha, R. (2005). Tropical rivers. *Geomorphology*, *70*, 187–206. https://doi.org/10.1016/j.geomorph.2005.02.005

LDAS, & Land Data Assimilation System. (2018). Retrieved from: https://ldas.gsfc.nasa.gov/gldas/GLDASelev.php

Mangiarotti, S., Cazenave, A., Soudarin, L., & Crétaux, J. F. (2001). Annual vertical crustal motions predicted from surface mass redistribution and observed by space geodesy. *Journal of Geophysical Research*, *106*, 4277–4291. https://doi.org/10.1029/2000JB900347

Marengo, J. A. (2005). The characteristics and variability of the atmospheric water balance in the Amazon basin: spatial and temporal variability. *Climate Dynamics*, *24*, 11–22. https://doi.org/10.1007/s00382-004-0461-6

Mayer-Gürr, T., Behzadpur, S., Ellmer, M., Kvas, A., Klinger, B., Strasser, S., & Zehentner, N. (2018). *ITSG-Grace2018-monthly, daily and static gravity field solutions from GRACE*. GFZ Data Services. http://doi.org/10.5880/ICGEM.2018.003

Miguez-Macho, G., & Fan, Y. (2012a). The role of groundwater in the Amazon water cycle: 1. Influence on seasonal streamflow, flooding and wetlands. *Journal of Geophysical Research*, *117*, 1–30. https://doi.org/10.1029/2012JD017539

Miguez-Macho, G., & Fan, Y. (2012b). The role of groundwater in the Amazon water cycle: 2 . Influence on seasonal soil moisture and evapotranspiration. *Journal of Geophysical Research*, *117*, 1–27. https://doi.org/10.1029/2012JD017540

Milani, E. J., & Thomaz Filho, A. (2000). Sedimentary basins of the South America. In U. G. Cordani, E. J. Milani, A. Thomaz-Filho, & D. A. Campos (Eds.), *Tectonic evolution of South America. 31st International Geological Congress. Rio de Janeiro* (pp. 389–449). Academia Brasileira de Ciências e Departamento Nacional da Produção Mineral (DNPM) 856p.

Moreira, D. M., Calmant, S., Perosanz, F., Xavier, L., Rotunno Filho, O. C., Seyler, F., & Monteiro, A. C. (2016). Comparisons of observed and modeled elastic responses to hydrological loading in the Amazon basin. *Geophysical Research Letters*, *43*, 9604–9610. https://doi.org/10.1002/2016GL070265

Mortatti, J., Moraes, J. M., Victoria, R. L., & Martinelli, L. A. (1997). Hydrograph separation of the Amazon River: A methodological study. *Aquatic Geochemistry*, *3*, 117–128. https://doi.org/10.1023/A:1009606801595

Munis, M. B. (2009). *Caracterização geomagnética do gráben Purus e suas implicações na evolução das bacias do Solimões e do Amazonas. Tese de Doutorado, Sistemas Petrolíferos, PEC, COPPE* (p. 102). Universidade Federal do Rio de Janeiro.

Nesbitt, S. W., & Anders, A. M. (2009). Very high resolution precipitation climatologies from the Tropical Rainfall Measuring Mission precipitation radar. *Geophysical Research Letters*, *36*, 1–5. https://doi.org/10.1029/2009GL038026

Nobre, C. A., Obregón, G. O., Marengo, J. A., Fu, R., & Poveda, G. (2009). Characteristics of Amazonian climate: Main features. *Geophysical Monograph Series*, *186*, 149–162. https://doi.org/10.1029/2009GM000903

Pokhrel, Y. N., Fan, Y., Miguez-Macho, G., Yeh, P. J. F., & Han, S. C. (2013). The role of groundwater in the Amazon water cycle: 3. Influence on terrestrial water storage computations and comparison with GRACE. *Journal of Geophysical Research: Atmospheres*, *118*, 3233–3244. https://doi.org/10.1002/jgrd.50335

Rajner, M., & Liwosz, T. (2011). Studies of crustal deformation due to hydrological loading on GPS height estimates. *Geodesy and Cartography*, *60*, 135–144. https://doi.org/10.2478/v10277-012-0012-y

Rajner, M., & Liwosz, T. (2017). Analysis of seasonal position variation for selected GNSS sites in Poland using loading modelling and GRACE data. *Geodesy and Geodynamics*, *8*, 253–259. https://doi.org/10.1016/j.geog.2017.04.001

Reynolds, C. A., Jackson, T. J., & Rawls, W. J. (2000). Estimating soil water-holding capacities by linking the Food and Agriculture Organization soil map of the world with global pedon databases and continuous pedo-transfer functions. *Water Resources Research*, *36*, 3653–3662. https://doi.org/10.1029/2000WR900130

Rodell, M., Houser, P. R., Jambor, U., Gottschalck, J., Mitchell, K., Meng, C.-J., et al. (2004). The global land data assimilation system. *American Meteorolical Society*, *85*, 381–394. https://doi.org/10.1175/BAMS-85-3-381

Santos, E. B., Lucio, P. S., & Silva, C. M. S. E. (2015). Precipitation regionalization of the Brazilian Amazon. *Atmospheric Science Letters*, *16*, 185–192. https://doi.org/10.1002/asl2.535

Schenk, C. J., Viger, R. J., & Anderson, C. P. (1999). Maps showing geology, oil and gas fields and geologic provinces of the South America region. In: *U. S. Geological Survey*. https://pubs.usgs.gov/of/1997/ofr-97-470/OF97-470D/sam06Gmap.html#TOP

Schobbenhaus, C., & Bellizia, A. (2001). *Geological map of South America, 1:5000000*. Brasilia: CGMW-CPRM-DNPM-UNESCO.

Seyler, P. T., & Boaventura, G. R. (2003). Distribution and partition of trace metals in the Amazon basin. *Hydrological Processes*, *17*, 1345–1361. https://doi.org/10.1002/hyp.1288

Smith, W. H. F., & Sandwell, D. T. (1997). Global seafloor topography from satellite altimetry and ship depth soundings. *Science*, *277*(5334), 1956–1962. https://doi.org/10.1126/science.277.5334.1956

Tapley, B. D. (2004). GRACE measurements of mass variability in the Earth system. *Science*, *305*, 503–505. https://doi.org/10.1126/science.1099192

Tourian, M. J., Reager, J. T., & Sneeuw, N. (2018). The total drainable water storage of the Amazon river basin: A first estimate using GRACE. *Water Resources Research*, *54*, 3290–3312. https://doi.org/10.1029/2017WR021674

Van Dam, T., Wahr, J., Milly, P. C. D., Shmakin, A. B., Blewitt, G., Lavallée, D., & Larson, K. M. (2001). Crustal displacements due to continental water loading. *Geophysical Research Letters*, *28*, 651–654. https://doi.org/10.1029/2000GL012120

Wahr, J., Molenaar, M., & Bryan, F. (1998). Time variability of the Earth's gravity field: Hydrological and oceanic effects and their possible detection using GRACE. *Journal of Geophysical Research: Solid Earth*, *103*, 30205–30229. https://doi.org/10.1029/98JB02844

Wang, H. (2000). Surface vertical displacements and level plane changes in the front reservoir area caused by filling the Three Gorges Reservoir. *Journal of Geophysical Research*, *105*(B6), 13211–13220. https://doi.org/10.1029/2000JB900072

Wu, X., Heflin, M. B., Ivins, E. R., Argus, D. F., & Webb, F. H. (2003). Large-scale global surface mass variations inferred from GPS measurements of load-induced deformation. *Geophysical Research Letters*, *30*, 1–4. https://doi.org/10.1029/2003GL017546

Zalán, P. V., & Matsuda, N. S. (2007). Bacia de Marajó. *Boletim de Geociencias da Petrobras*, *15*, 311–319.

Zhang, L., Dobslaw, H., Stacke, T., Guntner, A., Dill, R., & Thomas, M. (2017). Validation of terrestrial water storage variations as simulated by different global numerical models with GRACE satellite observations. *Hydrology and Earth System Sciences*, *21*(2), 821837. https://doi.org/10.5194/hess-21-821-2017

45

4. Influência hidrológica na variação de gravidade terrestre em Manaus, Amazonas, Brasil

Artigo submetido para a *Journal of Applied Geophysics*

Lavoisiane Ferreira de Souza[1], Giuliano Sant'Anna Marotta[1], Elizabeth Hale Madden[1]

[1]Observatório Sismológico, Instituto de Geociências, Universidade de Brasília

Hydrological influence on the variation of the terrestrial gravity field in Manaus, Amazonas, Brazil

L. Ferreira[1], G. S. Marotta[1], E. H. Madden[1]

[1]Seismological Observatory/Institute of Geosciences/University of Brasília.

Corresponding author: Lavoisiane Ferreira (lavoisiane@outlook.com)

[1]Prédio SG -13, Campus Darcy Ribeiro, Universidade de Brasília, CEP 70.910-900 – Brasília / DF – Brasil

Abstract

The influence of groundwater on the hydrological cycle has been studied at large-scale across the Amazon Basin, one of the largest freshwater reservoirs in the world. Considering this Basin's importance in the global hydrological cycle, local studies also are critical. Here, we focus on the local hydrological cycle in Manaus, at the center of the Amazon Basin. We observed the variability of local gravity, fluvial height, soil moisture, precipitation, evapotranspiration and groundwater in the rainy (December-May) and dry (June-November) seasons, during drought (2016) and flood (2017) years. In general, when the first rains start, gravity, fluvial height and soil moisture are at minimum values. Soil moisture is instantaneously influenced by the first precipitation. After the first rains, an increase in gravity coincides with an increase in soil moisture. The soil becomes saturated and the variation in soil moisture achieves maximum values, which are sustained until the end of rainy season. Due the relationship of soil moisture with precipitation, the maximum variation in gravity is delayed relative to these data by similar amounts, nearly 3 months in 2016 and 5 months in 2017. After soil saturation by infiltration, the groundwater starts to be fed by percolation and the water table starts to rise. Thus, variation in local gravity reflects mainly variations in groundwater level. After, the soil loses moisture (soil moisture values decrease), while the gravity signal maintains high values, representing the sustained behavior of the groundwater. 3D modeling shows that the Negro River height variation does not influence the gravity signal. However, we observe high similarity between fluvial behavior and the gravity signal. Thus, since the gravity signal represents mainly the groundwater, this demonstrates a connection between groundwater variations and surface water, such as rivers.

KEYWORDS: Microgravity, Groundwater Estimation, 3D Modeling, Hydrological cycle, Negro River.

4.1   Introduction

Studies of surface water and groundwater and their roles in the hydrological cycle are performed in many parts of the world in different scales. At the regional scale, the Gravity Recovery and Climate Experiment (GRACE) data is used in hydrological studies (Tapley, 2004), since the time gravity variations obtained by differencing the GRACE gravity fields provide information about changes in the distribution of mass within the Earth and at its surface (Swenson et al., 2003). Thus, the total water storage (TWS) provided by GRACE data is composed of water on vegetations surfaces, of groundwater, snow, surface water in rivers, wetlands, natural lakes, man-made reservoirs (Guntner et al., 2007). At the local scale, there are not many studies, but water balance studies in Amazonian micro-scale basins have shown that a significant proportion of total discharge is contributed by the groundwater system (Lesack, 1993; Tomassela et al., 2008). Thus, according to Frappart et al. (2019), though surface water storage behavior is widely described (Marengo et al., 2008-2011; Frappart et al., 2012), knowledge about groundwater is lacking. Studies at the local scale can bring more information about the behavior of the hydrological cycle and a better understanding of the connections between different components of the water balance in the Amazon basin (Tomassela et al., 2008).

Gravity changes measured by high precision gravimeters can be used for to monitor changes in water-land distribution in the vicinity of the station (Kazama et al., 2012; Van Camp et al., 2017). Thus, gravity meters have been widely used for studies of hydrological effects on the local scale such as groundwater, soil moisture, rainfall, or snow covering (Hokkanen et al., 1994; Imanishi et al., 2006; Meurers, 2006; Van Camp et al., 2006; Kroner et al., 2007; Neumeyer et al., 2008; Kang et al., 2011). Signals ranging from a few thousands of nm/s² to less than 1 nm/s² reveal hydrogeological effects at spatial resolutions of up to 1 km² (Van Camp et al., 2017). Continuous ground gravity measurements provide valuable information to evaluate the water mass balance in the saturated and unsaturated zone at the mesoscale (Llubes et al., 2004). However, it is a challenge to discriminate between the gravitational effect of water storage change on the unsaturated zone and aquifer (Van Camp et al., 2017).

Hokkanen et al. (1994) investigate the hydrological effects that influence the gravity field at a local scale, analyzing the relationships between the time-varying gravity data and the amount of water variation at the surface and in the subsurface after rains. Meurers (2006) suggest that small rainfall events correspond to variations in gravity

signals, which can be explained from the Newtonian effect of vertical mass redistribution (vertical variation of density without change in mass pressure). Kroner et al. (2007) study the effects of the hydrological cycle on the gravity signal, showing that the variation can be from a few nm/s² to tens of nm/s². Considering the Bouguer approximation, an infinite horizontal layer of water that is 1 cm thick produces a gravity change of about 4.2 nm/s² (Van Camp et al., 2017).

Despite these studies indicating the importance of local studies to understand the hydrological cycle, few local studies have been performed in the Amazon Basin. Considering the large international importance of the Amazon region, which represents one of the largest freshwater reservoirs in the world and, according to Tapley (2004), which has one of the largest hydrological cycles on the planet, it is necessary to understand the hydrological processes at the local level here.

We present a local study near the city of Manaus, at the center of the Amazon Basin. To improve understanding of gravity variations and how these variations relate to the hydrological cycle, local data from a relative gravity meter (gPhone) is compared to data on fluvial height, soil moisture, precipitation, evapotranspiration, and groundwater level. In addition, we model the influence of river height variation on gravity variation at the gPhone station location and estimate the groundwater variation using the gravity data.

4.2   Materials and Methods

The city of Manaus, located in the Amazon Basin, is close to the junction of the Negro River with the Solimões River. After joining, the river is called the Amazon River. Geologically, the city of Manaus is located on in the Cretaceous sedimentary formation Alter do Chão, composed mainly of sandstone, claystone, and clayey sandstone (Faria et al., 2004). The predominant soil types in the region are gleysols and ferrasols, with bulk density varying from 1.02 g/cm³ to 1.44 g/cm³ (Batjes, 2005; Dijkshoorn et al., 2005).

In Manaus, the mean precipitation from 1986 to 2015 is 2339.3 mm/yr (D'avila Junior and Vieira, 2019). Precipitation is highest between December and May (Fisch, 1990), with maximum values in March (Mascarenhas Junior et al., 2009), and lowest between June and November (Fisch, 1990), with minimum values in August (Mascarenhas Junior et al., 2009). According to Mascarenhas Junior et al. (2009), the extreme variation in precipitation can be due to events at different scales: influence from the El Niño (droughts) and La Ninã (floods); instability lines formed in the northeast of Pará state and

flow to Manaus; and, at the local scale, by the increase of waterproofed areas and greenhouse gases.

According Tomassela et al. (2008), the annual behavior of groundwater shows a maximum in July, before of the peak of dry season in August, and a minimum between December and February. Thus, it is estimated that the aquifer beneath the plateau recharges in 4 months (Tomassela et al., 2008). In Manaus, the Alter do Chão Aquifer System has an average thickness of 200 m, a water table variation of 3.5 m and an average depth of 25 m with main stream direction of NE to SW, in the direction of Negro River (Aguiar, 2012). Based on water table measurements, physical-chemical parameters in-situ in wells, and isotopic analyses of groundwater, Pita et al. (2018) find a partitioning of the aquifer to the west of Manaus: one aquifer is present down to 130 m depth and another is present below 130 m. In the upper aquifer, the recharge is made by meteoric water, and the water is less mineralized, while in the bottom aquifer, there are more mineralization due the residence time of the water and interactions water-rock (Pita et al., 2018). However, more studies are necessary for to bring more information about the depth and behavior of groundwater in Manaus.

Aiming to improve the understanding of the relationship between local gravity and the hydrological cycle and between the connections of different components of the hydrological cycle, we compare variations in gravity, water table level, fluvial height, soil moisture and precipitation. We estimate the groundwater variation (ΔGW and ΔGW^{SOIL_GLDAS}) using the variation in gravity data (Δg) at the station in Figure 4.1. Δg is measured with a Micro-g LaCoste gPhone gravimeter operating at a 1 s sample rate for 646 days from January 26, 2016 to November 1, 2017. Water table level variation (ΔWT) at the Tarumã well (#1300006065) (Figure 4.1) is from the Company of Research and Mineral Resources (CPRM). Fluvial height data (ΔF) at a sample rate of 15 min at the fluvial station #14990000 (Figure 4.1) is from the National Water Agency (ANA). Soil moisture data (ΔSM^{GLDAS}) up to 2 m depth is available at a sampling rate of 3 hr (Rodell et al., 2004) from the National Aeronautics and Space Administration/Goddard Space Flight Center. Local precipitation in daily (ΔP_{daily}^{INMET}) and monthly (ΔP^{INMET}) resolution and monthly evapotranspiration (ΔE^{INMET}) is from the meteorological station of INMET (National Institute of Meteorology). The Δg, ΔF, ΔSM^{GLDAS} data have different time sampling rates. Therefore, after acquired and/or processed, they all are converted to a 1-day sample rate using a Least Squares Method (LSM) applied to a moving window, in order to minimize the discrepancies in the resampled value estimation.

The gravimeter evaluates the water mass distribution in some hundred meters around the station (Van Camp et al., 2017), so it is necessary to keep in mind that all variables could vary within the study area. The Tarumã well (Figures 4.1 and 4.2) lies 2.5 km from the Negro river border and 4 km from the gravity station. The gravimeter and the well are at similar topographic heights (81 m and 82 m for the well and gravity station, respectively) and the entire city of Manaus lies in the same geological formation (Alter do Chão). The fluvial station, at the Negro river border, lies 13 km from the gravity station. Soil moisture from the hydrological model GLDAS has 0.25° of spatial resolution. The INMET meteorological station lies 9 km from the gravity station, but this does not affect the general analysis. .
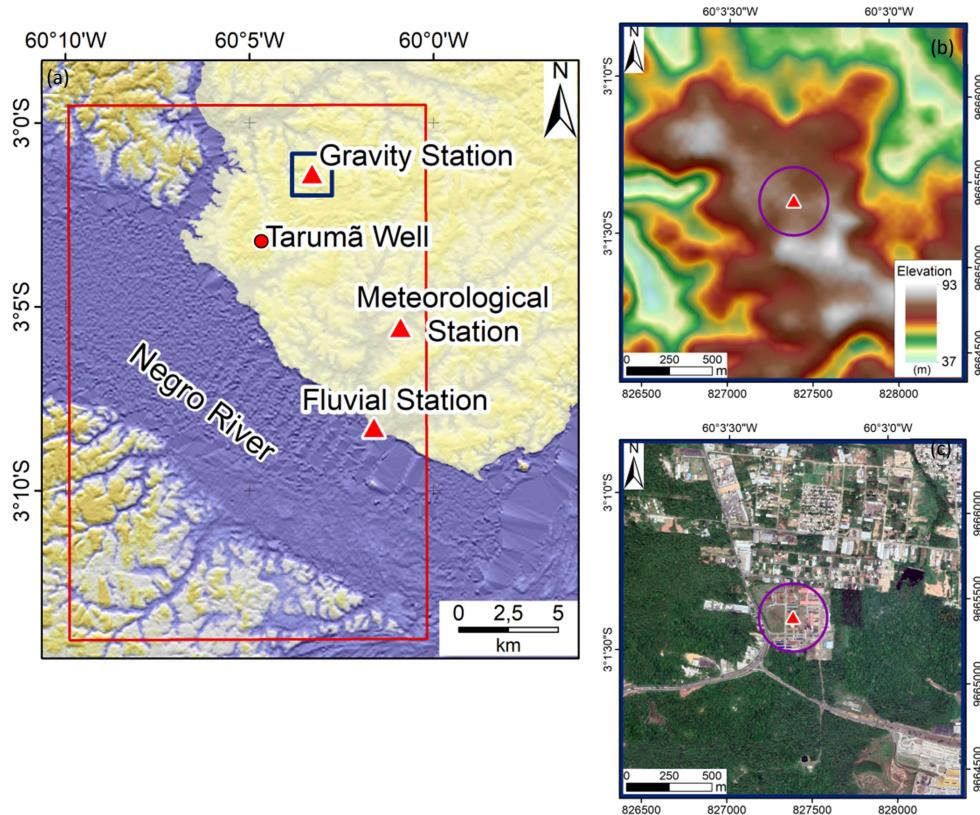
Figure 4.1 – (a) Location of the gravity station, Tarumã well, and fluvial and meteorological stations. The red square is the area used in the modeling of the river influence at the gravity station. The blue square is the area used in (b) and (c); (b) elevation and (c) the vegetation and urban zone around the gravity station. The purple circle limits 200 meters around the gravity station.
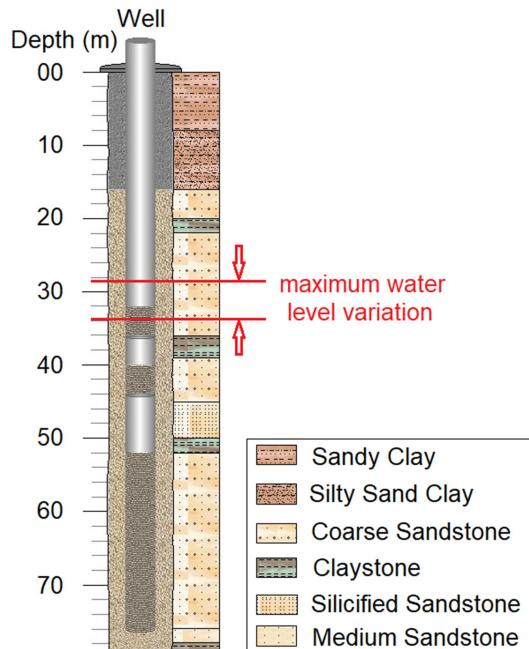
Figure 4.2 – Tarumã well. Source: Adapted from CPRM.

4.2.1 *Δg* Processing

In processing the local variation in gravity data (*Δg*), for the extraction of information related to the hydrologic loading, we consider the corrections due to atmospheric loading, pole movement, solid Earth tide, and oceanic loading. The atmospheric loading correction considers the variations of external pressure recorded by the gravimeter to determine a calibration factor that is applied to the time series (Spratt, 1982; Crossley et al., 1995; gMonitor User's Manual, 2012). The pole movement correction considers parameters provided by the International Earth Rotation and Reference Systems Service (IERS) and the formulation defined in the Absolute Observations Data Processing Standards (1992), specified in International Absolute Gravity Base station Network (IAGBN), which, according to Van Camp and Vauterin (2005), considers the location of the gravimetric station and the position of the pole at the time of observation. The corrections of earth tide and oceanic loading follow recommendations and formulations presented in technical note no. 36 of the IERS. For oceanic loading, we use parameters from the FES2004 model (Lyard et al., 2006), with 0.125° resolution. The correction of the nontidal oceanic loading was not considered in this study since, according to Zhou (2008) and Kang et al. (2011), it has amplitudes lower than 10 nm/s².

We also correct the data for instrumental and natural (seismic event) effects. These corrections involve the variation of instrument level, instrumental drift and effects on the observed time series, such as steps caused by equipment interruption and spurious data caused by abrupt variation of the observed value due to instrumental or natural effects. We apply the Least Squares Method (LSM) to correct for the effect of steps and instrumental drift, using the functional model presented in Eq. 4.1:

$$F(t) = a + bt + ct^2 + \sum_{i=1}^{n} dH(t) \tag{4.1}$$

where: a representes the mean of the variation in values of the observed gravity field, to reduce it to zero, $bt + ct^2$ represents the instrumental drift correction factor as a function of time (t), and $\sum_{i=1}^{n} dH(t)$ is the factor associated with the step correction, where $H(x)_i$ represents the step function.

4.2.2 The river influence at the gravity station

Using a SG sensor, Meurers (2006) shows that, more than a few hundreds of meters from the station, there is no significant contribution to the gravity field, since the gravity damps by square of the distance. In addition, a variation in water height of 5 m in the nearby river, which is farther than this distance away, causes a low amplitude variation of less than 3 nm/s² (Meurers, 2006). Volgyesi and Toth (2004) model the gravity gradient due water mass variation (5 m) in the Danube River and compare with measured changes in two gravimeters, which the gravity gradients damps by cube of the distance.. They find the gravitational change to be very sensitive to the actual distance of the station from the river bank. Maximum gravity changes are exactly above the edge of water mass, and the change decreases strongly as a function of distance from the water reservoir (Volgyesi and Toth, 2004). In addition, Volgyesi and Toth (2004) find good agreement between measured gravity variation and gravity variation modeled with Mod3D, interactive software for 3D gravity and magnetic modeling (Cerovský et al, 2004). Thus, considering the high amount of water mass of the Negro River, we use Mod3D to calculate the Negro River influence on the anomalous gravitational field at the gravity station. The Negro River varies approximately 12 m in height and its width varies 3-9 km close to the station. The station is located 7 km from the nearest edge of the Negro River.

According to Van Camp et al. (2017), gravity changes measured at nm/s² are an appropriate tool to estimate the groundwater balance when the gravity variation is caused by a process homogeneously distributed in the vicinity of the station, thus, when the problem can be simplified as a Bouguer Plate Effect (BPE). Thus, 90% of the BPE comes from a volume represented by a cone with base radius equal to about 10 times its height (Van Camp et al., 2017). This is mean that 90% of the BPE, when its center is vertical to the gravimeter, can be related to the vertical component of the gravitational attraction of a horizontal thin disc (Van Camp et al., 2017).

4.2.3 *ΔGW* Estimation

After correcting the local gravity data (*Δg*), it is possible to estimate the groundwater variation (*ΔGW*) as follows. Eq. 4.2 considers a Bouguer plate with unsaturated and saturated zones, where Δg is the change in gravitational potential in μGal and G is the Universal Gravitational Constant (6.673×10^{-11} m³kg^{-1}s^{-2}). Taking the density contrast between water and rock ($\Delta\rho_{rw}$), and edges tending to infinity for a given thickness (Δh) of the plate (Koth and Long, 2012), *Δg* is:

$$\Delta g = 2\pi G \Delta\rho_{rw} \Delta h \qquad (4.2)$$

Now considering that the change in density ($\Delta\rho_{rw}$) occurs as a function of the water storage variation (Carmichael and Henry Jr, 1977; Koth and Long, 2012; Saibi, 2018), it can be calculated as the porosity (φ) multiplied by the water density (ρ_{water}):

$$\Delta\rho_{rw} = \varphi\rho_{water} \qquad (4.3)$$

Since we do not have a local measure to correct for the change in water in the unsaturated zone, we first assume that this change is zero and that Δh is equal to *ΔGW*, which is defined as (Koth and Long, 2012):

$$\Delta GW = \Delta g / 2\pi G \rho_{water} \varphi \qquad (4.4)$$

We use an effective porosity (φ) of 18%, defined for the aquifer Alter do Chão by Aguiar (2012) and a water density of 1 g/cm³.

Since the gravity station detects the unsaturated plus groundwater variation, the influence of unsaturated zone will result in an overestimation of ΔGW by this first method. This may influence our estimated time delay between maximum ΔGW and other data. Thus, we consider a second methodology, considering ΔSM^{GLDAS} as the unsaturated zone and find ΔGW^{SOIL_GLDAS}. By this method, before calculating ΔGW^{SOIL_GLDAS} by Eq. 4.4, we assume a gravity influence from ΔSM^{GLDAS} of 4.2 nm/s² per cm (Van Camp et al., 2017) and subtract this from Δg. By this method, there is the risk of not representing the real soil moisture behavior in the area within a few hundred meters around the station, which influences the signal.

4.2.4 Study of the hydrological cycle response in the observed data

After processing and resampling these data, we analyze the different components of the hydrological cycle. Thus, to improve the analysis of signal correlation on time-series data, we estimate the time delay difference values finding the maximum and minimum values in a window separating the different seasons and years. In addition, we estimate the correlation index between them performing a cross-correlation. To achieve the best result, we normalize all series and interpreted the signals, aiming to bring more information about the influence of each variable in the hydrological cycle.

4.3 Results

We used a 3D model to study the river influence at the gravity station (Figure 4.3f), in order to be sure about the main contributors to the gravity signal variation (Δg). The results show the river influence at the gravity station of 9.9 nm/s² (Figure 4.3b-e). However, considering that 90% of the Bouguer Plate Effect (BPE) is composed by the vertical component, which is 0 (Figure 4.3a-c), we can confirm that the river is not influencing signal of the gravity station, despite the magnitude of the water variation. Beyond that, we can observe that, as concluded by Volgyesi and Toth (2004), the gravity signal decreases strongly due the distance to the river bank. Here, the gravity influence was more sensitive until around 2-3 km from river border (cyan color limits in Figure 4.3e).
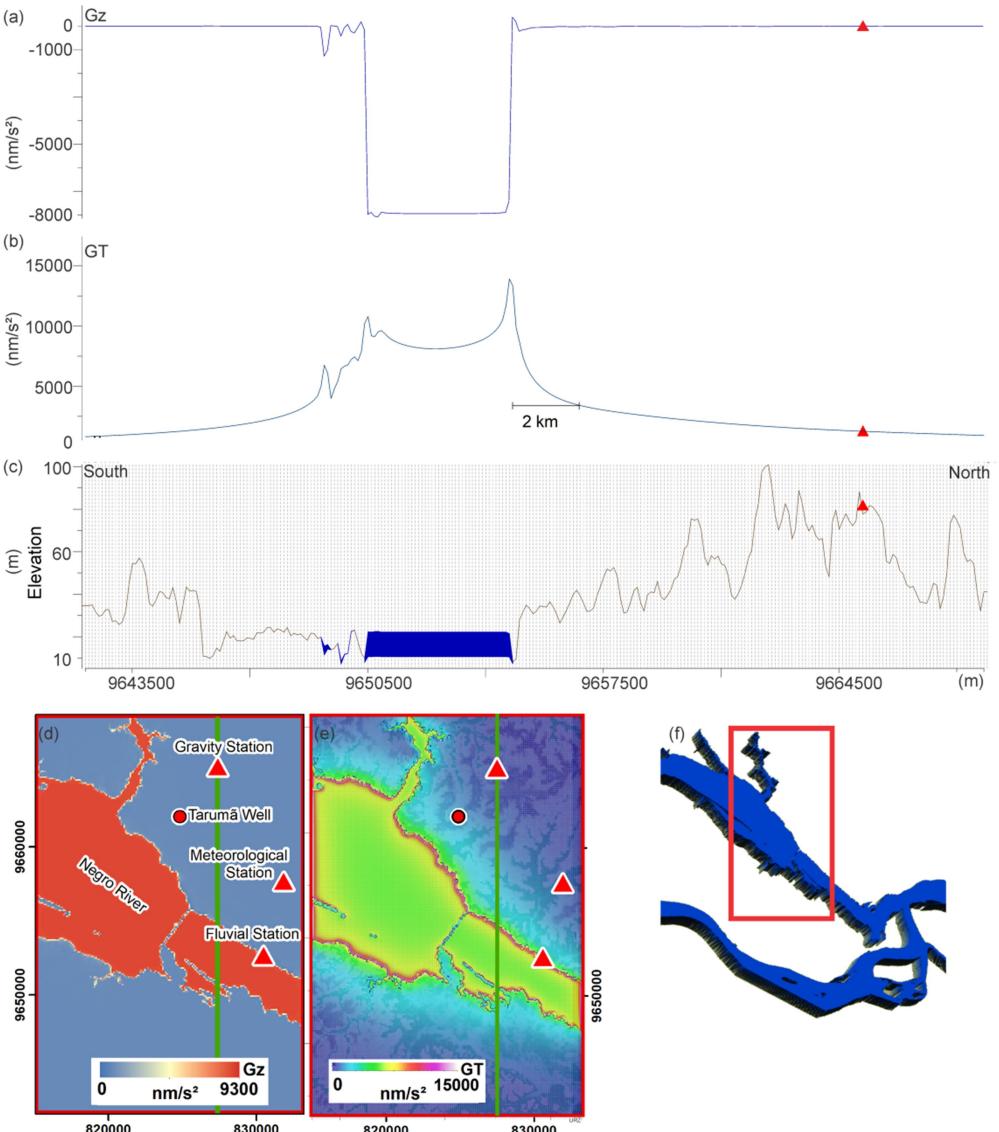
Figure 4.3 – Results of the Negro River gravity influence due to water variation: a) Profile of the modeled vertical gravity (Gz); b) Profile of the modeled total gravity (GT); c) Digital Elevation Model and river height variation used in the model; d) Map of the Gz variation; e) Map of the GT variation (green line shows profile location); f) 3D river height variation model. Red box shows area shown in d) and e).

Considering the variability of the rainy (December-May) and dry (June-November) seasons in Figure 4.4 and Table 4.1, we observe that our study interval for Δg from January 26, 2016 to November 1, 2017 contains the maximum precipitation values from 2016 and 2017. In 2016, maxima in monthly precipitation occurred in April (303.9 mm) and December (518 mm), near the start of 2017. Therefore, we consider the 2016 year starting in the rainy season in December 2015 and finishing in November 2016, and the 2017 year from December 2016 until November 2017. Δg data is available from January 26, 2016 to

November 30, 2016 and we consider a 2017 data range from December 1, 2016 to November 1, 2017.

In Brazil, the El Nino Southern Oscillation (ENSO) influence in 2015 and 2016 was strong, according to the Oceanic Nino Index (INMET, 2016), which can reduce rainfall during El Nino event (Marengo, 2004). The available monthly precipitation data from INMET (ΔP^{INMET}) for 2015 provides information about the precipitation behavior in year preceding our study. From December, 2014 to November, 2015, the maximum precipitation was in March (373.7 mm) and the total of precipitation was 1791.8 mm. As was 2015, 2016 (December, 2015 to November, 2016) was a drought year, with a total annual rainfall of 1916.3 mm. Maximum monthly precipitation in 2016 occurred in April (303.9 mm), and the minimum occurred in August (49.8 mm). In contrast, 2017 (December/2016 to November/2017) was a flood year, with a total annual precipitation of 2655 mm. In this year, there is a higher amplitude variation and a temporal shift in the maximum and minimum values of precipitation from 2016. The maximum occurred in December, 2016 (518.8 mm), while the minimum occurred in August (20.1 mm).

Maximum monthly evapotranspiration (ΔE^{INMET}) in 2016 occurred in November (191.2 mm), and the minimum occurred in August (60.6 mm). The total annual evapotranspiration in 2016 (December, 2015 to November, 2016) was 1638.2 mm. In 2017, the same pattern occurred with the maximum values in November (176.7 mm) and the minimum in August (34.3 mm). The total annual evapotranspiration in 2017 (December, 2016 to November, 2017) was 1660.8 mm.

In Figure 4.4, we present all data used in this research. Maximum variations in 2016 and 2017, respectively, are (Table 4.1): 297 and 375 nm/s² for Δg, 9.9 and 11.66 m for ΔF, 26 and 33 cm for ΔSM^{GLDAS}, 1.13 and 3.89 m for ΔWT (there is a gap in the maximum value interval in the 2016 year), 3.93 and 4.96 m for ΔGW, and 3.96 and 4.23 m for ΔGW^{SOIL_GLDAS}.
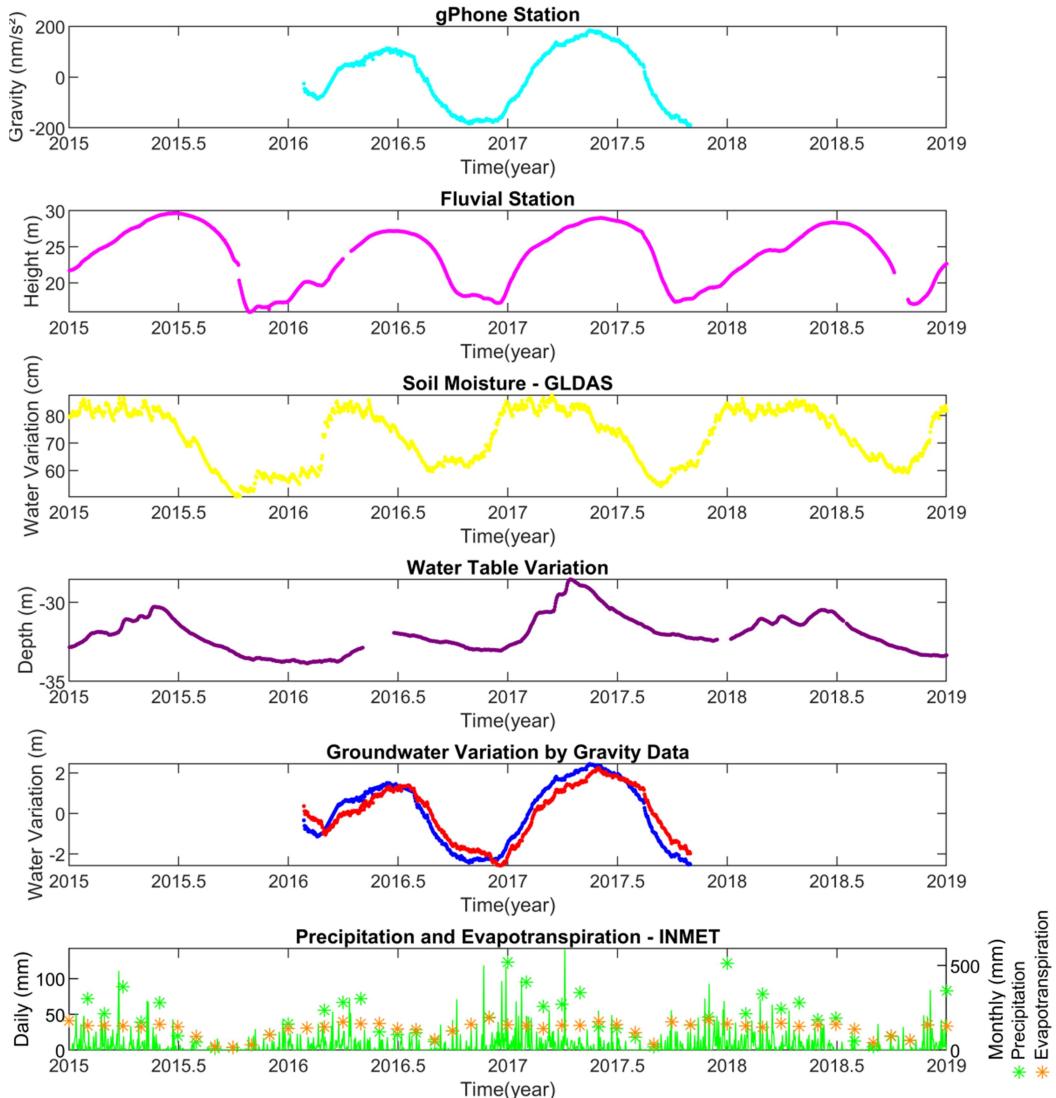
Figure 4.4 – Terrestrial gravity (Δg - cyan), fluvial height (ΔF - magenta), soil moisture (ΔSM^{GLDAS} - yellow), water table variation (ΔWT - purple), groundwater variation by gravity data (ΔGW - blue and ΔGW^{SOIL_GLDAS} - red), precipitation (ΔP_{daily}^{INMET} and ΔP^{INMET} - green) and evapotranspiration (ΔE^{INMET} – orange).

From Table 4.1, over the same time interval as the local gravimeter data recorded with the gPhone, the observed delay between Δg and ΔF, ΔSM^{GLDAS}, ΔWT, ΔGW, ΔGW^{SOIL_GLDAS} and ΔP_{daily}^{INMET} quantifies how these variables are related in the hydrological cycle. ΔSM^{GLDAS} is influenced instantaneously by the first precipitation of the rainy season. When ΔSM^{GLDAS} achieves a maximum value, this represents soil saturation and this value is sustained until the end of rainy season (note the plateau in the ΔSM^{GLDAS} signal in Figure 4.4 and 4.5), when the rain starts to decrease. In 2016, soil saturation was sustained for 53 days (7 weeks) from March 21st to May, 13th. In 2017, soil saturation was sustained for 137 days (19 weeks) from December 28th to May 14th.

The first maximum in ΔSM^{GLDAS} precedes the maximum in Δg by 83 days (11 weeks) in 2016 and 139 days (19 weeks) in 2017. Considering that ΔSM^{GLDAS} is related instantaneously to ΔP_{daily}^{INMET}, the delay in Δg relative to ΔP_{daily}^{INMET} is of similar length to the delay in Δg relative to ΔSM^{GLDAS} in both 2016 and 2017. These delays are approximately 3 months in 2016 and 5 months in 2017.

The estimated ΔGW in 2016, determined by our first method assuming zero change in water in the unsaturated zone, is 3.93 m. ΔWT is 1.13 m. The apparently large difference in these values is difficult to resolve, given the gap ΔWT data in 2016 (see Figure 4). The difference between ΔGW (4.96 m) and ΔWT (3.89 m) is smaller in 2017, but ΔGW likely is overestimated, due the way that the unsaturated zone is treated.

ΔGW^{SOIL_GLDAS} assumes the correction of the unsaturated zone from ΔSM^{GLDAS} beyond of a gravity influence of 4.2 nm/s² per cm. In 2016, the estimated ΔGW^{SOIL_GLDAS} (3.96 m) is similar to ΔGW (3.93 m), which shows that during the drought years, we can consider the unsaturated zone as zero. As for ΔGW, the difference between ΔGW^{SOIL_GLDAS} and ΔWT (1.13 m) is again difficult to resolve because of the gap in data. In 2017, ΔGW^{SOIL_GLDAS} (4.23 m) is much closer to ΔWT (3.89 m) than ΔGW (4.96 m), suggesting that ΔGW^{SOIL_GLDAS} method performs better than ΔGW mainly during the flood years.

Analyzing the delays between Δg and the estimated ΔGW and ΔGW^{SOIL_GLDAS}, we observe that there is no time delay between Δg and ΔGW, since it was estimated using constants parameters directly beyond of Δg. On the other hand, we find the minimum of ~5 days of delay in Δg relative to ΔGW^{SOIL_GLDAS} in 2016, and ~2 weeks in 2017. We cannot determine the delays of ΔGW and ΔGW^{SOIL_GLDAS} relative to ΔWT in 2016 due to the gap in data. In 2017, ΔGW has a delay of ~1 month relative to ΔWT, while ΔGW^{SOIL_GLDAS} has a delay of ~6 weeks relative to ΔWT. The maxima in Δg and ΔGW precede the maximum in ΔF by the minimum of 2 days in 2016, and ~2 weeks in 2017. On the other hand, ΔGW^{SOIL_GLDAS} and ΔF has a similar signal behavior with a short delay of ~3 days in both 2016 and 2017 years.

Variations		Δg (nm/s²)	ΔF (m)	ΔSM^{GLDAS} (cm)	ΔWT (m)	ΔGW (m)	ΔGW^{SOIL_GLDAS}
2016	Max	113	27.19	85.2-85.6	-31.93	1.49	1.32-1.38
	Date	12-Jun	14-Jun to 30-Jun	21-Mar to 13-May	------	12-Jun	17-Jun to 19-Jul
	Min	-184	17.2	59.6	-33.06	-2.43	-2.57
	Date	27-Oct	13-Dec	27-Aug	18-Dec	27-Oct	18-Dec
	Amp	297	9.9	26.0	1.13	3.93	3.96
2017	Max	185	29	82.8-87.4	-28.55	2.44	2.25
	Date	16-May	03-Jun	28-Dec to 14-May	13-Apr	16-May	31-May
	Min	-190	17.34	54.2	-32.44	-2.52	-1.98
	Date	----	06-Oct	12-Sep	07-Dec	----	----
	Amp	375	11.66	33.0	3.89	4.96	4.23

To determine how much these variables are related to one another, we perform a cross correlation analysis using Δg as reference. With the exception of ΔP_{day}^{INMET} (29%) and ΔWT (66%), the variables have a correlation coefficient (R) higher than 85%, at 96% for ΔF and 86% for ΔSM^{GLDAS}.

Starting the hydrological cycle with precipitation, water will be distributed in the forms of evapotranspiration, soil moisture, groundwater, and surface water. First, analyzing the monthly precipitation and evapotranspiration, we can observe that the evapotranspiration has the same pattern during drought (2016) and flood (2017) years (Figure 4.4). The total annual evapotranspiration in 2016 was 1638.2 mm and in 2017 was 1660.8 mm. In addition, we can observe that during the rainy season, the evapotranspiration is constant (observe the plateau in the signal of the Figure 4.4), achieving approximately 145 mm per month, which represents 50% or more of the precipitation (which it achieves different maximum values during the drought and flood years – Figure 4.4). The total annual precipitation in 2016 was 1916.3 mm and in 2017 was 2655 mm.

In the rainy season, around the gravity station, the water of precipitation not subtracted by the constant evapotranspiration will be distributed as soil moisture, and groundwater. During the dry season the evapotranspiration represents approximately the total or more of the precipitation. Thus, to obtain an understanding of the observed data and its relation with the hydrological cycle, after data processing we normalize the

amplitudes of each time series (Figure 4.5). From Figure 4.5, we interpret the behavior of the hydrological cycle in rainy and dry season.

In general, when the first rains start, Δg, ΔF, and ΔSM^{GLDAS} are at minimum values. After the first rains, the increase in Δg coincides with an increase in ΔSM^{GLDAS}. The soil moisture is instantaneously influenced by the starting of rainy season with the first precipitation. The soil becomes saturated to the end of rainy season and we note that ΔSM^{GLDAS} achieves a maximum value before Δg. The saturation was sustained for 53 days in 2016 and 137 days in 2017. Due to the relationship of ΔSM^{GLDAS} with ΔP_{day}^{INMET}, their maxima have similar delays relative to the maximum in Δg, preceding the maximum in Δg by nearly 3 months in 2016 and 5 months in 2017.

After soil saturation by infiltration, the groundwater starts to be fed by percolation rising the ΔWT and Δg tracks with ΔF and ΔGW^{SOIL_GLDAS}. Between soil moisture and the groundwater, the groundwater comprises the majority of the water in the Alter do Chão Aquifer under the gravity station used in this study. Thus, Δg reflects mainly changes in the groundwater level. Before Δg, ΔF and ΔGW^{SOIL_GLDAS} reach their peaks, the soil loses moisture (ΔSM^{GLDAS} values decrease). Δg values remain high, reflecting the sustained groundwater levels.

Observing the similar behavior between Δg, ΔGW^{SOIL_GLDAS} and ΔF, we can observe that there is a connection between the groundwater variation and surface water as rivers. We analyze this alongside the previous results in the discussion section.
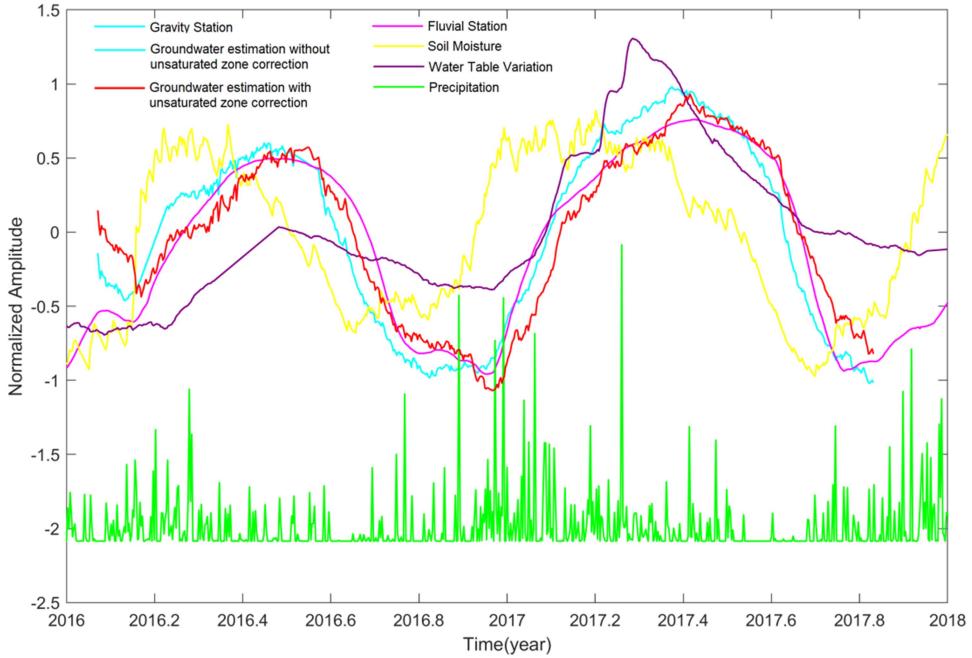
Figure 4.5 – Normalized data and temporal analysis of Δg and ΔGW (cyan), ΔF (magenta), ΔSM^{GLDAS} (yellow), ΔWT (dark purple), ΔGW^{SOIL_GLDAS} (red), ΔP_{day}^{INMET} (green). Time delays can be observed. Δg and ΔGW have exactly the same signal, since ΔGW was estimated using constants directly from of Δg.

4.4 Discussion

According to INMET (2016), in Brazil, the El Nino influence in 2015/2016 was strong, the only years with stronger influences being 1997/1998 and 1982/1983. During the summer and autumn of 2016, the El Nino influence waned and the temperature of the sea surface in the Pacific Equatorial gradually decreased (INMET, 2016). This cooling occurred mainly in May, due to negative surface temperatures in the Central Pacific Equatorial. A neutral condition was sustained in June to December. In December 2017, the monthly precipitation in Manaus was 512.8 mm, which is the highest accumulated rain since December 1961 in the region and more than twice the climatological mean for the same month (219.6 mm) (INMET, 2017). This is similar to the high value of December, 2016, which we identify as the beginning of the 2017 rainy season (see Section 4.3).

For the evapotranspiration, we need to highlight that the vicinity of meteorological station is lied in the urban zone, while the gravity station is lied in the border of the urban zone (Figure 1c). Thus, the local evapotranspiration around the gravity station can have some different magnitude variation of the values considered in this work. Our analysis of evapotranspiration in dry and rainy season is in agreement to Marengo (2005), which

affirms that the ratio between evapotranspiration and precipitation of the dry season is higher than for rainy season, and to Rocha et al. (2009), which concluded that the evapotranspiration is constant during the rainy station, varying 2.8 to 3.6 mm/day, and, it gradually increases during the drier station until 4 mm/day, being dominated by over radiation and deficit in vapour pressure.

Maximum Δg in 2016 occurs in June, 2 months before the driest month (August) and 2 months after the rainiest month (April). Minimum Δg occurs at the end of October, 1 month before the rainiest month (December) and 3 months after the driest month (August). The maximum was achieved again only in May 2017, 5 months after the rainiest month (December 2016) and 3 months before the driest month (August 2017). Thus, we estimate an aquifer recharge period of nearby 2 months in 2016 and 5 months in 2017.

During drought years, the groundwater is responsible for sustaining the surface waters, due the deficit in water storage in the surface water, as rivers, and in the soil. The higher interval recharge in 2017 shows the hydrological system trying to retrieve the water lost in the preceding drought years. Soil moisture observations suggest that drier rainy seasons, which do not fully replenish the soil water profile, cause a 'carry over' of the soil moisture deficit and reduced groundwater recharge in the subsequent wet season (Hodnett et al., 1996).

Δg and ΔGW demonstrate similar behavior, as ΔGW was estimated using constants parameters directly beyond of Δg. Since Δg is being influenced by the unsaturated zone plus, as we find, by the groundwater, estimates of ΔGW are a result of these combined processes and the delay of ΔGW is an approximation and not an exact determination of this time delay. Since the maximum of unsaturated zone occurs before the maximum groundwater variation, the combined gravity signal between them results in a shifted signal, anticipating the result of delay from the estimated groundwater. The maximum of the Δg, which reflects mainly the groundwater, precedes the maximum in ΔF and it is shorter during drought years (as few days) than in flood years (~two weeks).

On the other hand, ΔGW^{SOIL_GLDAS}, which has the unsaturated zone correction, achieves its maximum and minimum in the same period as ΔF and there is a similar behavior between them. Thus, if modeling the river influence at a gravity station suggests that the river is not influencing Δg, the similar behavior between ΔGW^{SOIL_GLDAS} and ΔF shows that they are instantaneously connected and influenced by the water variation. We highlight that to correct the unsaturated zone from the gravity signal (limited to some hundred meters of resolution around the gravimeter) using the GLDAS data (with 0.25°

resolution) is not the most appropriate approach (Van Camp et al., 2017). However, we decided to use the model, since the gravity station was not accompanied by local soil moisture measurements, piezometers and meteorological data as suggested by many authors (Meurers, 2006; Hinderer et al., 2007; Kazama et al., 2012; Van Camp et al., 2017). We hope that this research could motivate more studies with more controlled parameters that clarify and improve knowledge about groundwater behavior.

The shorter delay between maximum variations in groundwater and ΔF during droughts is in agreement with the results of Pfeffer et al. (2014) who used satellite radar altimetry data during droughts to find the groundwater level, considering the groundwater connection with surface waters.

The delay and amplitude difference between ΔWT and groundwater estimation can be related to the partitioning of the aquifer in different depths as mentioned by Pita et al. (2018). To the west of Manaus, they suggest one aquifer until 130 m depth, with recharge made mainly by meteoric water, and another below 130 m, with a higher residence time of the water (Pita et al., 2018). Another possibility for the delay difference is the distance to the gravity station and the proximity to the river of Tarumã well.

With these results, we can now consider the local hydrological cycle at Manaus, following the hydrological cycle stages for the Amazon Basin presented by Miguez-Macho and Fan (2012a-b). There is exchange between the vadose zone and the water table in the different periods (floods and droughts). With the first rains of the year, the unsaturated soil begins to accumulate water rapidly, which influences Δg. As the soil saturates, maximum ΔSM^{GLDAS} occurs, 3 and 5 months before maximum values of ΔF and Δg in 2016 and 2017, respectively. After some weeks, soil water reaches greater depths, percolates to the water table and, consequently, increases the water table level. This is when the maximum values of Δg occur, suggesting that the variation in groundwater is the main contributor to the variation of the gravity field. After some days or weeks, ΔF achieves its maximum, since the surface-intermediate flows and the increased water table level feed the flows of the channels. We observe that there is a connection between the groundwater variation and surface water as rivers.

4.5 Conclusions

This work provides new insight into the local hydrologic cycle near Manaus. We observe the variability of the rainy (December-May) and dry (June-November) season, during drought (2016) and flood (2017) years. In general, when the first rains start, the gravity, fluvial and soil moisture signals are at minimum values. The soil moisture is instantaneously influenced by the start of rainy season, with the first precipitation. After the first rains, the increase in gravity coincides with an increase in soil moisture. The soil becomes saturated and its signal achieves maximum values, which are sustained until the end of rainy season. Due to the relationship of soil moisture with precipitation, they have similar values of delay with the gravity variation, nearly 3 months (2016) and 5 months (2017).

After soil saturation by infiltration, the groundwater starts to be fed by percolation and the water table start to increase. Thus, gravity is reflecting the groundwater. After, the soil loses moisture (soil moisture values decrease), while gravity values are sustained, reflecting the sustained behavior of groundwater. We estimate the period of aquifer recharge of 2 and 5 months for 2016 and 2017, respectively. The higher interval recharge in 2017 shows the hydrological system trying to retrieve the water lost in the preceding drought years, due the deficit in water storage in the surface water, as rivers, and in the soil.

There is no time delay between gravity signal and the estimated groundwater level when water in the unsaturated zone is not taken into account. The gravity signal is influenced by the unsaturated zone and the groundwater, thus the signal is a result of these combined processes, and the delay of estimated groundwater is an approximation only. The maximum in gravity variation, reflecting mainly the groundwater, precedes the maximum in fluvial variation.

On the other hand, the estimated groundwater with the unsaturated zone correction achieves the maximum and minimum in the approximately same period of the fluvial variation. Thus, if modeling shows that the river is not influencing the gravity signal, and the gravity signal is representing mainly the groundwater, the similar behavior between these variables shows the connection between groundwater variations and surface water, as rivers. In view of these observations and analyses at Manaus, in the center of the Amazon Basin, we can observe the connection between the groundwater variation and surface water, as rivers.

4.6 Acknowledgments, Samples, and Data

Data for this research are available in:

Information about soils (Batjes, 2005; Dijkshoorn et al., 2005) provided by ISRIC in https://www.isric.org/explore/isric-soil-data-hub; Information about well of Tarumã provided by Company of Research and Mineral Resources (CPRM) in http://rimasweb.cprm.gov.br/; GLDAS data (Rodell et al., 2004) provided by NASA/GSFC/HSL in https://disc.gsfc.nasa.gov/datasets/GLDAS_NOAH025_3H_2.1/summary; Fluvial height provided by National Water Agency (ANA) in http://www.snirh.gov.br/hidrotelemetria/serieHistorica.aspx;

4.7 References

Aguiar, C. J. B. (2012). Relatório diagnóstico Aquífero Alter do Chão no Estado do Amazonas, Bacia Sedimentar do Amazonas. In: C. J. B. Aguiar, M. A. A. Mourão (Eds.), Projeto Rede Integrada de Monitoramento das Águas Subterrâneas. Belo Horizonte: CPRM – Serviço Geológico do Brasil. (Coleção de Relatórios-Diagnóstico dos Aquíferos Sedimentares do Brasil), 30p.

Batjes, N. H. (2005). SOTER-based soil parameter estimates for Latin America and the Caribbean (ver. 1.0). Report 2005/02, ISRIC - World Soil Information, Wageningen. Available in http://data.isric.org/geonetwork/srv/eng/catalog.search#/metadata/3a9ed87d-affc-4f72-aa6e-72db4fefec40

Carmichael, R. S., Henry Jr, G. (1977). Gravity exploration for groundwater and bedrock topography in glaciated areas, *Geophysics*, 42(4):850–859.

Cerovský, I., Meurers, B., Pohánka, V., Frisch, W., Goga, B. (2004). Gravity and magnetic 3D modeling software - Mod3D, in Meurers, B. and Pail, R. (eds): Proc. 1st Workshop on Int. Gravity Field Research, Österr. Beitr. Met. Geoph., 163-168, in press.

Crossley, D.J., Jensen, O.G., Hinderer, J. (1995). Effective barometric admittance and gravity residuals, *Physics on the Earth Planetary Interiors*, 90:221–241. doi:10.1016/0031-9201(95)05086-Q

D'avila Junior, J. C. M., Vieira, A. F. S G. (2019). Padrões pluviométricos da Cidade de Manaus-AM: 1986 a 2015, *Boletim Paulista de Geografia*, 102:1-31.

Dijkshoorn, J. A., Huting, J. R. M.,Tempel, P. (2005). Update of the 1:5 million Soil and Terrain Database for Latin America and the Caribbean (SOTERLAC, ver. 2.0). Report 2005/01, ISRIC - World Soil Information, Wageningen. Available in http://data.isric.org/geonetwork/srv/eng/catalog.search#/metadata/436bd4b0-7ffc-4272-be57-686b7d7eea7d

Faria, M. S. G., Bahia, R., Almeida, M. E., Oliveira, M. A. (2004). Folha SA.20-Manaus. In: Schobbenhaus, C., Gonçalves, J. H., Santos, J. O. S., Abram, M. B., Leão Neto, R., Matos, G. M. M., Vidotti, R. M., Ramos, M. A. B., Jesus, J. D. A. de., (eds.), Carta Geológica do Brasil ao Milionésimo, Sistemas de Informações Geográficas-SIG. Programa Geologia do Brasil, CPRM, Brasília. CD-ROM.

Fisch, G. (1990). Climatic aspects of the Amazonian Tropical Forest, *Acta Amazonica*, 20:39-48. doi:10.1590/1809-43921990201048

Frappart, F., Papa, F., Santos da Silva, J., Ramillien, G., Prigent, C., Seyler, F., Calmant, S. (2012). Surface freshwater storage in the Amazon basin during the 2005 exceptional drought, *Environmental Research Letter*, 7 (4):044010.

Frappart, F., Papa, F., Güntner, A., Tomasella, J., Pfeffer, J., Ramillien, G., Emilio, T., Schietti, J., Seoane, L., da Silva Carvalho, J., Medeiros Moreira, D., Bonnet, M.-P., Seyler, F., (2019). The spatio-temporal variability of groundwater storage in the Amazon River Basin, *Advances in Water Resources*, 124:41-52. https://doi.org/10.1016/j.advwatres.2018.12.005.

gMonitor User's Manual (2012). gMonitor Gravity Data Acquisition and Processing Software, 37p.

Güntner, A., Stuck, J., Werth, S., Döll, P., Verzano, K., Merz, B. (2007). A global analysis of temporal and spatial variations in continental water storage, *Water Resources Research*, 43:W05416. doi:10.1029/2006WR005247.

Hodnett, M. G., Oyama, M. D., Tomasella, J., Marques, A. O. F. (1996). Comparisons of long-term soil water storage behaviour under pasture and forest in three areas of Amazonia. In Amazonian Deforestation and Climate, Gash, J. H. C., Nobre, C. A, Roberts, J. M., Victoria, R. L. (eds). Wiley: Chichester, UK; 57–77

Hinderer, J., Crossley, D., Warburton, R. (2007). Gravimetric Methods – Superconducting Gravity Meters, *Treatise on Geophysics*, 3:65–122. doi:10.1016/B978-044452748-6/00172-3

Hokkanen, T., Korhonen, K., Virtanen, H. (1994). Hydrogeological Effects on Superconducting Gravimeter Measurements at Metsähovi in Finland, *Journal of Environmental and Engineering Geophysics*, 11:261–267. doi:10.2113/jeeg11.4.261

INMET (2016), Panorama geral das condições meteorológicas e os principaís eventos extremos significativos ocorridos no Brasil em 2016, Instituto Nacional de Meteorologia, 1-11.

INMET (2017), Boletim Agroclimatológico Mensal, Instituto Nacional De Meteorologia, 52(12):1-45

Imanishi, Y., Kokubo, K., Tatehata, H. (2006). Effect of underground water on gravity observation at Matsushiro, Japan, *Journal of Geodynamics,* 41:221–226. doi:10.1016/j.jog.2005.08.031

Kang, K., Li, H., Peng, P., Hao, H., Wei, J. (2011). Seasonal variations in hydrological influences on gravity measurements using gPhones, *Terrestrial Atmospheric and Oceanic Science*, 22(2):157–168. doi:10.3319/TAO.2010.08.02.01(TibXS)

Kazama, T., Tamura, Y., Asari, K., Manabe, S., Okubo, S. (2012). Gravity changes associated with variations in local land-water distributions: Observations and hydrological modeling at Isawa Fan, northern Japan. *Earth, Planets and Space*, 64(4):309–331.

Koth, K. R., Long, A. J. (2012). Microgravity methods for characterization of groundwater-storage changes and aquifer properties in the karstic Madison aquifer in the Black Hills of South Dakota, 2009–12: U.S. Geological Survey Scientific Investigations Report 2012–5158, 22p.

Kroner, C., Jahr, T., Naujoks, M., Weise, A. (2007). Hydrological signals in gravity-foe or friend?, *International Association of Geodesy Symposia*, 130:504–510. doi:10.1007/978-3-540-49350-1_73

Lesack, L. F. W. (1993). Water balance and hydrologic characteristics of a rain forest catchment in the Central Amazon Basin, *Water Resources Research*, 29(3):759–773. doi:10.1029/92WR02371.

Llubes, M., Florsch, N., Hinderer, J., Longuevergne, L., Amalvict, M. (2004). Local hydrology, the Global Geodynamics Project and CHAMP/GRACE perspective: some case studies, *Journal of Geodynamics*, 38:355–374.

Lyard, F., Lefevre, F., Letellier, T., Francis, O. (2006). Modelling the global ocean tides: Modern insights from FES2004, *Ocean Dynamics*, 56:394–415. doi:10.1007/s10236-006-0086-x

Marengo, J. A. (2004). Interdecadal variability and trends of rainfall across the Amazon basin, *Theoretical and Applied Climatology*, 78:79–96.

Marengo, J. A., Nobre, C., Tomasella, J., Sampaio, G., Camargo, H. (2008). The drought of Amazonia in 2005, *Journal of Climate*, 21: 495–516.

Marengo, J. A., Tomasella, J., Alves, L. M., Soares, W. R., Rodriguez, D. A. (2011). The drought of 2010 in the context of historical droughts in the Amazon region, *Geophysical Research Letter*, 38:L12703

Mascarenhas Junior, T. A., Saraiva, J. M. B., Aguiar, F. E. O. (2009). Comparação entre a normal climatológica de 1961-1990 e o período 1991-2007 para a precipitação na cidade de Manaus-AM, *Revista Brasileira de Climatologia*, 5:165-175. doi:10.5380/abclima.v5i0.50484.

Meurers, B. (2006). Long and short term hydrological effects on gravity in Vienna, *Bulletin d'Information des Marées Terrestres*, 142:11343–11352.

Miguez-Macho, G. and Fan, Y. (2012a). The role of groundwater in the Amazon water cycle: 1. Influence on seasonal streamflow, flooding and wetlands, *Journal of Geophysical Research*, 117:1–30. doi:10.1029/2012JD017539

Miguez-Macho, G.and Fan, Y. (2012b). The role of groundwater in the Amazon water cycle: 2 . Influence on seasonal soil moisture and evapotranspiration, *Journal of Geophysical Research*, 117:1–27. doi:10.1029/2012JD017540

Neumeyer, J., Barthelmes, F., Kroner, C. Petrovic, S., Schmidt, R., Virtanen, H., Wilmes, H. (2008). Analysis of gravity field variations derived from Superconducting Gravimeter recordings, the GRACE satellite and hydrological models at selected European sites. *Earth Planet and Space,* 60**:**505–518. https://doi.org/10.1186/BF03352817

Pfeffer, J., Seyler, F., Bonnet, M.-P., Calmant, S., Frappart, F., Papa, F., Paiva, R. C. D., Satgé, F., Silva, J. S. D. (2014). Low-water maps of the groundwater table in the central Amazon by satellite altimetry, *Geophysical Research Letter*, 41:1981–1987. doi:10.1002/2013GL059134.

Pita, R. C. S., Silva Júnior, G. C., Rosário, F. F., Silva, M. L. (2018), Alter do Chão aquifer system west of Manaus city, Amazonas State, Brazil: hydrochemical processes, origin of salinity and relations with adjacent aquifers, *Revista do Instituto de Geociências – USP*, 18(1):27-96. doi: 10.11606/issn.2316-9095.v18-134253

Rodell, M., Houser, P. R., Jambor, U., Gottschalck, J., Mitchell, K., Meng, C.-J., Arsenault, K., Cosgrove, B., Radakovich, J., Bosilovich, M., Entin, J. K., Walker, J. P., Lohmann, D., Toll, D. (2004). The Global Land Data Assimilation System, *Bulletin American Meteorological Society*, 85:381–394. doi:10.1175/BAMS-85-3-381

Saibi, H. (2018). Microgravity and Its Applications in Geosciences, Gravity - Geoscience Applications, Industrial Technology and Quantum Aspect, Taher Zouaghi, IntechOpen, 41–72. doi: 10.5772/intechopen.71223. Available from: https://www.intechopen.com/books/gravity-geoscience-applications-industrial-technology-and-quantum-aspect/microgravity-and-its-applications-in-geosciences.

Spratt, R. (1982). Modelling the effect of atmospheric pressure variations on gravity, *Geophysical Journal of the Royal Astronomical Society*, 71:173–186.

Swenson, S., Wahr, J., Milly, P. C. D. (2003), Estimated accuracies of regional water storage variations inferred from the Gravity Recovery and Climate Experiment (GRACE), *Water Resources Research*, 39(8):1223. doi:10.1029/2002WR001808.

Tapley, B. D. (2004). GRACE Measurements of Mass Variability in the Earth System, *Science*, 305:503–505.

Tomasella, J., Hodnett, M. G., Cuartas, L. A., Nobre, A. D., Waterloo, M. J., Oliveira, S. M. (2008). The water balance of an Amazonian micro-catchment: the effect of interannual variability of rainfall on hydrological behaviour. *Hydrological Processes*, 22: 2133-2147. doi:10.1002/hyp.6813

Van Camp, M., Vauterin, P. (2005). Tsoft: Graphical and interactive software for the analysis of time series and Earth tides, *Computers and Geoscience*, 31:631–640. doi:10.1016/j.cageo.2004.11.015

Van Camp, M., Vanclooster, M., Crommen, O., Petermans, T., Verbeeck, K., Meurers, B., Van Dam, T., Dassargues, A. (2006). Hydrogeological investigations at the Membach station, Belgium, and application to correct long periodic gravity

variations, *Journal of Geophysical Research*, 111:B10403. doi:10.1029/2006JB004405.

Van Camp, M., de Viron, O., Watlet, A., Meurers, B., Francis, O., Caudron, C. (2017). Geophysics from terrestrial time-variable gravity measurements, *Reviews of Geophysics*, 55:938–992. doi:10.1002/2017RG000566

Volgyesi, L., Toth, G. (2005). Modelling gravity gradient variation due to water mass fluctuations, IAG International Symposium, *Gravity, Geoid and Space Missions*, 1-6. doi:10.1007/3-540-26932-0_63.

Zhou, J C. (2008). Loading problem in earth's tides and satellite gravity field recovery and its applications, Ph. D. thesis, Wuhan : Institute of Geodesy and Geophysics, Chinese Academy of Science, 39-43.

5. Conclusões Finais

No estudo regional (Capítulo 3) observou-se que o deslocamento vertical associado à carga hidrológica é influenciado pela geologia, na qual a maior amplitude de deslocamento vertical ocorre em direção às bacias sedimentares e às planícies. Assim, condições geológicas adequadas para armazenar água nos sedimentos, associado à propriedades físicas, além da espessura das camadas sedimentares na Bacia Amazônica são essenciais para explicar as variações no deslocamento vertical. Nas bacias sedimentares, existem estações onde o deslocamento vertical é menor do que o esperado, e isto pode estar associado ao adelgaçamento e/ou compactação da camada de rocha sedimentar e/ou presença de rochas ígneas intrusivas.

Os resultados regionais da modelagem de deformação hidrológica baseada no TWS representaram 18 a 66% da amplitude da variação do deslocamento vertical. Na região da variação máxima da amplitude do TWS, onde se localiza a porção oriental do aquífero Alter do Chão, a diferença entre os resultados do modelo de deformação hidrológica e o deslocamento vertical local foram mais evidentes. Aqui, os resultados do modelo de deformação hidrológica representaram apenas 18-32% da amplitude, porque os principais rios da Bacia Amazônica estão nesta região. Como resultado, a contribuição desta modelagem é subestimada devido à limitada resolução espacial do TWS, obtido a partir da missão GRACE.

Por outro lado, os resultados de um modelo de deformação hidrológica de alta resolução baseado no modelo LSDM resultaram em 36% a 116% da amplitude da variação do deslocamento vertical. As variações máximas de amplitude foram identificadas nas estações próximas ao rio Amazonas e próximas ao encontro entre os principais afluentes, reforçando a importante contribuição da carga hidrológica dos rios. Além disso, a variação de amplitude do deslocamento vertical aumenta da Cordilheira dos Andes até a Bacia sedimentar do Amazonas. As estações na borda leste da Bacia do Amazonas, delimitadas pelo Arco Gurupá, apresentaram valores mais baixos na variação de amplitude máxima do que as estações em encontros fluviais na bacia sedimentar do Amazonas. Isso pode estar associado à distribuição da água nos canais do estuário e do delta antes de fluir para o oceano.

No estudo local (Capítulo 4), observou-se que em geral, quando começam as primeiras chuvas, o sinal gravitacional, fluvial e de umidade do solo está em valores mínimos. A umidade do solo é instantaneamente influenciada pelo início da estação

chuvosa, com a primeira precipitação. Após as primeiras chuvas, o aumento da gravidade coincide com o aumento da umidade do solo. O solo fica saturado e seu sinal atinge valores máximos, que se sustentam até o final do período chuvoso. Devido à relação instantânea da umidade do solo com a precipitação, ambos apresentaram semelhantes valores de atraso em relação à variação de gravidade, quase 3 meses (2016) e 5 meses (2017). Então, estimou-se o período de recarga do aquífero de 2 e 5 meses para 2016 e 2017, respectivamente. O maior intervalo de recarga em 2017 mostrou o sistema hidrológico tentando recuperar a água perdida nos anos de seca anteriores, devido ao déficit no armazenamento de água nas águas superficiais, como rios, e no solo.

Após a saturação do solo por infiltração, o lençol freático passa a ser alimentado por percolação e começa a aumentar. Assim, a gravidade está refletindo, principalmente, as águas subterrâneas. Depois, o solo perde umidade (os valores da umidade do solo diminuem), enquanto os valores da gravidade são sustentados, refletindo o comportamento sustentado das águas subterrâneas.

Considerando que o sinal de gravidade é influenciado pela zona não saturada e pela água subterrânea, o sinal representa o resultado desses processos combinados, e o atraso do resultado da estimativa da água subterrânea sem a correção da zona não saturada é apenas uma aproximação. Nessa estimativa, o máximo na variação da gravidade, refletindo principalmente as águas subterrâneas, precedeu o máximo na variação fluvial e foi mais curto durante os anos de seca (alguns dias) do que nos anos de cheia (~ duas semanas). Por outro lado, a estimativa da água subterrânea com a correção da zona não saturada atingiu o máximo e o mínimo em aproximadamente no mesmo período da variação fluvial. Assim, se a modelagem mostrou que o rio não está influenciando o sinal de gravidade, e o sinal de gravidade está representando principalmente as águas subterrâneas, o comportamento semelhante entre essas variáveis mostrou a conexão entre as variações das águas subterrâneas e as águas superficiais, como os rios.

6. Referência Bibliográfica

Agnew, D. C., (2007). Earth Tides. Treatise Geophys., 3, 163–195. https://doi.org/10.1016/B978-044452748-6.00056-0

Aguiar, C. J. B. (2012). Relatório diagnóstico Aquífero Alter do Chão no Estado do Amazonas, Bacia Sedimentar do Amazonas. In: C. J. B. Aguiar, M. A. A. Mourão (Eds.), Projeto Rede Integrada de Monitoramento das Águas Subterrâneas. Belo Horizonte: CPRM – Serviço Geológico do Brasil. (Coleção de Relatórios-Diagnóstico dos Aquíferos Sedimentares do Brasil), 30p.

Almeida, F. F. M. (1978). A evolução dos crátons Amazônico e do São Francisco comparada com seus homólogos do hemisfério norte. Anais do 30º Congresso Brasileiro de Geologia, Sociedade Brasileira de Geologia, 6, 2393–2407.

Almeida, F. G. V., Calmant, S., Seyler, F., Ramillien, G., Blitzkow, D., Matos, A. C. C., & Silva, J. S. (2012). Time-variations of equivalente water heights from Grace Mission and in-situ river stages in the Amazon basin. Acta Amazonica, 42, 125–134.

Alterman, Z., Jarosch, H., Pekeris, C.L. (1959). Oscillations of the Earth. Proc. R. Soc. A Math. Phys. Eng. Sci., 252, 80–95. https://doi.org/10.1098/rspa.1959.0138

ANA, Agência Nacional das Águas, & J. L. G. Zoby. (2005). Panorama da qualidade das águas subterrâneas no Brasil. (p. 80). Brasília: Agência Nacional das Águas.

ANA, & Agência Nacional das Águas. (2015). Avaliação dos Aquíferos das Bacias Sedimentares da Província Hidrogeológica Amazonas no Brasil (escala 1:1.000.000) e Cidades Pilotos (escala 1:50.000), Geologia da Província Hidrogeológica Amazonas (Vol II, p. 126). SIP: Brasília, Agência Nacional de Águas (ANA).

ANA, & Agência Nacional das Águas. (2016). http://www.metadados.inde.gov.br/geonetwork/srv/br/metadata.show.embedded?uuid=3ec60e4f-85ea-4ba7-a90c-734b57594f90

ANA, & Agência Nacional das Águas. (2017). www2.ana.gov.br/Paginas/portais/bacias/amazonica.aspx

Argus, D. F., Landerer, F. W., Wiese, D. N., Martens, H. R., Fu, Y., Famiglietti, J. S., & Watkins, M. M. (2017). Sustained water loss in California's mountain ranges during severe drought from 2012 to 2015 inferred from GPS. Journal of Geophysical Research: Solid Earth, 122, 10559–10585. https://doi.org/10.1002/2017JB014424

Baker, T. F. (1996). A new test of Earth tide models in central Europe. Geophysical Research Letters, 23(24), 3559-3562.

Baker, T. F., Bos, M. S. (2003). Validating Earth and ocean tide models using tidal gravity measurements. Geophys. J. Int., 152, 468–485.

Batjes, N. H. (2005). SOTER-based soil parameter estimates for Latin America and the Caribbean (ver. 1.0). Report 2005/02 ISRIC-World Soil Information, Wageningen. http://data.isric.org/geonetwork/srv/eng/catalog.search#/metadata/3a9ed87d-affc-4f72-aa6e-72db4fefec40

Beutler G., Weber R., Hugentobler U., Rothacher M., Verdun A. (1998). GPS Satellite Orbits. In: Teunissen P.J.G., Kleusberg A. (eds) GPS for Geodesy. Springer, Berlin, Heidelberg, 650p.

Bevis, M., Alsdorf, D., Kendrick, E., Fortes, L. P., Forsberg, B., Smalley, R., & Becker, J. (2005). Seasonal fluctuations in the mass of the Amazon River system and Earth's elastic response. Geophysical Research Letters, 32, 1–4. https://doi.org/10.1029/2005GL023491

Blakely, R. (1995). Potential Theory in Gravity and Magnetic Applications. Cambridge University Press, Cambridge. doi:10.1017/CBO9780511549816

Blewitt, G., Hammond, W., & Kreemer, C. (2018). Harnessing the GPS Data Explosion for Interdisciplinary Science. Eos, 99, https://doi.org/10.1029/2018eo104623

Blewitt, G., Lavallée, D., Clarke, P., & Nurutdinov, K. (2001). A new global mode of Earth deformation: Seasonal cycle detected. Science, 294(5550), 2342–2345. https://doi.org/10.1126/science.1065328

Bower, D. R., Courtier, N. (1998). Precipitation effects on gravity measurements at the Canadian Absolute Gravity Site. Phys. Earth Planet. Inter., 106, 353–369. https://doi.org/10.1016/S0031-9201(97)00101-5

Brooks, K.N., Ffolliott, P.F., Magner, J.A. (2012). Hydrology and the Management of Watersheds, Wiley, 533 p.

Brush, S. G. (1996). Nebulous Earth: the Origin of the Solar System and the Core of the Earth from Laplace to Jeffreys. Cambridge University Press, Cambridge.

Brutsaert, W. (2005). Hydrology: An Introduction, Cambridge University Press, 605p.

California Institute of Technology (2010). Introduction to GPS Applications in Geodesy, GIPSY User Group Class, Jet Propulsion Laboratory, California Institute of Technology, 38p.

Caputo, M. (1962). Tables for the deformation of an Earth model by surface mass distributions. J. Geophys. Res., 67, 1611–1616. https://doi.org/10.1029/JZ067i004p01611

Caputo, M. (1961). Deformation of a Layered Eath by an Axially Symmetric Surface Mass Distribution. J. Geophys. Res., 66, 1479–1483.

Caputo, M. V. (2014). Juruá orogeny: Brazil and Andean countries. Brazilian Journal of Geology, 44, 181–190. https://doi.org/10.5327/Z2317-4889201400020001

Caputo, M. V., & Silva, O. B. (1991). Origem e evolução de bacias sedimentares (p. 415). Rio de Janeiro: Petrobrás.

Caputo, M. V., & Soares, E. A. A. (2016). Eustatic and tectonic change effects in the reversion of the transcontinental Amazon River drainage system. Brazilian Journal of Geology, 46, 301–328.

Carmichael, R. S., Henry Jr, G. (1977). Gravity exploration for groundwater and bedrock topography in glaciated areas. Geophysics, 42(4):850–859.

Cerovský, I., Meurers, B., Pohánka, V., Frisch, W., Goga, B. (2004). Gravity and magnetic 3D modeling software - Mod3D, in Meurers, B. and Pail, R. (eds): Proc. 1st Workshop on Int. Gravity Field Research, Österr. Beitr. Met. Geoph., 163-168, in press.

Chanard, K., Avouac, J. P., Ramillien, G., & Genrich, J. (2014). Modeling deformation induced by seasonal variations of continental water in the Himalaya region: Sensitivity to Earth elastic structure. Journal of Geophysical Research: Solid Earth, 119, 5097–5113. https://doi.org/10.1002/2013JB010451

Cleary, R. W. (2017). Águas subterrâneas, Princeton Groundwater Inc., 117p

Cordani, U. G., Ramos, V. A., Fraga, L. M., Cegarra, M., Delgado, I., Souza, K. G., et al. (2016). Tectonic Map of South America, Comission of the Geologic Map of the World - Scale 1:5,000,000 (2nd ed.). Paris: CGMW-CPRM-SEGEMAR.

Costa, S. M. A., Matos, A. C. O. C., & Blitzkow, D. (2012). Validation of the land water storage from Gravity Recovery and Climate Experiment (GRACE) with gauge data in the Amazon Basin. Boletim Ciências Geodésicas, Curitiba, 18, 262–281. https://doi.org/10.1590/S1982-21702012000200006

Crossley, D.J., Jensen, O.G., Hinderer, J. (1995). Effective barometric admittance and gravity residuals. Physics on the Earth Planetary Interiors, 90:221–241. doi:10.1016/0031-9201(95)05086-Q

D'avila Junior, J. C. M., Vieira, A. F. S G. (2019). Padrões pluviométricos da Cidade de Manaus-AM: 1986 a 2015. Boletim Paulista de Geografia, 102:1-31.

Davis, J. L., Elósegui, P., Mitrovica, J. X., & Tamisiea, M. E. (2004). Climate-driven deformation of the solid Earth from GRACE and GPS. Geophysical Research Letters, 31, 1–4. https://doi.org/10.1029/2004GL021435

Dehant, V., Defraigne, P., Wahr, J. M. (1999). Tides for a convective Earth. Journal of Geophysical Research, 104(B1):1035–1058.

Dijkshoorn, J. A., Huting, J. R. M., & Tempel, P. (2005). Update of the 1:5 million soil and terrain database for Latin America and the Caribbean (SOTERLAC, ver. 2.0). Report 2005/01, ISRIC - World Soil Information, Wageningen. http://data.isric.org/geonetwork/srv/eng/catalog.search#/metadata/436bd4b0-7ffc-4272-be57-686b7d7eea7d

Dill, R. (2008). Hydrological model LSDM for operational Earth rotation and gravity field variations. In: Scientific Technical Report STR (Vol. 08/09, p. 35). Germany: GFZ Potsdam. https://doi.org/10.2312/GFZ.b103-08095

Dill, R., & Dobslaw, H. (2013). Numerical simulations of global-scale high-resolution hydrological crustal deformations. Journal of Geophysical Research: Solid Earth, 118, 5008–5017. https://doi.org/10.1002/jgrb.50353

Dill, R., Klemann, V., & Dobslaw, H. (2018). Relocation of river storage from global hydrological models to georeferenced river channels for improved load-induced surface displacements. Journal of Geophysical Research: Solid Earth, 123, 7151–

7164. https://doi.org/10.1029/2018JB016141

Dong, D., Fang, P., Bock, Y., Cheng, M. K., & Miyazaki, S. (2002). Anatomy of apparent seasonal variations from GPS-derived site position time series. Journal of Geophysical Research, 107(B4), 1–16. https://doi.org/10.1029/2001JB000573

Dziewonski, A., & Anderson, D. (1981). Preliminary reference Earth model. Physics of the Earth and Planetary Interiors, 25, 297–356. https://doi.org/10.1016/0031-9201(81)90046-7

El-Rabbany, A. (2002). Introduction to GPS: The Global Positioning System, Artech House, 176p.

Espinoza Villar, J. C., Guyot, J. L., Ronchail, J., Cochonneau, G., Filizola, N., Fraizy, P., et al. (2009a). Contrasting regional discharge evolutions in the Amazon basin (1974–2004). Journal of Hydrology, 375, 297–311. https://doi.org/10.1016/j.jhydrol.2009.03.004

Espinoza Villar, J. C., Ronchail, J., Guyot, J.-L., Cochonneau, G. G., Naziano, F., Lavado, W., et al. (2009b). Spatio-temporal rainfall variability in the Amazon basin countries (Brazil, Peru, Bolivia, Colombia, and Ecuador). International Journal of Climatology, 29, 1574–1594. https://doi.org/10.1002/joc.1791

Espinoza, J. C., Chavez, S., Ronchail, J., Junquas, C., Takahashi, K., & Lavado, W. (2015). Rainfall hotspots over the southern tropical Andes: Spatial distribution, rainfall intensity, and relations with large-scale atmospheric circulation. Water Resources Research, 51, 3459–3475. https://doi.org/10.1002/2014WR016273

Espurt, N., Baby, P., Brusset, S., Roddaz, M., Hermoza, W., & Barbarand, J. (2010). The Nazca Ridge and Uplift of the Fitzcarrald Arch: Implications for Regional Geology in Northern South America. In C. Hoorn & F. P. Wesselingh (Eds.), Amazonia: Landscape and Species Evolution, (pp. 89–100). Blackwell. https://doi.org/10.1002/9781444306408.ch6

Faria, M. S. G., Bahia, R., Almeida, M. E., Oliveira, M. A. (2004). Folha SA.20-Manaus. In: Schobbenhaus, C., Gonçalves, J. H., Santos, J. O. S., Abram, M. B., Leão Neto, R., Matos, G. M. M., Vidotti, R. M., Ramos, M. A. B., Jesus, J. D. A. de., (eds.), Carta Geológica do Brasil ao Milionésimo, Sistemas de Informações Geográficas-SIG. Programa Geologia do Brasil, CPRM, Brasília. CD-ROM.

Farrell, W. E. (1972). Deformation of the Earth's surface loads. Reviews of Geophysics, 10, 761–767. https://doi.org/10.1029/RG010i003p00761

Fisch, G. (1990). Climatic aspects of the Amazonian Tropical Forest. Acta Amazonica, 20:39-48. doi:10.1590/1809-43921990201048

Fisch, G., Marengo, J. A., & Nobre, C. A. (1998). Uma revisão geral sobre o clima da Amazônia. Acta Amazonica, 28(2), 101–126. https://doi.org/10.1590/1809-43921998282126

Fitts, C. R. (2015). Águas Subterrânea (Groundwater Science). Translated by Daniel Vieira (2 ed., p. 692). Rio de Janeiro: Elsevier. ISBN 978-85-352-7744-9.

Frappart, F., Papa, F., Santos da Silva, J., Ramillien, G., Prigent, C., Seyler, F., Calmant, S. (2012). Surface freshwater storage in the Amazon basin during the 2005 exceptional drought. Environmental Research Letter, 7 (4):044010.

Frappart, F., Papa, F., Güntner, A., Tomasella, J., Pfeffer, J., Ramillien, G., et al. (2019). The spatio-temporal variability of groundwater storage in the Amazon River Basin. Advances in Water Resources, 124, 41–52. https://doi.org/10.1016/j.advwatres.2018.12.005

Freeze, A. R. and Cherry, J. A. (2017). Águas Subterrâneas, tradução de Groundwater, Everton de Oliveira (coord.), São Paulo, 698p.

Fritsche, M., Döll, P., & Dietrich, R. (2012). Global-scale validation of model-based load deformation of the Earth's crust from continental watermass and atmospheric pressure variations using GPS. Journal of Geodynamics, 59–60, 133–142. https://doi.org/10.1016/j.jog.2011.04.001

Fu, Y., Argus, D. F., Freymueller, J. T., & Heflin, M. B. (2013). Horizontal motion in elastic response to seasonal loading of rain water in the Amazon Basin and monsoon water in Southeast Asia observed by GPS and inferred from GRACE. Geophysical Research Letters, 40, 6048–6053. https://doi.org/10.1002/2013GL058093

Gemael, C. (1999). Introdução à Geodésia Física, Ed. UFPR, Curitiba, 304p.

gMonitor User's Manual (2012). gMonitor Gravity Data Acquisition and Processing Software, 37p.

Guimarães, G. N., Blitzkow, D. (2011). Problema de valor de contorno da geodésia: Uma abordagem conceitual. Boletim de Ciências Geodésicas, sec. Comunicações/Trab. Técnicos, Curitiba, 17(4), 607–624

Guimarães, G. N., Blitzkow, D., de Matos, A. C. O. C., Almeida, F. G. V., & Barbosa, A. C. B. (2012). Analysis of the crust displacement in Amazon Basin. In S. Kenyon, M. Pacino, & U. Marti (Eds.), Geodesy for planet Earth, international association of geodesy symposia (Vol. 136, pp. 885–891). Berlin: Springer.

Güntner, A., Stuck, J., Werth, S., Döll, P., Verzano, K., Merz, B. (2007). A global analysis of temporal and spatial variations in continental water storage. Water Resources Research, 43:W05416. doi:10.1029/2006WR005247.

Guo, J., Li, Y., Huang, Y., Deng, H., Xu, S., & Ning, J. (2004). Green's function of the deformation of the Earth as a result of atmospheric loading. Geophysical Journal International, 159, 53–68. https://doi.org/10.1111/j.1365-246X.2004.02410.x

Hagemann, S., & Dümenil, L. (1998). Documentation for the hydrological discharge model. In: Technical Report No. 17. Hamburg, Germany: Max Planck Institute for Meteorology.

Heki, K. (2001). Seasonal modulation of interseismic strain buildup in northeastern Japan driven by snow loads. Science, 293, 89–92. https://doi.org/10.1126/science.1061056

Hinderer, J., Crossley, D., Warburton, R. (2007). Gravimetric Methods – Superconducting Gravity Meters. Treatise on Geophysics, 3:65–122. doi:10.1016/B978-044452748-

6/00172-3

Hodnett, M. G., Oyama, M. D., Tomasella, J., Marques, A. O. F. (1996). Comparisons of long-term soil water storage behaviour under pasture and forest in three areas of Amazonia. In Amazonian Deforestation and Climate, Gash, J. H. C., Nobre, C. A, Roberts, J. M., Victoria, R. L. (eds). Wiley: Chichester, UK; 57–77

Hokkanen, T., Korhonen, K., Virtanen, H. (1994). Hydrogeological Effects on Superconducting Gravimeter Measurements at Metsähovi in Finland. Journal of Environmental and Engineering Geophysics, 11:261–267. doi:10.2113/jeeg11.4.261

Ibanez, D. M., Riccomini, C., & Miranda, F. P. (2014). Is the current stress state in the Central Amazonia caused by surface water loading?.Journal of South American Earth Sciences, 55, 19–28. https://doi.org/10.1016/j.jsames.2014.07.002

INMET, & Instituto Nacional de Meteorologia. (1992). Normais climatológicas (1961-1990). Brasília, Brasil: Departamento Nacional de Meteorologia.

INMET (2016), Panorama geral das condições meteorológicas e os principaís eventos extremos significativos ocorridos no Brasil em 2016, Instituto Nacional de Meteorologia, 1-11.

INMET (2017), Boletim Agroclimatológico Mensal, Instituto Nacional De Meteorologia, 52(12):1-45

Imanishi, Y., Sato, T., Higashi, T., Sun, W., Okubo, S. (2004). A Network of Superconducting Gravimeters Detects Submicrogal Coseismic Gravity Changes. Science, 306, 476–478. https://doi.org/10.1126/science.1101875

Imanishi, Y., Kokubo, K., Tatehata, H. (2006). Effect of underground water on gravity observation at Matsushiro, Japan. Journal of Geodynamics, 41:221–226. doi:10.1016/j.jog.2005.08.031

Kang, K., Li, H., Peng, P., Hao, H., Wei, J. (2011). Seasonal variations in hydrological influences on gravity measurements using gPhones. Terrestrial Atmospheric and Oceanic Science, 22(2):157–168. doi:10.3319/TAO.2010.08.02.01(TibXS)

Karegar, M. A., Dixon, T. H., Kusche, J., & Chambers, D. P. (2018). A new hybrid method for estimating hydrologically induced vertical deformation from GRACE and a hydrological model: An example from Central North America. Journal of Advances in Modeling Earth Systems, 10, 1196–1217. https://doi.org/10.1029/2017MS001181

Kazama, T., Tamura, Y., Asari, K., Manabe, S., Okubo, S. (2012). Gravity changes associated with variations in local land-water distributions: Observations and hydrological modeling at Isawa Fan, northern Japan. Earth, Planets and Space, 64(4):309–331.

Koth, K. R., Long, A. J. (2012). Microgravity methods for characterization of groundwater-storage changes and aquifer properties in the karstic Madison aquifer in the Black Hills of South Dakota, 2009–12: U.S. Geological Survey Scientific Investigations Report 2012–5158, 22p.

Kroner, C., Jahr, T., Naujoks, M., Weise, A. (2007). Hydrological signals in gravity- foe or

friend?. International Association of Geodesy Symposia, 130:504–510. doi:10.1007/978-3-540-49350-1_73

Kusche, J., & Schrama, E. J. O. (2005). Surface mass redistribution inversion from global GPS deformation and Gravity Recovery and Climate Experiment (GRACE) gravity data. Journal of Geophysical Research, 110, B09409. https://doi.org/10.1029/2004JB003556

Kvas, A., Behzadpour, S., Ellmer, M., Klinger, B., Strasser, S., Zehentner, N., & Mayer-Gürr, T. (2019). ITSG-Grace2018: Overview and evaluation of a new GRACE-only gravity field time series. Journal of Geophysical Research: Solid Earth, 124, 9332–9344. https://doi.org/10.1029/2019JB017415

Lambert, A., Beaumont, C. (1977). Nano variations in gravity due to seasonal groundwater movements: Implications for the gravitational detection of tectonic movements. J. Geophys. Res., 82, 297–306. https://doi.org/10.1029/JB082i002p00297

Langley R.B. (1998). GPS receivers and the observables. In: Teunissen P.J.G., Kleusberg A. (eds) GPS for Geodesy. Springer, Berlin, Heidelberg, 650p.

Laske, G., Masters, G., Ma, Z., & Pasyanos, M. (2013). Update on CRUST1.0—A 1-degree Global Model of Earth's Crust. Geophysical Research Abstracts, 15, EGU2013-2658.

Latrubesse, E. M., Arima, E. Y., Dunne, T., Park, E., Baker, V. R., d'Horta, F. M., et al. (2017). Damming the rivers of the Amazon basin. Nature, 546, 363–369. https://doi.org/10.1038/nature22333

Latrubesse, E. M., Stevaux, J. C., & Sinha, R. (2005). Tropical rivers. Geomorphology, 70, 187–206. https://doi.org/10.1016/j.geomorph.2005.02.005

LDAS, & Land Data Assimilation System. (2018). Retrieved from: https://ldas.gsfc.nasa.gov/gldas/GLDASelev.php

Lesack, L. F. W. (1993). Water balance and hydrologic characteristics of a rain forest catchment in the Central Amazon Basin. Water Resources Research, 29(3):759–773. doi:10.1029/92WR02371.

Llubes, M., Florsch, N., Hinderer, J., Longuevergne, L., Amalvict, M. (2004). Local hydrology, the Global Geodynamics Project and CHAMP/GRACE perspective: some case studies. Journal of Geodynamics, 38:355–374.

Longman, I. M. (1963). A Green's Function for Determining the Deformation of the Earth under Surface Mass Loads:2. Computations and Numerical Results. J. Geophys. Res., 68, 485.

Longman, I.M. (1962). A Green's function for determining the deformation of the Earth under surface mass loads: 1.Theory. J. Geophys. Res., 67, 845–850.

Love, A. E. H. (1926). A Treatise on the Mathematical Theory of Elasticity, Dover, Mineola, N.Y., 4th ed., 643p.

Lyard, F., Lefevre, F., Letellier, T., Francis, O. (2006). Modelling the global ocean tides:

Modern insights from FES2004. Ocean Dynamics, 56:394–415. doi:10.1007/s10236-006-0086-x

Mangiarotti, S., Cazenave, A., Soudarin, L., & Crétaux, J. F. (2001). Annual vertical crustal motions predicted from surface mass redistribution and observed by space geodesy. Journal of Geophysical Research, 106, 4277–4291. https://doi.org/10.1029/2000JB900347

Manoel Filho, J. (2008). Ocorrência das Águas Subterrâneas, Capítulo 2.1, 53-75 In: Feitosa, F. A. C. (Coord.), Manoel Filho, J., Feitosa, E. C., Demetrio, J. G. A., 2008. Hidrogeologia: conceitos e aplicações, CPRM – Serviço Geológico do Brasil, 3rd ed., 812p

Marengo, J. A. (2004). Interdecadal variability and trends of rainfall across the Amazon basin. Theoretical and Applied Climatology, 78:79–96.

Marengo, J. A. (2005). The characteristics and variability of the atmospheric water balance in the Amazon basin: spatial and temporal variability. Climate Dynamics, 24, 11–22. https://doi.org/10.1007/s00382-004-0461-6

Marengo, J. A., Nobre, C., Tomasella, J., Sampaio, G., Camargo, H. (2008). The drought of Amazonia in 2005. Journal of Climate, 21: 495–516.

Marengo, J. A., Tomasella, J., Alves, L. M., Soares, W. R., Rodriguez, D. A. (2011). The drought of 2010 in the context of historical droughts in the Amazon region. Geophysical Research Letter, 38:L12703

Mascarenhas Junior, T. A., Saraiva, J. M. B., Aguiar, F. E. O. (2009). Comparação entre a normal climatológica de 1961-1990 e o período 1991-2007 para a precipitação na cidade de Manaus-AM, Revista Brasileira de Climatologia, 5:165-175. doi:10.5380/abclima.v5i0.50484.

Mayer-Gürr, T., Behzadpur, S., Ellmer, M., Kvas, A., Klinger, B., Strasser, S., & Zehentner, N. (2018). ITSG-Grace2018-monthly, daily and static gravity field solutions from GRACE. GFZ Data Services. http://doi.org/10.5880/ICGEM.2018.003

Meurers, B. (2006). Long and short term hydrological effects on gravity in Vienna. Bulletin d'Information des Marées Terrestres, 142:11343–11352.

Miguez-Macho, G., & Fan, Y. (2012a). The role of groundwater in the Amazon water cycle: 1. Influence on seasonal streamflow, flooding and wetlands. Journal of Geophysical Research, 117, 1–30. https://doi.org/10.1029/2012JD017539

Miguez-Macho, G., & Fan, Y. (2012b). The role of groundwater in the Amazon water cycle: 2 . Influence on seasonal soil moisture and evapotranspiration. Journal of Geophysical Research, 117, 1–27. https://doi.org/10.1029/2012JD017540

Milani, E. J., & Thomaz Filho, A. (2000). Sedimentary basins of the South America. In U. G. Cordani, E. J. Milani, A. Thomaz-Filho, & D. A. Campos (Eds.), Tectonic evolution of South America. 31st International Geological Congress. Rio de Janeiro (pp. 389–449). Academia Brasileira de Ciências e Departamento Nacional da Produção Mineral (DNPM) 856p.

Ministério do Meio Ambiente (2007). Águas subterrâneas: um recurso a ser conhecido e protegido, Ministério do Meio Ambiente, Brasília, 37p.

Monico, J. F. G. (2008). Posicionamento pelo NAVSTAR-GPS: descrição, fundamentos e aplicações, Ed. UNESP, São Paulo, 2ª ed., 480p

Moreira, D. M., Calmant, S., Perosanz, F., Xavier, L., Rotunno Filho, O. C., Seyler, F., & Monteiro, A. C. (2016). Comparisons of observed and modeled elastic responses to hydrological loading in the Amazon basin. Geophysical Research Letters, 43, 9604–9610. https://doi.org/10.1002/2016GL070265

Mortatti, J., Moraes, J. M., Victoria, R. L., & Martinelli, L. A. (1997). Hydrograph separation of the Amazon River: A methodological study. Aquatic Geochemistry, 3, 117–128. https://doi.org/10.1023/A:1009606801595

Munis, M. B. (2009). Caracterização geomagnética do gráben Purus e suas implicações na evolução das bacias do Solimões e do Amazonas. Tese de Doutorado, Sistemas Petrolíferos, PEC, COPPE (p. 102). Universidade Federal do Rio de Janeiro.

Nesbitt, S. W., & Anders, A. M. (2009). Very high resolution precipitation climatologies from the Tropical Rainfall Measuring Mission precipitation radar. Geophysical Research Letters, 36, 1–5. https://doi.org/10.1029/2009GL038026

Neumeyer, J., Barthelmes, F., Kroner, C. Petrovic, S., Schmidt, R., Virtanen, H., Wilmes, H. (2008). Analysis of gravity field variations derived from Superconducting Gravimeter recordings, the GRACE satellite and hydrological models at selected European sites. Earth Planet and Space, 60:505–518. https://doi.org/10.1186/BF03352817

Nobre, C. A., Obregón, G. O., Marengo, J. A., Fu, R., & Poveda, G. (2009). Characteristics of Amazonian climate: Main features. Geophysical Monograph Series, 186, 149–162. https://doi.org/10.1029/2009GM000903

Penna, N., Bos, M., Baker, T., Scherneck, H. G. (2008). Assessing the accuracy of predicted ocean tide loading displacement values. J. Geod., 82(12), 893–907, doi:10.1007/s00190-008-0220-2

Pfeffer, J., Seyler, F., Bonnet, M.-P., Calmant, S., Frappart, F., Papa, F., Paiva, R. C. D., Satgé, F., Silva, J. S. D. (2014). Low-water maps of the groundwater table in the central Amazon by satellite altimetry. Geophysical Research Letter, 41:1981–1987. doi:10.1002/2013GL059134.

Pita, R. C. S., Silva Júnior, G. C., Rosário, F. F., Silva, M. L. (2018), Alter do Chão aquifer system west of Manaus city, Amazonas State, Brazil: hydrochemical processes, origin of salinity and relations with adjacent aquifers. Revista do Instituto de Geociências – USP, 18(1):27-96. doi: 10.11606/issn.2316-9095.v18-134253

Pokhrel, Y. N., Fan, Y., Miguez-Macho, G., Yeh, P. J. F., & Han, S. C. (2013). The role of groundwater in the Amazon water cycle: 3. Influence on terrestrial water storage computations and comparison with GRACE. Journal of Geophysical Research: Atmospheres, 118, 3233–3244. https://doi.org/10.1002/jgrd.50335

Rabbel, W., Schuh, H. (1986). The Influence of Atmospheric Loading on VLBI-Experiments. J. Geophys., 59, 164–170.

Rajner, M., & Liwosz, T. (2011). Studies of crustal deformation due to hydrological loading on GPS height estimates. Geodesy and Cartography, 60, 135–144. https://doi.org/10.2478/v10277-012-0012-y

Rajner, M., & Liwosz, T. (2017). Analysis of seasonal position variation for selected GNSS sites in Poland using loading modelling and GRACE data. Geodesy and Geodynamics, 8, 253–259. https://doi.org/10.1016/j.geog.2017.04.001

Reynolds, C. A., Jackson, T. J., & Rawls, W. J. (2000). Estimating soil water-holding capacities by linking the Food and Agriculture Organization soil map of the world with global pedon databases and continuous pedo-transfer functions. Water Resources Research, 36, 3653–3662. https://doi.org/10.1029/2000WR900130

Rocha, H. R., Manzi, A. O., Shuttleworth, J. (2009), Evapotranspiration. Geophysical Monograph Series, 186:261-272.

Rodell, M., Houser, P. R., Jambor, U., Gottschalck, J., Mitchell, K., Meng, C.-J., et al. (2004). The global land data assimilation system. American Meteorolical Society, 85, 381–394. https://doi.org/10.1175/BAMS-85-3-381

Saibi, H. (2018). Microgravity and Its Applications in Geosciences, Gravity - Geoscience Applications, Industrial Technology and Quantum Aspect, Taher Zouaghi, IntechOpen, 41–72. doi: 10.5772/intechopen.71223.

Santos, E. B., Lucio, P. S., & Silva, C. M. S. E. (2015). Precipitation regionalization of the Brazilian Amazon. Atmospheric Science Letters, 16, 185–192. https://doi.org/10.1002/asl2.535

Schenk, C. J., Viger, R. J., & Anderson, C. P. (1999). Maps showing geology, oil and gas fields and geologic provinces of the South America region. In: U. S. Geological Survey. https://pubs.usgs.gov/of/1997/ofr-97-470/OF97-470D/sam06Gmap.html#TOP

Schobbenhaus, C., & Bellizia, A. (2001). Geological map of South America, 1:5000000. Brasilia: CGMW-CPRM-DNPM-UNESCO.

Schwiderski, E. W. (1980). On Charting Global Ocean Tides. Rev. Geophys. Sp. Phys., 18, 243–268.

Seyler, P. T., & Boaventura, G. R. (2003). Distribution and partition of trace metals in the Amazon basin. Hydrological Processes, 17, 1345–1361. https://doi.org/10.1002/hyp.1288

Shiklomanov, I. (1998). World water resources: a new appraisal and assessment for the 21st century, UNESCO, Paris, 37p.

Slichter, L. B., Caputo, M. (1960). Deformation of an Earth Model by Surface Pressures, J. Geophys. Res., 65, 4151–4156.

Smith, W. H. F., & Sandwell, D. T. (1997). Global seafloor topography from satellite

altimetry and ship depth soundings. Science, 277(5334), 1956–1962. https://doi.org/10.1126/science.277.5334.1956

Spratt, R. (1982). Modelling the effect of atmospheric pressure variations on gravity. Geophysical Journal of the Royal Astronomical Society, 71:173–186.

Stolz, A. and Larden, D.R. (1979). Seasonal displacement and deformation of the Earth by the atmosphere. J. Geophys. Res. Solid Earth, 84, 6185–6194. https://doi.org/10.1029/JB084iB11p06185

Stoneley, R. (1926). The elastic yielding of the earth. Geophys. Suppl. to Mon. Not. R. Astron. Soc., 1, 356–359.

Swenson, S., Wahr, J., Milly, P. C. D. (2003), Estimated accuracies of regional water storage variations inferred from the Gravity Recovery and Climate Experiment (GRACE). Water Resources Research, 39(8):1223. doi:10.1029/2002WR001808.

Takeuchi, H. (1950). On the Earth tide of the compressible Earth of variable density and elasticity. Trans. Am. Geophys. Union, 31, 651–689. https://doi.org/10.1029/TR031i005p00651

Tapley, B. D. (2004). GRACE measurements of mass variability in the Earth system. Science, 305, 503–505. https://doi.org/10.1126/science.1099192

Telford, W. M., Geldart L. P., Sheriff R. E. (1990). Applied Geophysics, Cambridge University Press, Cambridge, 2nd edition, 770p

The Comet Program (2019), Understanding the Hydrologic Environment. https://www.meted.ucar.edu/training_course.php?id=16, acessed in May, 2019.

Thomas, I. D., King, M. A., Clarke, P. J. (2007). A comparison of GPS, VLBI and modelo estimates of ocean tide loading displacements. J. Geod., 81, 359–368

Tomasella, J., Hodnett, M. G., Cuartas, L. A., Nobre, A. D., Waterloo, M. J., Oliveira, S. M. (2008). The water balance of an Amazonian micro-catchment: the effect of interannual variability of rainfall on hydrological behaviour. Hydrological Processes, 22: 2133-2147. doi:10.1002/hyp.6813

Tourian, M. J., Reager, J. T., & Sneeuw, N. (2018). The total drainable water storage of the Amazon river basin: A first estimate using GRACE. Water Resources Research, 54, 3290–3312. https://doi.org/10.1029/2017WR021674

Urschl, C., Dach, U., Hugentobler, U., Schaer, S., Beutler, G. (2005). Validating ocean tide loading models using GPS. Journal of Geodesy, 78, 616-625. https://doi.org/10.1007/s00190-004-0427-9

Van Camp, M., Vauterin, P. (2005). Tsoft: Graphical and interactive software for the analysis of time series and Earth tides. Computers and Geoscience, 31:631–640. doi:10.1016/j.cageo.2004.11.015

Van Camp, M., Vanclooster, M., Crommen, O., Petermans, T., Verbeeck, K., Meurers, B., Van Dam, T., Dassargues, A. (2006). Hydrogeological investigations at the Membach station, Belgium, and application to correct long periodic gravity variations. Journal

of Geophysical Research, 111:B10403. doi:10.1029/2006JB004405.

Van Camp, M., de Viron, O., Watlet, A., Meurers, B., Francis, O., Caudron, C. (2017). Geophysics from terrestrial time-variable gravity measurements. Reviews of Geophysics, 55:938–992. doi:10.1002/2017RG000566

Van Dam, T.M., Wahr, J.M. (1987). Displacements of the Earth's Surface Due to Atmospheric Loading: Effects on Gravity and Baseline Measurements. J. Geophys. Res., 92, 1281–1286.

Van Dam, T.M., Blewitt, G., Heflin, M. (1994). Atmospheric pressure loading effects on Global Positioning System coordinate determinations. J. Geophys. Res., 99, 23939–23950.

Van Dam, T.M., Wahr, J., Chao, Y., Leuliette, E. (1997). Predictions of crustal deformation and of geoid and sea-level variability caused by oceanic and atmospheric loading. Geophys. J. Int., 129, 507–517. https://doi.org/10.1111/j.1365-246X.1997.tb04490.x

Van Dam, T., Wahr, J., Milly, P. C. D., Shmakin, A. B., Blewitt, G., Lavallée, D., & Larson, K. M. (2001). Crustal displacements due to continental water loading. Geophysical Research Letters, 28, 651–654. https://doi.org/10.1029/2000GL012120

Van Dam, T., Wahr, J., Lavallée, D. (2007). A comparison of annual vertical crustal displacements from GPS and Gravity Recovery and Climate Experiment (GRACE) over Europe. Journal of Geophysical Research: Solid Earth, 112, 1–11. doi:10.1029/2006JB004335

Velicogna, I., Wahr, J., Van den Dool, H. (2001). Can surface pressure be used to remove atmospheric contributions from GRACE data with sufficient accuracy to recover hydrological signals?. J. Geophys. Res., 106, 16415–16434. https://doi.org/10.1029/2001JB000228

Volgyesi, L., Toth, G. (2005). Modelling gravity gradient variation due to water mass fluctuations, IAG International Symposium. Gravity, Geoid and Space Missions, 1-6. doi:10.1007/3-540-26932-0_63.

Wahr, J. (1995). Earth Tides. In Global Earth Physics, 40–46. doi:10.1029/RF001p0040

Wahr, J., Molenaar, M., & Bryan, F. (1998). Time variability of the Earth's gravity field: Hydrological and oceanic effects and their possible detection using GRACE. Journal of Geophysical Research: Solid Earth, 103, 30205–30229. https://doi.org/10.1029/98JB02844

Wang, H. (2000). Surface vertical displacements and level plane changes in the front reservoir area caused by filling the Three Gorges Reservoir. Journal of Geophysical Research, 105(B6), 13211–13220. https://doi.org/10.1029/2000JB900072

Wang, H., Xiang, L., Wu, P., Steffen, H., Jia, L., Jiang, L., Shen, Q. (2013). Effects of the tibetan plateau crustal structure on the inversion of water trend rates using simulated GRACE/GPS data. Terr. Atmos. Ocean. Sci., 24, 505–512. https://doi.org/10.3319/TAO.2012.09.21.01

Wu, X., Heflin, M. B., Ivins, E. R., Argus, D. F., & Webb, F. H. (2003). Large-scale global surface mass variations inferred from GPS measurements of load-induced deformation. Geophysical Research Letters, 30, 1–4. https://doi.org/10.1029/2003GL017546

Wunsch, C. and Stammer, D. (1997). Atmospheric loading and the oceanic "inverted barometer" effect. Rev. Geophys., 35, 79–107. https://doi.org/10.1029/96RG03037

Zalán, P. V., & Matsuda, N. S. (2007). Bacia de Marajó. Boletim de Geociencias da Petrobras, 15, 311–319.

Zhang, L., Dobslaw, H., Stacke, T., Guntner, A., Dill, R., & Thomas, M. (2017). Validation of terrestrial water storage variations as simulated by different global numerical models with GRACE satellite observations. Hydrology and Earth System Sciences, 21(2), 821837. https://doi.org/10.5194/hess-21-821-2017

Zhou, J C. (2008). Loading problem in earth's tides and satellite gravity field recovery and its applications, Ph. D. thesis, Wuhan : Institute of Geodesy and Geophysics, Chinese Academy of Science, 39-43.

Zou, R., Wang, Q., Freymueller, J. T., Poutanen, M., Cao, X., Zhang, C., Yang, S., He, P. (2015). Seasonal Hydrological Loading in Southern Tibet Detected by Joint Analysis of GPS and GRACE. Sensors, 12, 30525–38. doi: 10.3390/s151229815.